UiT The Arctic University of Norway

Faculty of Science and Technology , IFT Department of Physics and Technology

MIR-based in-situ measurement of Silicon crystal-melt interface

Mathias N. Jensen

Master’s thesis in Applied Physics and Mathematics (FYS-3941), June 2020

Abstract

The absorption of IR/MIR was estimated to be $1.56 \cdot 10^4 cm^{-1}$ for $\lambda = 1.10\mu m$, $13.7cm^{-1}$ for $\lambda = 2.55\mu m$, and $9.82cm^{-1}$ for the optimum wavelength of $\lambda = 2.16\mu m$ at 1687K for extrinsic Silicon with a dopant(Boron) concentration of $2.8 \cdot 10^{16} cm^{-3}$. Three samples of interface deflections $19.66 \pm 0.02mm$, $10.96 \pm 0.02mm$, and $13.76 \pm 0.02mm$ were measured using a transmittance scan and a ray tracing of a laser beam($\lambda = 2.55\mu m$) reflected off of the interface. The obtained measurements for the transmittance scan were $20.5 \pm 0.5mm$, $10.5 \pm 0.5mm$, and $13.5 \pm 0.5mm$ for the three samples. The reflection ray tracing yielded results for two of the samples, estimated as $19.35 \pm 0.79mm$ and 11.02 ± 1.21 for corresponding true deflections $19.66 \pm 0.02mm$ and $10.96 \pm 0.02mm$.

Table of contents

List of Figures

List of Tables

1 Introduction

Over the past 70 years, semiconductor based electronics have become a significant part of our daily lives. The most common material used for these devices is Silicon, the most abundant element in the earth's crust at 28% by mass.

What separates semiconductors from the groups of conductors and insulators is the fact that they can behave as if belonging to either group without changing its composition. These materials can do this because the low energy states of the valence electrons are separated from the high energy states required for conduction are separated by a *band gap*. This band gap means that every electron must be provided with an energy exceeding the band gap energy for it to contribute to conduction. Conductors, such as Copper, do not generally have a band gap. Instead they have an overlap between the valence and conduction energy levels, requiring a minimal potential for electrons to contribute to conduction. Oppositely, insulators have a large band gap which requires a high potential for the electrons to cross, leading to very poor conduction.

The purpose of this project is to investigate the viability of using a MIR-based sensor system to measure the peak deflection of the interface, shown in Fig.1 as h_0, during production. The deflection of the interface during the production of monocrystalline Silicon(mono-Si) is a function of the progression of the annealing of the material. The motivation for developing such a system is then that the annealing process, and thereby the final crystal quality, can be indirectly monitored by measuring the deflection of the crystal-melt interface.

The temperature surrounding the interface is, by definition, the melting temperature of Silicon, which is 1687K. Because of this and the requirement of material purity, any method aimed at measuring the interface must be non-contact, limiting the measurement mechanisms to either acoustic or optical.

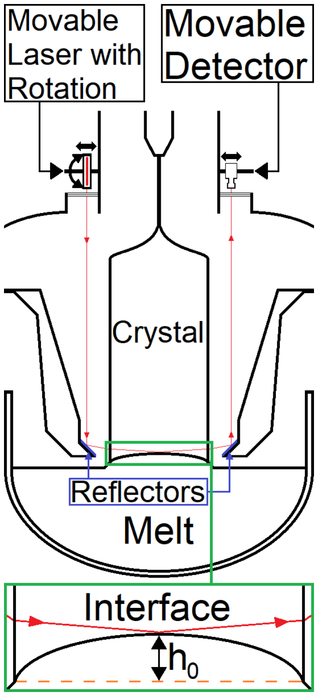

Figure 1: Sketch of proposed measurement system

The thin atmosphere(as will be discussed in Sec.3) inside the furnace and its complex geometry provides significant challenges for developing an acoustic method.
The project therefore focuses on two optical methods of measuring the interface deflection. Both of these methods rely on a MIR-laser as Silicon is largely transparent for these, as will be discussed in Sec.2.

The first of these methods is a transmittance scan, where the reflectors shown in Fig.1 are set at a 45° so that the beam has a normal angle of incidence to the crystal walls. A detector on the other side then attempts to capture the transmitted beam, the interface peak is then determined by lowering the beam entry point until the interface peak blocks the beam and the detector loses the beam.

The other method is a reflectance scan, as shown in Fig.1, where the beam incident angle is oblique. The method then scans the interface by varying the beam entry point until the beam reflects off of the interface and can be captured by the detector. The height of the interface can then be determined by tracing the ray from the known laser and detector positions.

While it may be possible to adapt this method to a number of semiconductor crystals produced through the Czochralski method such as Ge, GaAs, or InP, this project will exclusively focus on application for Silicon.
As such, the first aspect of the project will focus on describing the optical properties of Silicon and deriving a general model for its absorption spectrum in Sec.2.

The following two parts will focus on the conditions surrounding the crystal during the Czochralski production process, which will be described in detail in Sec.3. From there, the temperature distribution and resulting effects of the process will be obtained through a series of simulations in Sec.4.

In the last portion of the project, proposed measuring methods will be presented in detail and tested under lab conditions.

2 Optical properties of Silicon

As mentioned in Sec.1, what makes semiconductors stand out is the fact that semiconductors have a relatively small band gap of less than $3eV$.
This means that the lowest energy transition from the valence energy states to the conduction states is equal to the band gap energy. In the context of optics, this means that only photons of energies greater than the band gap can cause electrons to transition to the conduction states. This then means that photons of energies below the band gap cannot interact with the majority of electrons in the crystal, and thus is weakly absorbed.
If the wavelength of the laser is then chosen such that the associated photon energy is below the band gap then the beam can achieve high transmission through the Silicon crystal. The purpose of this section is then to determine the optimal wavelength for this and what the absorption is then expected to be, both for room temperature applications and in the conditions of the production process.

2.1 Electron bands and band gap energies

While it is common knowledge that electrons exist and that they are responsible for carrying electric charges to form a current, electrons also form a crucial bridge between matter and light. This is due to the photon-electron interaction, where an electron can absorb the energy of a photon to reach a higher energy state and correspondingly emit a photon by dropping to a lower energy state. However, the energy states and their energy levels relative to each other are not arbitrary, but are in fact determined by the atoms to which they belong.

The Pauli exclusion principle of quantum mechanics demand that all the electrons of an atom must each occupy a unique quantum state, this state is commonly described by the four quantum numbers:

1. The principal quantum number: $n = 1, 2, 3...$
2. The azimuthal quantum number: $\ell = 0, 1, 2, ...n - 1$
3. The magnetic quantum number: $m_\ell = 0, \pm 1, \pm 2... \pm \ell$
4. The spin quantum number: $m_s = \pm 1/2$

The principal quantum number here describes the "shell" that the electron is in, the azimuthal gives the "subshell", and the magnetic and spin defines the wavefunction of the electron. Because of this, electrons can only occupy discrete states, meaning that they cannot exist between the states defined by the quantum numbers. These discrete states then have corresponding energy levels, as depicted in Fig.2.
For any electron to transition between states, the absorbed/emitted energy must

be equal to the difference between energy levels. This brings in the Planck-Einstein relation $E = h\nu$, which states that the frequency (ν) is proportional to the energy(E) of a photon by the Planck constant ($h \approx 6.626 \cdot 10^{-34} m^2 kg/s$). This, in term means that for a photon to be absorbed, it must have an energy equal to the difference between an occupied state and an unoccupied state.

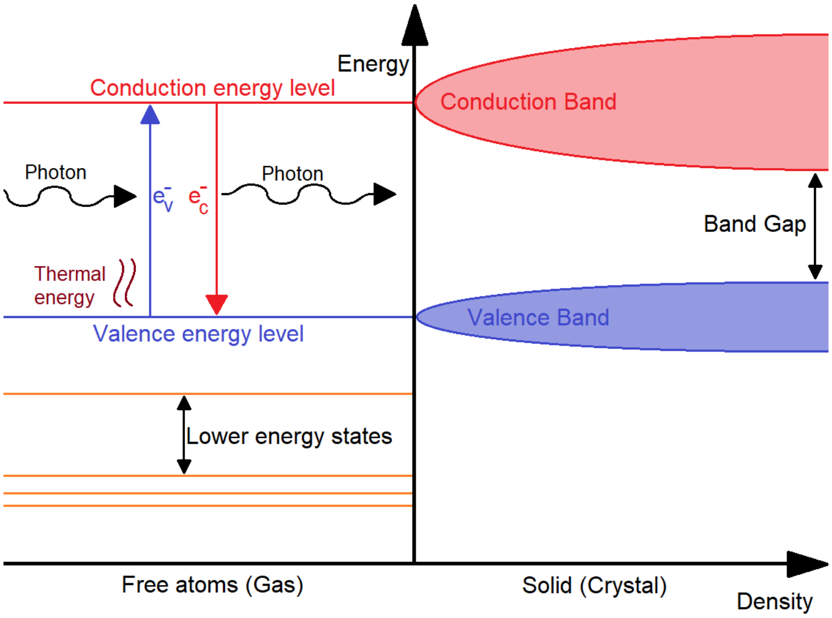

Figure 2: Conceptual sketch of electron energy levels and bands

However, as shown in Fig.2, the concept of discrete levels only applies when atoms don't interact, such as in gases. In solids, where they do interact, these discrete energy levels become diffuse and stretched into energy bands. This occurs because as the atoms become closer to each other and begin to form covalent bonds, where electrons are shared between atoms. As the electrons involved become a part of a larger quantum system, the Pauli exclusion principle then demands that they must occupy unique quantum states. This creates new allowed energy states near the energy levels of the free atoms. As the material becomes denser and more atoms are included into a single quantum system, more and more of these new states appear until the range of energies surrounding the preceding energy levels becomes so densely populated that it can be considered a continuous band.

This means that in ordered solids, such as crystals, we get continuous bands of possible electron states in the bulk material, separated by a gap of impossible electron states. The forbidden energy levels corresponding to these impossible states then define the band gap. This means that it is possible for an electron to go from any (occupied) state in the valence band, either through the absorption of a photon or by thermal excitation, to any (available) state in the conduction band and back again. This means that the solid material can both absorb and emit a large bandwidth of light, but only as long as the photon energy is equal to or greater than the band gap energy, as transitions of energies lower than the band gap would require the electrons to assume a forbidden energy level.

2.2 Electron distribution and Fermi level

Since the electron-photon interaction is the foundation of optical absorption and emission, the distribution of the electrons within the valence- and conduction-bands must be known to make a quantitative assessment of the absorption and emission spectra. This distribution is governed by the Fermi-Dirac distribution:

$$f\left(E\right) = \frac{1}{1 + e^{\frac{E - E_F}{k_B T}}}, \tag{1}$$

where k_B is Boltzmann's constant, T is temperature (in Kelvin), and E_F is the Fermi level, which describes the energy required to add an electron to the atom. This function yields the probability that an energy state E is occupied and therefore, by the law of large numbers, equals the relative density of electrons in that energy state, $f(E) = \frac{n(E)}{n}$.

This function is important for the optical behaviour of the material since the absorption of a photon of energy $E_p = h\nu_p$ can occur if and only if there exists an allowed and occupied energy state E_1 as well as an allowed and vacant energy state $E_2 = E_1 + E_p$. The probability of these conditions being true can then be defined through the Fermi-Dirac distribution, giving a joint probability:

$$f\left(E_1\right) \cdot f\left(E_p\right) = f\left(E_1\right) \cdot f\left(E_1 + E_p\right) \tag{2}$$

To be able to evaluate this expression, we must also know the energy at the Fermi level. This can be done by considering that if $E = E_F$ then the distribution evaluates to 1/2, meaning that the Fermi level is at the midpoint between the energy states. For intrinsic semiconductors, the only source of electrons and holes(vacancies) is the bulk material. Therefore, the number of electrons in the conduction band must always be equal to the number of holes in the valence band. Logically, this means that when in thermal equilibrium, the Fermi level lies in the middle of the band gap.

The expressions for the number of electrons in the conduction band(n) and holes in the valence band(n) are given in Eqs. 16.1-12 and -13 on page 643 of [4]. The

Fermi level and intrinsic carrier concentration(n_i) can then be defined as:

$$\begin{aligned} n &= N_C e^{\frac{E_F - E_C}{kT}} \\ p &= N_V e^{\frac{E_V - E_F}{kT}} \end{aligned} \quad \overset{n=p=n_i}{\Rightarrow} \quad \begin{aligned} n_i &= \sqrt{N_C N_V} e^{\frac{E_V - E_C}{2kT}} \\ E_F &= \frac{E_C + E_V}{2} + \frac{1}{2} kT \log\left(\frac{N_V}{N_C}\right) \end{aligned} \tag{3}$$

Where N_C and N_V are the effective densities of states while E_C and E_V denote the energies of the lowermost and topmost edges of the conduction and valence bands, respectively. The effective densities of states can also be described using the effective masses of the holes (m_p^*) and electrons (m_e^*) given on page 643 of [4]:

$$\begin{aligned} N_V &= 2\left(\frac{2\pi m_p{}^* kT}{h^2}\right)^{\frac{3}{2}} \\ N_C &= 2\left(\frac{2\pi m_e{}^* kT}{h^2}\right)^{\frac{3}{2}} \end{aligned} \quad \Rightarrow E_F = \frac{E_C + E_V}{2} + \frac{3}{4} kT \log\left(\frac{m_p{}^*}{m_e{}^*}\right) \tag{4}$$

However, almost all produced mono-Si also contain a controlled a highly controlled concentration of a selected contaminant, called a dopant. This dopant is commonly selected from one of a groups of the periodic table adjacent to that of the intrinsic material. For Silicon (group 14), these are commonly either

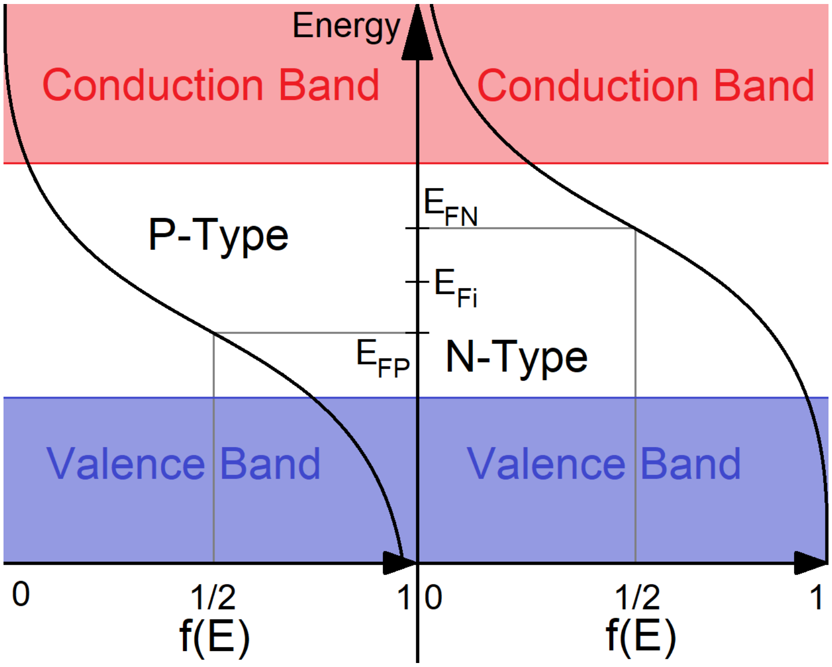

Figure 3: Conceptual sketch of Fermi-Dirac distributions in P-type (left) and N-type (right) extrinsic semiconductor material

Boron (group 13) or Phosphorus (group 15). When a dopant is introduced to the crystal, they can either serve as an electron donor (Phosphorus) or an electron acceptor (Boron). When doped, the now extrinsic semiconductor is then referred to as either N-type(P) or P-type(B), respectively.

Because the dopant atoms have a different number of electrons in their valence shell, they create new allowed electron states and add possible energy levels near the edge of either the conduction(N-type) or valence(P-Type) bands. This also means that the equality between vacant valence states and occupied conduction states is no longer valid. For N-type material, the donor atoms of the dopant will add unbound electrons to the crystal and add to the number of electrons in the conduction band:

$$n = N_D = N_C e^{\frac{E_{FN}-E_C}{kT}}, \tag{5}$$

where N_D is the concentration of donor atoms in atoms pr. cubic cm and E_{FN} is the Fermi level for the extrinsic N-type material.
This can then be solved by considering the intrinsic carrier concentration described in Eq.4 and the known intrinsic Fermi level E_{FI}:

$$\begin{aligned} n &= N_D = N_C e^{\frac{E_{FN}-E_C}{kT}} \\ n_i &= N_C e^{\frac{E_{FI}-E_C}{kT}} \end{aligned} \quad \Rightarrow E_{FN} = E_{FI} + kT \ln\left(\frac{N_D}{n_i}\right) \tag{6}$$

Which, as seen in the right side of Fig.3, means that the Fermi level increases towards the conduction band as the donor atom concentration increases.
For P-type material, the acceptor atoms have one or more electrons fewer than the bulk material and therefore contributes to the effective number of vacancies(p):

$$p = N_A = N_V e^{\frac{E_V-E_{FP}}{kT}} \tag{7}$$

Where E_{FP} is the Fermi level of the extrinsic P-type material. This can then be solved in the same way as for the N-type material:

$$\begin{aligned} p &= N_A = N_V e^{\frac{E_V-E_{FP}}{kT}} \\ n_i &= N_V e^{\frac{E_V-E_{FI}}{kT}} \end{aligned} \quad \Rightarrow E_{FP} = E_{FI} - kT \ln\left(\frac{N_A}{n_i}\right) \tag{8}$$

This causes the Fermi level to decrease towards the valence band as the concentration of acceptor atoms increases, as shown on the left side of Fig.3.

2.3 Direct and indirect band gaps

While the explanation given in Sec. 2.1 illustrates the concept of energy bands and the band gap, it is also a highly simplified version of the true case as will be shown in this section.

Because the energy band structure of a substance is dependent on the sharing of electrons through covalent bonds, it stands to reason that the nature of both bands and gap is correlated with the nature of the structure of the covalent bonds.

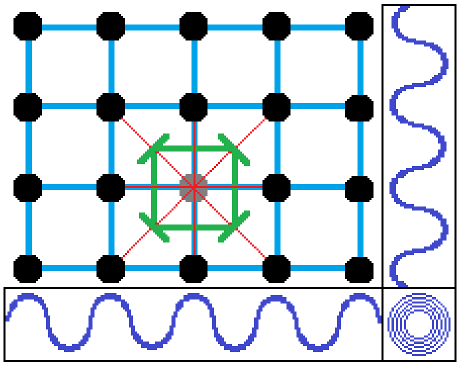

Figure 4: Conceptual illustration of periodic potential and first Brillouin zone of a square 2D lattice

As illustrated in Fig. 4, a 2D lattice can be percieved as having a periodic potential of same period as the spacing between the atoms and we can therefore describe the band structure throughout the lattice by describing the effect of the proximities outlined in red on the center atom within the green area. This green area then forms a primitive cell called a *Brillouin zone* that describes the band structure throughout the crystal.

Within the Brillouin zone, an electron state can be described as a *Bloch wave*:

$$\psi\left(\mathbf{r}\right) = e^{i\mathbf{k}\cdot\mathbf{r}} u\left(\mathbf{r}\right), \tag{9}$$

which is a solution to the *time-independent Schrödinger equation*:

$$-\frac{h^2}{2m}\nabla^2\psi^2\left(\mathbf{r}\right) + V\left(\mathbf{r}\right)\psi\left(\mathbf{r}\right) = \mathbf{E}\psi\left(\mathbf{r}\right) \tag{10}$$

Here, $V\left(\mathbf{r}\right)$ is the periodic potential of the lattice which imposes the requirement that the function $u\left(\mathbf{r}\right)$ must also be periodic with the same period. The key here is the wave vector $\mathbf{k}$ of the Bloch wave, which must be of equal dimensionality to the spatial vector $\mathbf{r}$. This means that for a specific $\mathbf{k}$-vector there are specific Bloch states describing allowed electron states and associated energy levels, this means that the band structure is dependent on the wave vector $\mathbf{k}$.

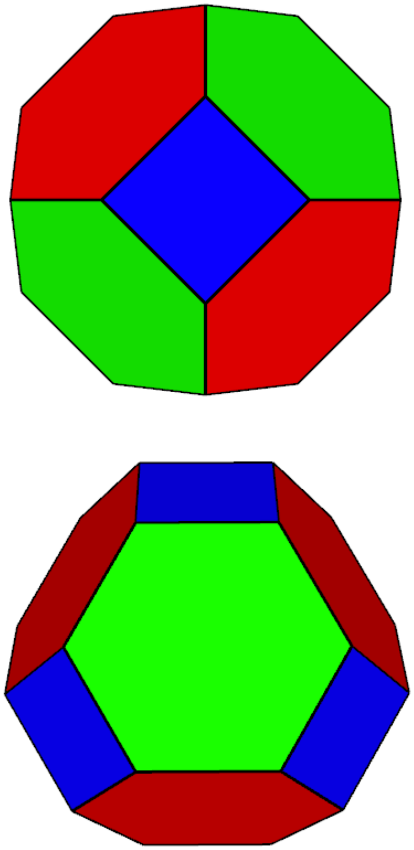

Figure 5: Projections of the Brillouin zone of Silicon from the center face (top) and hexagonal side (bottom)

In Fig. 5 we see projections of the first Brillouin zone of Silicon, which takes the shape of a truncated octahedron in the reciprocal 3D lattice such that each side directly faces the neighbouring points of the lattice.

As we can see, the **k**-vector must now be of three dimensions and can be described as:

$$\mathbf{k} = \begin{bmatrix} \mathbf{b}_1 & \mathbf{b}_2 & \mathbf{b}_3 \end{bmatrix} \cdot \mathbf{p}, \qquad (11)$$

The **b**-vectors are the normal vectors to the three red hexagonal surfaces of the Brillouin zone shown in Fig. 5 that span the space of the zone. The vector $\mathbf{p} = \begin{bmatrix} u & v & w \end{bmatrix}^T$ is then used to describe some point along the surface of the zone, commonly using the reference points:

Point	$\mathbf{p}$		
Γ	0	0	0
X	0	1/2	1/2
L	1/2	1/2	1/2
W	1/4	3/4	1/2
U	1/4	5/8	5/8
K	3/8	3/4	3/8

Though, for simplicity we will mostly focus on the points Γ,X and L which describe the center of the zone, square face and hexagonal face, respectively.

The difference between a direct band gap semiconductor, such as GaAs, and an indirect band gap semiconductor, such as Silicon, is the **k**-vector difference between the valence band peak and the bottom of the conduction band.

As we can see in Fig. 6 for GaAs, the valence band peak and conduction band bottom are aligned at the same **k**-vector, this means that an electron transition across the band gap is purely a matter of energy since no change in the wave vector is required.

For indirect band gaps, such as Silicon whose E-k diagram is depicted in Fig. 7, we can see that this is not the case as the minimum of the conduction band is at a different **k** vector than the valence band maximum. This means that for an electron to transition between these energies, it must change both its energy and its wave vector.

This change in wave vector can be viewed as analogous to physical movement where, in classical mechanics, a force must act on the object to change its velocity, exchanging a momentum between the active elements. Although, electrons generally adhere to quantum mechanics instead of classic mechanics, so the change in wave vector is not actually a change in velocity and this change is not, strictly speaking, an exchange of actual momentum because the net velocity of the lattice does not change. Instead, this is commonly referred to as the *crystal momentum*:

$$\mathbf{p}_{\text{crystal}} = \hbar\mathbf{k} \qquad (12)$$

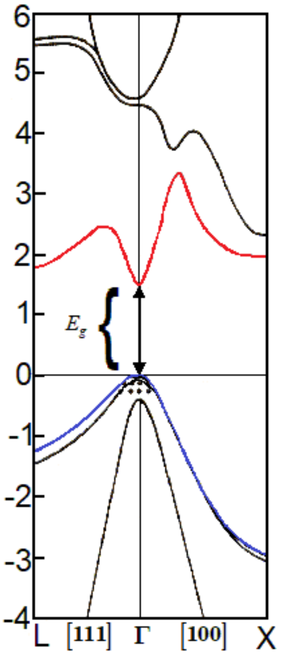

Figure 6: E-k diagram of GaAs[26]

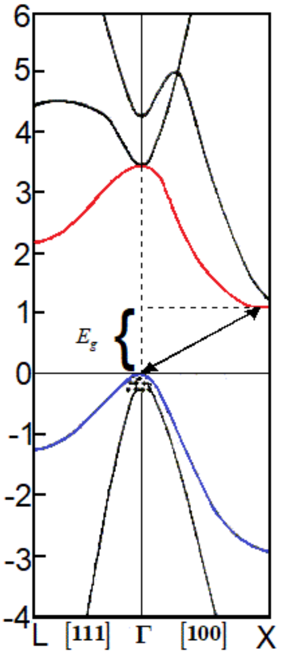

Figure 7: E-k diagram of Silicon [26]

This "momentum" manifests itself as an oscillation in the lattice, acting like a wave propagating through the crystal which does not produce a net movement in either the atoms or the lattice as a whole, hence the differentiation between momentum and crystal momentum.

Since this momentum is a pseudomomentum, consisting of waves in the lattice, it is not actually an independent event and is not carried by an actual particle in the way that photons carry light. However, to understand and quantify the effect of this wave in a quantum system, these waves are said to be carried by a quasiparticle referred to as a phonon. As quasiparticles, phonons don't actually exist, but are instead defined as a collective elastic excitation of the atoms of the lattice.

In the context of optics, this means that for indirect band gap materials, absorption requires either a photon of sufficient energy to bridge the direct band gap, which is usually significantly larger than the true band gap, or this requires both a photon and a phonon. This means that single photon absorption is relatively harder in indirect band gap material than for direct band gaps when the photon energy is near the band gap energy.

The biggest difference between these two is in photon emission. In direct band gap materials, the only thing needed is an energy release, which the electrons can do on their own. In indirect materials, however, a phonon is also required. This means that emission occurs spontaneously in direct materials, while emission from indirect materials must be stimulated by a phonon-electron interaction, resulting in direct band gap materials producing significantly higher emissions than indirect band gap materials. This is the principal reason why devices such as Light Emitting Diodes (LED's) and Laser Diodes (LD's) are almost exclusively made from composite semiconductor materials based on direct band gap materials, such as GaAs, ZnSe or InGaN.

2.4 Absorption in Silicon

For intrinsic Silicon, as discussed in Sec.2.3, a single-photon band-to-band transition requires a change in crystal momentum provided by a phonon. This makes the photon absorption a joint event of both a photon and a phonon interacting with an electron simultaneously.
This means that the absorption is both innately weaker and a more complicated process for indirect transitions than for direct ones.

2.4.1 Intrinsic Silicon

The mathematical expression for the absorption spectrum of indirect semiconductors has been the subject of many works, such as that of Berglund[19]. Berglund postulated in Eq. 1 of [19] that the absorption coefficient could be expressed as:

$$\alpha_\nu = \begin{cases} A(h\nu - E_g + E_P)^2 N_p & , h\nu > E_g - E_p \\ 0 & h\nu \leq E_g - E_p \end{cases} \tag{13}$$

Here, the parameters are:

- A: Temperature-independent constant
- h: Planck's constant
- ν: Photon frequency in Hz
- E_g: Indirect band gap energy
- E_p: Energy of involved phonon
- $N_P = \left(e^{E_p/kT} - 1\right)^{-1}$: Fermi distribution of involved phonon

This project will instead consider the expression found by Chow[27] shown in Eq.(16). The reason for this is that Chow performed a more thorough derivation of the equations, making the expression more theoretically valid. Chow argued that the absorption event can be viewed as taking one of two paths, as shown in Fig.8. These paths are then defined as:

- Path A: A photon of energy $h\nu \geq E_g \mp \Omega\left(\mathbf{p}_0\right)$ is absorbed and an electron makes a transition from the valence band into a virtual state where it either absorbs or emits a phonon of energy $\Omega\left(\mathbf{p}_0\right)$ and momentum $\mathbf{p}_0$ to complete the transition:
$\{\mathbf{k} \sim \mathbf{0}, \epsilon_v\left(\mathbf{k} \sim \mathbf{0}\right)\} \rightarrow \{\mathbf{k} \sim \mathbf{0}, \epsilon_c\left(\mathbf{p} \sim \mathbf{p}_0\right) \mp \Omega\left(\mathbf{p}_0\right)\} \rightarrow \{\mathbf{p} \sim \mathbf{p}_0, \epsilon_c\left(\mathbf{p} \sim \mathbf{p}_0\right)\}$
- Path B: A phonon of momentum $\mathbf{p}_0$ and energy $\Omega\left(\mathbf{p}_0\right)$ is either absorbed or emitted so that an electron moves to a virtual state where a photon of energy $h\nu \geq E_g \mp \Omega\left(\mathbf{p}_0\right)$ is absorbed, completing the transition:
$\{\mathbf{k} \sim \mathbf{0}, \epsilon_v\left(\mathbf{k} \sim \mathbf{0}\right)\} \rightarrow \{\mathbf{p} \sim \mathbf{p}_0, \epsilon_v\left(\mathbf{k} \sim \mathbf{0}\right) \pm \Omega\left(\mathbf{p}_0\right)\} \rightarrow \{\mathbf{p} \sim \mathbf{p}_0, \epsilon_c\left(\mathbf{p} \sim \mathbf{p}_0\right)\}$

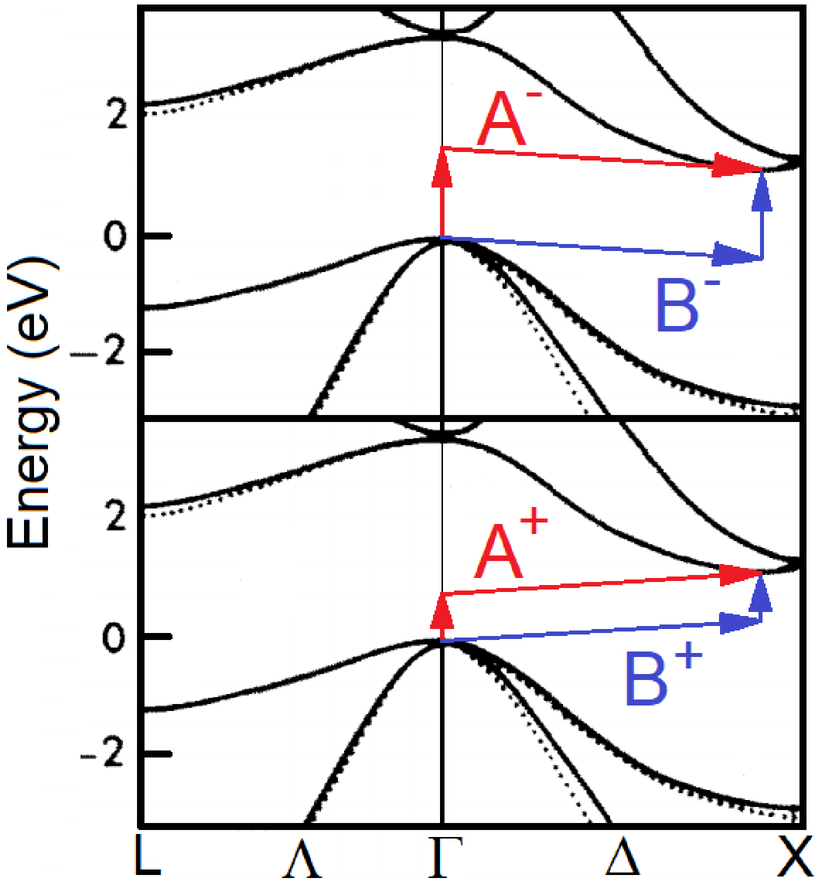

Figure 8: Paths A and B when emitting (top) or absorbing(bottom) a phonon, overlaid over the band structure(Cropped and up-scaled from Fig. 1 of [21])

Chow then rewrote the polarization function for optical phonon interactions as formulated by Dunn[28] using Green's functions, thereby obtaining the absorption coefficients for Path A and B (Eqs. 25 and 29 of [27]):

$$\begin{aligned} \alpha_A(\omega_0) &= \frac{e^2\delta {g_c}^2}{48\pi m^2}\frac{\omega_0}{(\Delta E_1)^2}\frac{|\langle \mathbf{0},c|\mathbf{p}|\mathbf{0},v\rangle|^2}{(\omega_0-\Delta E_1)^2}(4m_v m_c)^{3/2} \\ &\times\left[(\omega_0+\Omega(\mathbf{p}_0)-E_g)^2 n(\mathbf{p}_0)+(\omega_0-\Omega(\mathbf{p}_0)-E_g)^2(n(\mathbf{p}_0)+1)\right] \end{aligned} \tag{14}$$

$$\begin{aligned} \alpha_B(\omega_0) &= \frac{e^2\delta {g_v}^2}{48\pi m^2}\frac{\omega_0}{(\Delta E_2)^2}\frac{|\langle \mathbf{p}_0,c|\mathbf{p}|\mathbf{p}_0,v\rangle|^2}{(\omega_0-\Delta E_2)^2}(4m_v m_c)^{3/2} \\ &\times\left[(\omega_0+\Omega(\mathbf{p}_0)-E_g)^2 n(\mathbf{p}_0)+(\omega_0-\Omega(\mathbf{p}_0)-E_g)^2(n(\mathbf{p}_0)+1)\right] \end{aligned} \tag{15}$$

This then gives the total absorption constant $\alpha = \alpha_A + \alpha_B$:

$$\begin{aligned}\alpha\left(\nu\right) = Dh\nu &\left(\frac{\delta {g_c}^2 \| \langle \mathbf{0}, c \left| \mathbf{p} \right| \mathbf{0}, v \rangle \|^2}{E_{g,D}(\mathbf{0})^2 [h\nu - E_{g,D}\left(\mathbf{0}\right)]^2} + \frac{\delta {g_v}^2 \| \langle \mathbf{p}_0, c \left| \mathbf{p} \right| \mathbf{p}_0, v \rangle \|^2}{E_{g,D}(\mathbf{p}_0)^2 [h\nu - E_{g,D}\left(\mathbf{p}_0\right)]^2}\right), \\ &\times \left[\left(h\nu + \Omega\left(\mathbf{p}_0\right) - E_g\right)^2 n\left(\mathbf{p}_0\right) + \left(h\nu - \Omega\left(\mathbf{p}_0\right) - E_g\right)^2 \left(n\left(\mathbf{p}_0\right) + 1\right)\right]\end{aligned} \tag{16}$$

where $D = \frac{e^2 (4 m_v m_v)^{\frac{3}{2}}}{48 \pi m^2}$ and $E_{g,D}\left(\mathbf{k}\right)$ is the direct band gap for wavevector $\mathbf{k}$.

Due to the phonon energy $\Omega\left(\mathbf{p}_0\right)$ being very low ($63 meV$[29]) compared to the band gap ($\approx 1.12 eV$ at 300K), the following approximation can be used:

$$\left(h\nu + \Omega\left(\mathbf{p}_0\right) - E_g\right)^2 \approx \left(h\nu - \Omega\left(\mathbf{p}_0\right) - E_g\right)^2 \approx \left(h\nu - E_g\right)^2 \tag{17}$$

Such that:

$$\left(h\nu + \Omega\left(\mathbf{p}_0\right) - E_g\right)^2 n\left(\mathbf{p}_0\right) + \left(h\nu - \Omega\left(\mathbf{p}_0\right) - E_g\right)^2 \left(n\left(\mathbf{p}_0\right) + 1\right) \approx \left(h\nu - E_g\right)^2 \eta\left(\mathbf{p}_0\right), \tag{18}$$

where $\eta\left(\mathbf{p}_0\right) = 2n\left(\mathbf{p}_0\right) + 1 = \frac{e^{\frac{\Omega(\mathbf{p}_0)}{kT}} + 1}{e^{\frac{\Omega(\mathbf{p}_0)}{kT}} - 1}$, allowing Eq.16 to be rewritten as:

$$\begin{aligned}\alpha_p\left(\nu\right) = &\left(\frac{\delta {g_c}^2 \| \langle \mathbf{0}, c \left| \mathbf{p} \right| \mathbf{0}, v \rangle \|^2}{E_{g,D}(\mathbf{0})^2 [h\nu - E_{g,D}\left(\mathbf{0}\right)]^2} + \frac{\delta {g_v}^2 \| \langle \mathbf{p}_0, c \left| \mathbf{p} \right| \mathbf{p}_0, v \rangle \|^2}{E_{g,D}(\mathbf{p}_0)^2 [h\nu - E_{g,D}\left(\mathbf{p}_0\right)]^2}\right) \\ &\times D \eta\left(\mathbf{p}_0\right) \left(h\nu - E_g\right)^2 h\nu\end{aligned} \tag{19}$$

As we can see, expressions in Eqs.19 and 16 can be argued to have the same principal shape as that of Eq.13 postulated by Berglund. However, Eq.19 explicitly includes the Bloch-state matrix elements $\left|\langle \mathbf{0}, c | \mathbf{p} | \mathbf{0}, v \rangle\right|^2$ and $\left|\langle \mathbf{p}_0, c | \mathbf{p} | \mathbf{p}_0, v \rangle\right|^2$ corresponding to the photon induced electron transitions from the valence band peak to a virtual state and virtual state to conduction band vally, respectively. The added inclusion of both the phonon couplings g_c and g_v for the valence and conduction band as well as the direct band gaps $E_{g,D}\left(\mathbf{p}\right)$ at both valence peak ($\mathbf{0}$) and conduction valley($\mathbf{p}_0$) and the number of conduction valleys δ makes Eq.19 a more complete expression of the absorption process than the findings of Berglund.

Region of validity

Since the expression for the absorption in Eq. 19 considers the phonon assisted absorption processes, the absorption spectrum near the intrinsic absorption edge can be separated into three regions as shown in Fig.9:

- Region B: where the photon energy is $h\nu < E_g - \Omega(\mathbf{p}_0)$, meaning that the photon energy is too low for single photon absorptions to cause band-to-band transition.
- Region A_i: where the photon energy is $E_g - \Omega(\mathbf{p}_0) < h\nu < E_{g,D}(\mathbf{0})$, meaning that the photon energy is sufficient for a band-to-band transition, but only indirect (phonon assisted) absorption.
- Region A_d: where the photon energy is $E_{g,D}(\mathbf{0}) < h\nu$, meaning that both indirect and direct single-photon band-to-band transitions are possible.

As can be seen in Eq.19, the absorption coefficient is proportional to the square of the energy difference between the photon energy and the band gap energy. Because of this, and the inverse square proportionality to the photon energy relative to the direct band gap, it is expected that the absorption coefficient becomes significantly high as the photon energy exceeds the band gap energy. Because the purpose of this project is to evaluate transmission based measurement methods, the derived model will be focused on the regions where the absorption is expected to be low. As can be seen in Fig.9, the regions where the absorption is sufficiently weak to make practical measurements are the lower bounds of region A_i through region B.

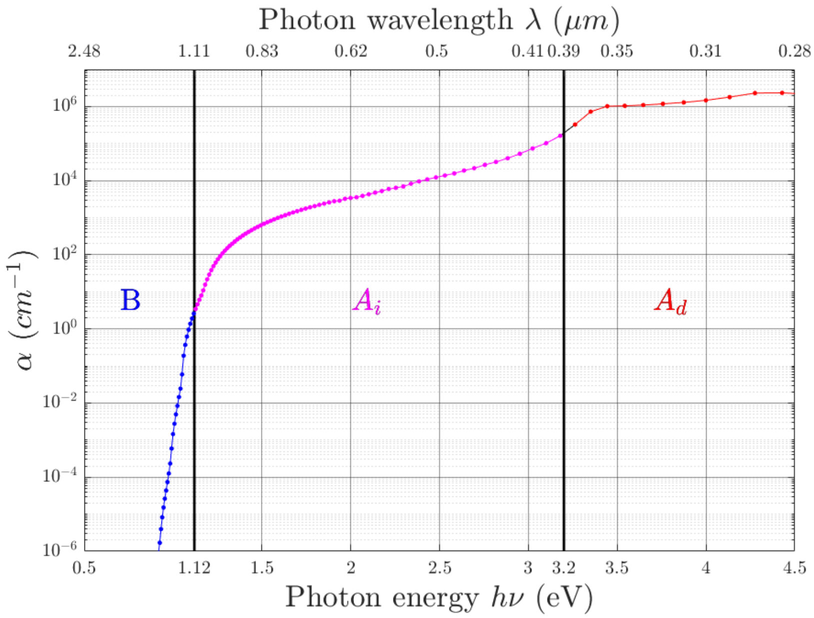

Figure 9: Absorption spectrum of Si(Schinke et al. [33]) with regions B, A_i and A_d marked for room temperature

Furthermore, in Eqs. 19 and 20 of [27] Chow made the approximations:

$$\begin{array}{l} f\left(\mu_+ + (\mathbf{p}-\mathbf{p}_0)^2/2m_c - \Omega\left(\mathbf{p}_0\right)\right) = f\left(\epsilon_c\left(\mathbf{p}\right) - \Omega\left(\mathbf{p}_0\right)\right) \approx 0 \\ f\left(\mu_- + k^2/2m_v\right) = f\left(\epsilon_v\left(\mathbf{0}\right)\right) \approx 0 \end{array}, \tag{20}$$

where $f(\cdot)$ is the Fermi-dirac distribution of the energies $\epsilon_v(\mathbf{0})$ and $\epsilon_c(\mathbf{p})$ of the valence band peak and conduction valley, respectively. These approximations only hold if the Fermi level is sufficiently far away from the conduction and valence bands:

$$\min\left[\epsilon_c\left(\mathbf{p}\right) - \Omega\left(\mathbf{p}_0\right), -\epsilon_v\left(\mathbf{0}\right)\right] - E_f >> kT \tag{21}$$

As the temperature increases, and as dopant is added, this assumption may not hold. Because of this, the approximation done by Chow in Eq. 18 of [27] may not be valid for the conditions expected in a Czochralski-furnace. Therefore, the new approximation in Eq.22 is derived to increase the range of validity.

$$\beta^{-1}\sum_{z_v}\frac{n\left(\mathbf{p}_0\right)}{z_v+\zeta_\mu+\Omega\left(\mathbf{p}_0\right)-\mu_+-\left(\mathbf{p}-\mathbf{p}_0\right)^2\Big/2m_c}\frac{1}{z_v+\mu_-+k^2/2m_v}\frac{1}{\left[z_v+\zeta_\mu-\epsilon_c\left(\mathbf{0}\right)\right]^2}$$
$$\approx\left\{\frac{1-f\left(-\epsilon_v\left(\mathbf{0}\right)\right)}{\left[\zeta_\mu-\epsilon_v\left(\mathbf{0}\right)-\epsilon_c\left(\mathbf{0}\right)\right]^2}-\frac{f\left(\epsilon_c\left(\mathbf{p}_0\right)-\Omega\left(\mathbf{p}_0\right)\right)}{\left[\epsilon_c\left(\mathbf{p}_0\right)-\epsilon_c\left(\mathbf{0}\right)\right]^2}\right\}\frac{n\left(\mathbf{p}_0\right)}{\zeta_\mu+\Omega\left(\mathbf{p}_0\right)-E_g-\frac{\left(\mathbf{p}-\mathbf{p}_0\right)^2}{2m_c}-\frac{k^2}{2m_v}} \tag{22}$$

Continuing along the same derivation as done by Chow, the new form of Eq.14 then becomes:

$$\alpha_A\left(\omega_0\right)=\frac{e^2\delta{g_c}^2|\langle\mathbf{0},c|\mathbf{p}|\mathbf{0},v\rangle|^2}{48\pi m^2}\frac{\omega_0(4m_v m_c)^{3/2}}{\left(\Delta E_1\right)^2}\left(\frac{1-f\left(-\varepsilon_v\left(\mathbf{0}\right)\right)}{\left(\omega_0-\Delta E_1\right)^2}-\frac{f\left(\varepsilon_v\left(\mathbf{p}_0\right)-\Omega\left(\mathbf{p}_0\right)\right)}{\left(\Delta E_{11}\right)^2}\right),$$
$$\times\left[\left(\omega_0+\Omega\left(\mathbf{p}_0\right)-E_g\right)^2 n\left(\mathbf{p}_0\right)+\left(\omega_0-\Omega\left(\mathbf{p}_0\right)-E_g\right)^2\left(n\left(\mathbf{p}_0\right)+1\right)\right] \tag{23}$$

where $\Delta E_{11}=\varepsilon_c\left(\mathbf{p}_0\right)-\varepsilon_c\left(\mathbf{0}\right)$, and with similar terms found in the new expression of Eq.15 for B-path processes.

2.4.2 Extrinsic Silicon

As discussed in Sec.2.2, the Fermi level is a key parameter in describing the behaviour of a semiconductor, and the dopant level is the main factor in altering it. In addition to altering the Fermi level, the dopant also has a narrowing effect[30] on the band gap as described by the equation:

$$\Delta E_g\left(N\right)=\frac{-3q^2}{16\pi\varepsilon_s}\sqrt{\frac{q^2N_D}{\varepsilon_s kT}}\left(meV\right) \tag{24}$$

However the total shrinkage of the band gap is quite small, even for such high dopant concentrations that the Fermi level is pushed inside either the valence or conduction bands. In such cases, the semiconductor becomes *degenerate*, meaning that it behaves more like a metal than a semiconductor. Evaluating the Fermi level using Eg.8 it can be found that p-type material becomes degenerate when the dopant concentration exceeds $2.4205\cdot10^{19}cm^{-3}$ at 300K or $3.2278\cdot10^{19}cm^{-3}$ at 1687K. For these concentrations, the corresponding band gap shrinkage given by Eq.24 is $-0.111eV$ and $-0.171eV$. For a more reasonable dopant concentration, such as $10^{17}cm^{-3}$, the shrinkages become $-7.14\cdot10^{-3}eV$ and $-3.01\cdot10^{-3}eV$, which is decidedly negligible.

A larger difference between intrinsic and extrinsic absorption can be found in the B-region shown in Fig.9. While in intrinsic material, the absorption becomes near zero at photon energies lower than the band gap, this is not so for extrinsic material. The presence of a dopant in the lattice creates new mobile charges, either electrons in the conduction band or holes in the valence band. While this becomes true for intrinsic material as well due to thermal excitation, the additional charges provided by the dopant greatly enhances this effect. This free charge absorption is a process of intraband absorption, meaning that it can occur with single photon energies below the band gap and can be described by the expression [31]:

$$\alpha\left(\lambda\right) = \frac{q^3 \lambda^2 p}{4\pi^2 \varepsilon_0 c^3 n {(m^*)}^2 \mu}, \tag{25}$$

where $q = 1.6022 \cdot 10^{-19} C$ is the elemental charge, $\varepsilon_0 = 8.8542 \cdot 10^{-12} \mathrm{F}/_{\mathrm{m}}$ is the vacuum permittivity, m^* is the effective charge mass, n is the refractive index, p is the charge (dopant) density and μ is the charge mobility.

Since dopants alter the band structure by creating new states near the bands of the bulk material, the presence of high dopant densities, either in bulk or inhomogeneities, can also create ”shallow” states separate from the bands of the bulk material that are subject to similar path processes as described in Sec.2.4.1.

2.4.3 Temperature dependent model

Given that the expressions found in Sec.2.4.1 rely heavily on the exact band structure being known, constructing a theoretically exact model would require a complete expression for the temperature dependence of the entire band structure. While this may be possible, it is well beyond the scope of this project and the relevant quantities will therefore be approximated using appropriate functions of the temperature.

Considering the findings of Sec.2.4.1, an approximate model for the intrinsic absorption in region A_i depicted in Fig.9 can be constructed from Eq.16 with considerations to Eq.23 and the complementary expression for B-path processes. By considering the non-energy factors as temperature dependent coefficients, the model can be expressed as:

$$\alpha_{Approx,A_i}\left(\nu,T\right)=\left\{\frac{C_A\left(T\right)}{E_{g,D}(\mathbf{0},T)^2}\left[\frac{F_{11}\left(T\right)}{\left[h\nu-E_{g,D}\left(\mathbf{0},T\right)\right]^2}-\frac{F_{12}\left(T\right)}{\Delta E_{11}(T)^2}\right]+\right.$$
$$\left.\frac{C_B\left(T\right)}{E_{g,D}(\mathbf{p}_0,T)^2}\left[\frac{F_{21}\left(T\right)}{\left[h\nu-E_{g,D}\left(\mathbf{p}_0,T\right)\right]^2}-\frac{F_{22}\left(T\right)}{{\Delta E_{22}}^2}\right]\right\}D\eta\left(\mathbf{p}_0,T\right)\left(h\nu-E_g\left(T\right)\right)^2h\nu \tag{26}$$

Including the effects of adding a dopant as discussed in Sec.2.4.2, the complete model is described as:

$$\begin{aligned}\alpha_{Ex,B+A_i}\left(\nu,T\right)=\chi\left(h\nu\right)&\left\{\frac{C_1\left(T\right)}{E_{g,D}(\mathbf{0},T)^2\left[h\nu-E_{g,D}\left(\mathbf{0},T\right)\right]^2}+\right.\\&\left.\frac{C_2\left(T\right)}{E_{g,D}(\mathbf{p}_0,T)^2\left[h\nu-E_{g,D}\left(\mathbf{p}_0,T\right)\right]^2}+M\left(\nu,T\right)\right\}\\&\times D\eta\left(\mathbf{p}_0,T\right)\left(h\nu-E_g\left(T\right)\right)^2h\nu+C_{FCA}\left(\nu,T\right)\nu^{-2}N\end{aligned}\quad, \tag{27}$$

where $\chi\left(h\nu\right)=\begin{cases}1:h\nu\geq E_g\left(T\right)\\0:h\nu<E_g\left(T\right)\end{cases}$ is a step function marking the edge of region A_i where Eq.26 is valid.

As can be seen in Eq.27, the Bloch-state elements($|\langle\mathbf{0},c|\mathbf{p}|\mathbf{0},v\rangle|^2$ and $|\langle\mathbf{p}_0,c|\mathbf{p}|\mathbf{p}_0,v\rangle|^2$), phonon couplings($g_v$ and g_c) and conduction valley counts(δ) of Eq.16 have been absorbed into the coefficient functions $C_1\left(T\right)$ and $C_2\left(T\right)$.
While the true temperature dependent expressions for these functions can be determined, this would require a derivation of the temperature dependence of the entire band structure, which is well beyond the scope of this project. Instead, the coupling coefficients are proposed to follow an exponential temperature model:

$$C_n\left(T\right)=\gamma_n e^{\delta_n T} \tag{28}$$

Similarly, the direct band gap energies $E_{g,D}\left(\cdot,T\right)$ and the indirect band gap E_g are also approximated using the semi-empirical equation proposed by Varshni[41]:

$$E\left(T\right) = E\left(0\right) + \frac{\alpha T^2}{T+\beta}, \tag{29}$$

where α and β are material parameters and $E(0)$ is the energy at 0K.
The parameters for the indirect band gap(E_g) of Silicon are shown in Table 1 as given by the works of Alex et al. [46].

$E_g\left(0\right)$	α	β
$1.1692eV$	$-4.9 \pm 0.2 \cdot 10^{-4} {}^{eV}/_{K}$	$655 \pm 40K$

Table 1: Varshni parameters for indirect band gap

The function $M\left(\nu,T\right)$ is a gathered function of the residuals caused by the Fermi level being close to the band edges as described at the end of Sec.2.4.1 and the transitions due to the shallow states described in Sec.2.4.2:

$$M\left(\nu,T\right) = \frac{C_{12}\left(T\right)}{E_{g,D}(\mathbf{0},T)^2 \Delta E_{11}(T)^2} + \frac{C_{22}\left(T\right)}{E_{g,D}(\mathbf{p}_0,T)^2 \Delta E_{22}{}^2} + \alpha_{SS,A_i}\left(\nu,T\right) \tag{30}$$

Where $\alpha_{SS,A_i}\left(\nu,T\right)$ is the absorption due to shallow states, assuming that the band of these states is **k**-dependant it is reasonable to assume that both direct and indirect transitions to and from these can occur. In this case, the absorption due to these states can be expressed as two sets of A- and B-path processes, one for transitions from the valence band and one to the conduction band.
However, due to a lack of a sufficiently large dataset describing the variation of the absorption spectrum as a function of temperature, a compromise must be made and $\alpha_{SS,A_i}\left(\nu,T\right)$ is therefore evaluated using only one path process. Furthermore, due to the fact that for the residuals we expect that $C_{12}\left(T\right) << C_1\left(T\right)$ and $C_{22}\left(T\right) << C_2\left(T\right)$ and assuming that the relationships $\Delta E_{11}{}^2\left(T\right) > \left[E_g\left(T\right) - E_{g,D}\left(\mathbf{0},T\right)\right]^2$ and $\Delta E_{22}{}^2\left(T\right) > \left[E_g\left(T\right) - E_{g,D}\left(\mathbf{p}_0,T\right)\right]^2$ as seen in Fig.7 hold, then it can be expected that the residuals are a minor component and are therefore fitted into the same expression as $\alpha_{SS,A_i}\left(\nu,T\right)$.

The complete model is then expressed as:

$$\begin{aligned} \alpha_{Ex,B+A_i}\left(\nu,T\right) = \chi\left(h\nu\right) \Bigg\{ & \frac{C_1\left(T\right)}{E_{g,D}(\mathbf{0},T)^2 \left[h\nu - E_{g,D}\left(\mathbf{0},T\right)\right]^2} + \\ & \frac{C_2\left(T\right)}{E_{g,D}(\mathbf{p}_0,T)^2 \left[h\nu - E_{g,D}\left(\mathbf{p}_0,T\right)\right]^2} + \frac{C_3\left(T\right)}{E_a{}^2\left(T\right)\left[h\nu - E_a\left(T\right)\right]^2} \Bigg\} \\ & \times D\eta\left(\mathbf{p}_0,T\right)\left(h\nu - E_g\left(T\right)\right)^2 h\nu + C_{FCA}\left(\nu,T\right)\nu^{-2}N \end{aligned} \tag{31}$$

2.4.4 Fitting of temperature model

Using data from Schinke et al.[33] and Šik et al.[32], the region A_i absorption expression is fit to the data as is seen in Fig.10. As is clear from Fig.10, there is a little available data regarding the absorption near the band gap at higher temperatures, which makes it difficult to determine a good fit for the most important section of the absorption spectrum.

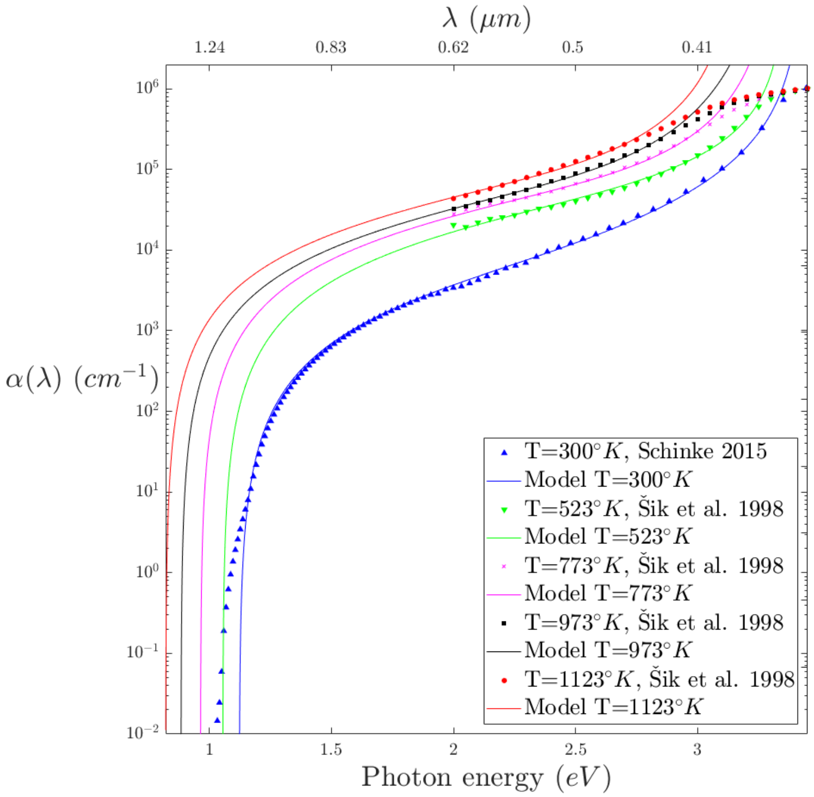

Figure 10: Logarithmic plot of independent best fits of model to the data of Schinke and Šik

From the independent fitting, the values of the coefficients $C_1\,(T)$,$C_2\,(T)$, and $C_3\,(T)$ are shown in Fig.11 and the energies $E_{g,D}\,(\mathbf{0},T)$,$E_{g,D}\,(\mathbf{p}_0,T)$, and $E_a\,(T)$ are shown in Fig.12:

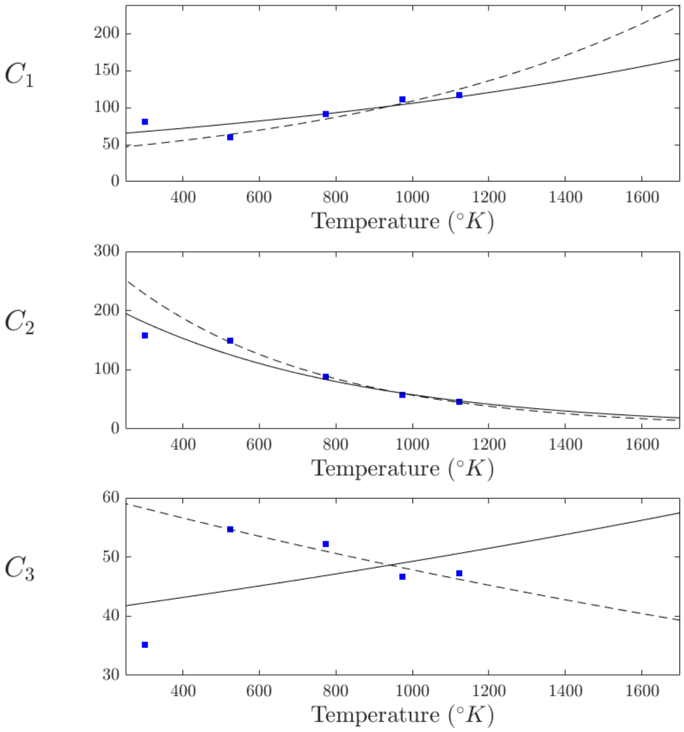

Figure 11: Coefficient parameters of best fits

The points shown in Fig.11 are the best fitted values of the C coefficients. The solid lines are then the best fits of the proposed modelling function stated in Eq.28 for all five datasets, while the dashed line is the fit for only those of Šik et al.

Since the data of Šik et al. has a wide temperature range and follows the proposed model well, the dashed line functions will be considered from here on. In

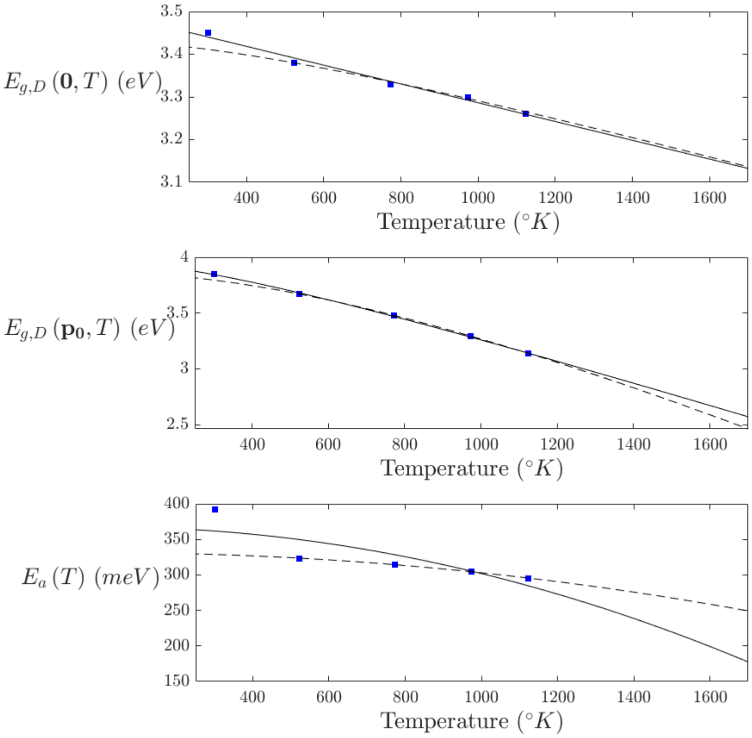

Figure 12: Energy parameters of best fits

Fig.12, we see the best fitted values of the energies shown as blue squares with the proposed Varshni equation(Eq.29) fitted onto them. Again, we see that the solid lines of the fit for all five datasets conforms poorly, while the dashed line using only the data of Šik et al. conforms well to the model.

The determined fit parameters are described in Table 2:

Energy	$E_x(0)$	α	β	Coef.	γ	δ
$E_{g,D}(\mathbf{0},T)$	3.432	$-2.6 \cdot 10^{-4}$	844.1	$C_1(T)$	35.56	$1.12 \cdot 10^{-3}$
$E_{g,D}(\mathbf{p},T)$	3.866	$-1.8 \cdot 10^{-3}$	522.2	$C_2(T)$	413.5	$-1.98 \cdot 10^{-3}$
$E_a(T)$	0.331	$-7.7 \cdot 10^{-2}$	$2.7 \cdot 10^{6}$	$C_3(T)$	63.31	$-2.76 \cdot 10^{-4}$

Table 2: Table of determined model parameters

2.4.5 Free Carrier Absorption

The free carrier term:

$$C_{FCA}(\nu,T)\,\nu^{-2}N \tag{32}$$

With:

$$C_{FCA}(\nu,T) = \frac{q^3}{4\pi^2\varepsilon_0 c n(\nu,T)\left(m^*(T)\right)^2\mu(T)} \tag{33}$$

As explored by Batista et al.[42], the charge carrier mobility is inversely proportional to $T^{2.7\pm0.1}$ and while the refractive index[43] and effective charge mass[44] are both temperature dependent, they are negligibly weak in comparison, the approximation is therefore made:

$$C_{FCA}(\nu,T) \approx \frac{q^3}{9.2 \cdot 10^9 \pi^2 \varepsilon_0 c (m^*)^2 n(\nu)\, T^{-2.7}} \tag{34}$$

The principal factor in the frequency dependence of this is then given by the Sellmeier equation determined by Chandler-Horowitz and Amirtharaj[34]:

$$n(\nu) = \sqrt{11.67316 + \frac{\nu^2}{c^2} + \frac{0.004482633c^2}{\nu^2 - (1.108205c)^2}} \tag{35}$$

The free carrier absorption coefficient can be seen in Fig.13.

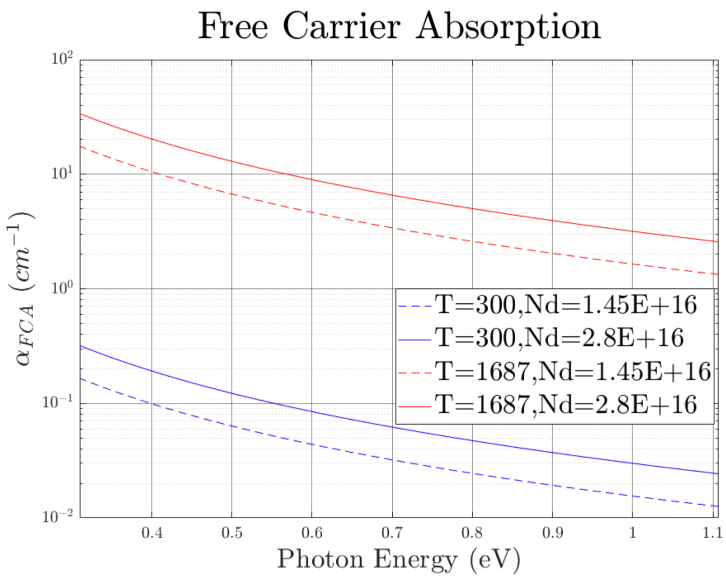

Figure 13: Free carrier absorption coefficient for border temperatures and dopant concentration

2.4.6 Multi-photon Absorption

While not previously mentioned, absorption can also occur for energies below the band gap, this can then be described using the i-photon absorption coefficients (β_i):

$$\frac{\partial I}{\partial l} = -\sum_{i=1}^{n} \beta_i {I_0}^{i} \tag{36}$$

In the most likely case of two-photon absorption, the absorbance can then be expressed as:

$$A\left(l\right) = \frac{1}{1+\beta_2 l I_0} \tag{37}$$

An expression for the two-photon absorption coefficient was derived by Dinu[40] as:

$$\beta\left(\nu\right) = C_2 {F_2}^{ind}\left(\frac{2h\nu}{E_{g,ID}}\right),\ {F_2}^{ind}\left(x\right) = \frac{\left(2x-1\right)^4}{\left(2x\right)^7} \tag{38}$$

Using this and data obtained by Sinclair et al.[39], the beta coefficient can be defined as shown in Fig.14.

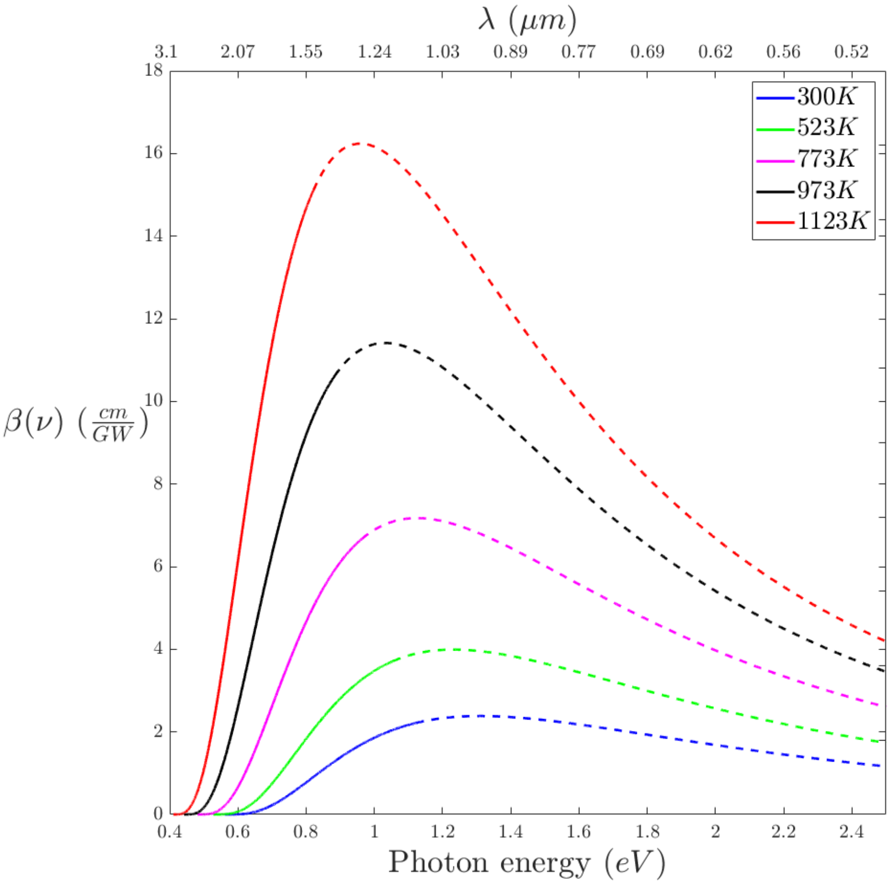

Figure 14: 2-photon absorption coefficient β_2 with increasing temperature

2.4.7 Complete Model

Assembling the findings for both the intrinsic band-to-band absorption and the free carrier absorption into a common model yields the absorption spectrum shown in Fig.15.

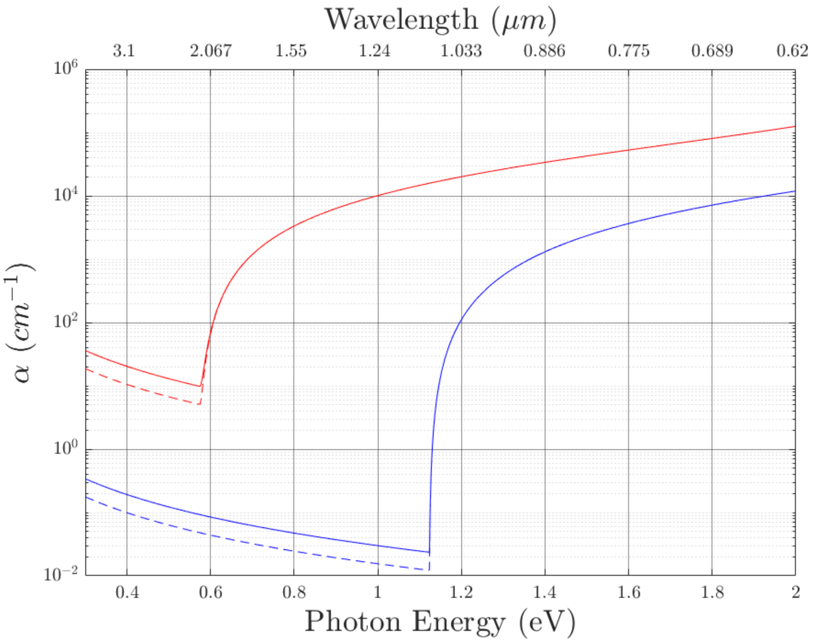

Figure 15: Complete model for room temperature and near the melting point

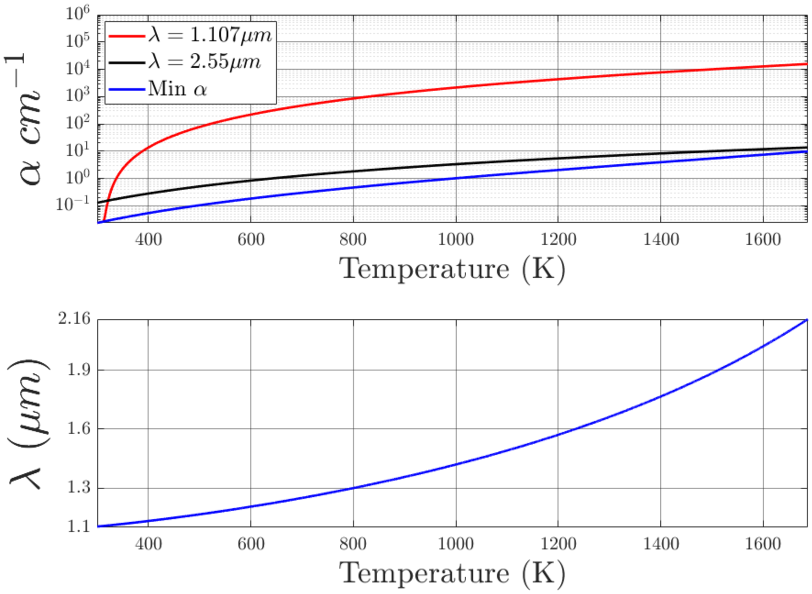

Figure 16: Top: absorption coefficient for select wavelengths compared to minimum
Bottom: wavelength corresponding to minimum absorption

In Fig.16, the absorption coefficient for the room temperature band gap wavelength of $1.10\mu m$ is shown in comparison to $2.55\mu m$ and the minimum absorption whose wavelength is shown in the bottom plot.

3 The Czochralski process

As mention in Sec.1, the Czochralski method is the most common way to produce semiconductor material due to its high scalability and the low production costs. This section will be describing the process how it came to be what it is today.

3.1 The basic principle

The operating principle of this method is that when the free atoms of the melt are allowed to solidify onto an established crystalline structure, then the the atoms will become a part of the pre-existing lattice.
The reason why this happens is that the lattice is a structure composed of Silicon atoms bound together through covalent bonds, where each atom achieves a lower energy state by sharing an electron with four other atoms. This bonding causes the lowest energy state of a collection of atoms to be one where they are arranged in a diamond pattern. This interlocking pattern of cubic cells is what forms the crystalline structure and causes the periodic electromagnetic field that drives new atoms to solidify in the same pattern, thus growing the crystal.

In the Czochralski method, a seed crystal provides the initial ”template” lattice to which the material of the melt solidifies onto, from there the newly grown parts of the lattice do the same for the following material.
The growing process therefore starts with the seed crystal being dipped into the melt, initiating the growth process. Then, the crystal is then grown by keeping the melt just above its melting temperature while the solid crystal is being cooled, driving more material to grow onto the crystal.

This is the common mechanism for all three methods mentioned in Sec.1, the difference being how the process proceeds from there.
In the Float-Zone method, the crystallization front is advanced by moving the plane where heat is applied away from the solidified crystal, allowing the direction of cooling to be away from the crystal. Opposite to this, the Czochralski method instead moves the crystal relative to a stationary heat source by pulling the crystal up from the melt. This is then controlled so that the crystallization front, forming the crystal-melt interface, remains stationary relative to the melt surface as the crystal is grown.

3.2 History of development

The method was first invented in 1916 by its namesake, polish chemist Jan Czochralski [6] when he discovered that dipping a metallic tip into an under-cooled molten metal and slowly raising it as the metal began solidifying onto it would produce a thin rod of mono-crystalline material. Amongst those familiar with the history of this process, it is a popular belief that this discovery was made by accident when Czochralski accidentally dipped his pen in a crucible of molten tin instead of his inkwell, creating a crystalline filament. Czochralski moved on to create an apparatus (Fig.17) specifically to investigate this effect, this experimental setup consisted primarily of a tipped weight on a vertical carrier leading down to an open crucible containing molten tin. This setup was far from anything seen today and could only produce very thin, short rods of tin, but it was the start of something that revolutionized the world.

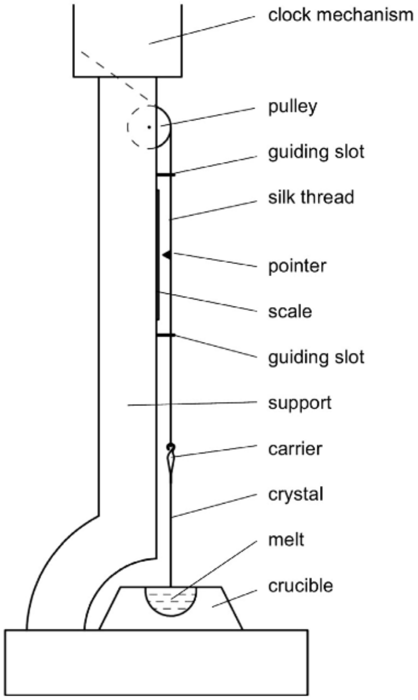

Figure 17: Schematic of Czochralski's original apparatus [6]

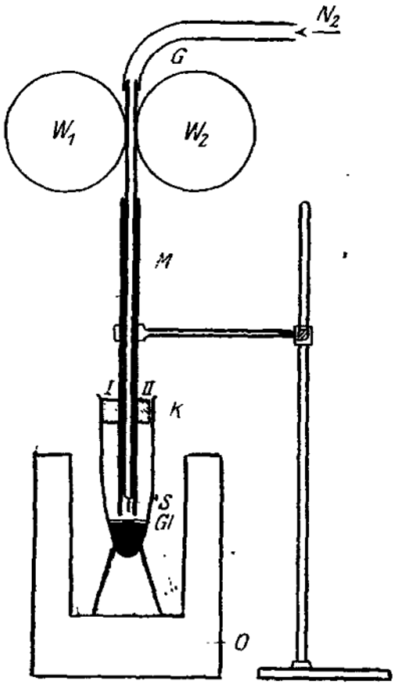

Figure 18: Schematic of Gomperz improved setup [7]

In the early days, this was little more than a curiosity, but it was enough to catch the interest of many chemists and metallurgists including E. von Gomperz [7] who in 1922 took the method to its next step. The setup (Fig.18) of Gomperz differed from Czochralski's original design in many ways, it used gas to cool the dipping assembly and was partially closed instead of open, but most importantly, it was the first to employ the use of a seed crystal. The seed crystal greatly improved the device's ability to form crystals, allowing Gomperz to grow crystals out of not only tin, but other metals, like Aluminium and Zinc. The use of a seed also meant that the interface between the crystal and the melt did not rely on simple adherence as it did in Czochralski's design but instead exploited capillary forces to bridge the two, this allowed him to produce thicker rods of material and made the process more robust, which made it possible to pull significantly longer crystals.

From there on, the technique was gradually refined to produce larger crystals from many other materials but the design remained largely the same. It was not until 1937 when Henry Walther [8] published a paper on the use of a Czochralski-derived method of producing cylindrical ingots of mono-crystalline NaCl. The design he described (Fig.19) was largely the same as what Gomperz had created 15 years earlier but introduced both the use of rotation and gas cooling of the crystal. Walther theorized that by rotating the crystal as it is being grown one could not only force the crystal to become cylindrical, but also greatly increase ones control over the growth process by discouraging anomalous lateral growth.

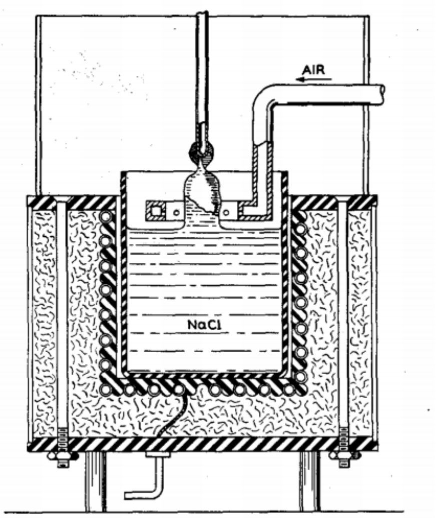

Figure 19: Schematic of Walther's setup [8]

Development of the process kept going, many experiments were conducted to improve the process, such as the experiments of A. G. Hoyem and E. P. T. Tyndall [9] in 1929 that investigated the conditions required for the growth of mono-crystalline zinc and the relations between the factors of those conditions. They also discovered that the appropriate temperature gradient varied with crystal orientation, a seemingly small but very important fact.

Those experiments then lead to perhaps the most important change in the process when, in 1948, Gordon K. Teal and J. B. Little [6] managed to create a rod of single-crystal Germanium, the first semiconductor material produced using this process. Once the proverbial code was cracked, it didn't take long before other metalloids were produced using the same technique, with the first Cz-Si being pulled in 1949 by Teal and E. Buehler [6].

It was during this time that physicists like William Shockley began using semiconductor-based junction devices, such as the Bipolar Junction Transistor (BJT) invented by Shockley and his team in 1947 [6]. This then made the Czochralski method much more attractive both to the scientific community and the business world, leading to a greatly accelerated rate of development in the following years, enabling the production of larger and larger crystals.

Throughout the 1950’s labs around the world also began producing compound semiconductor materials, most notably Gallium arsenide (GaAs) in 1958 [10]. This is also used in high-efficiency PV cells where it outperforms Silicon-based cells, but due to higher costs and lower scalability it is mostly used in special, small scale applications, like aerospace. GaAs has, however, seen wider use in various electronics since it outperforms Si-based technology in operating frequency and noise ratios, it is also widely used in light emitting applications.

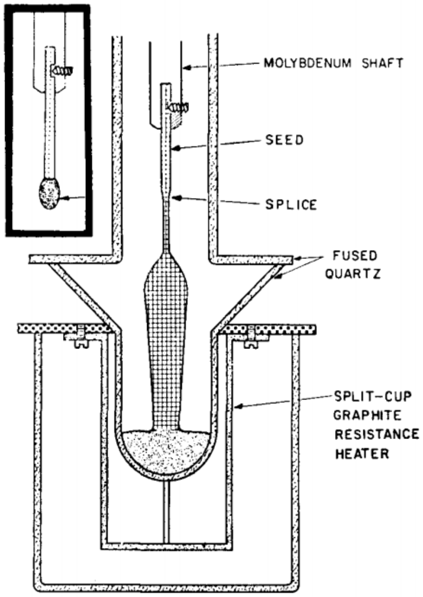

Figure 20: Schematic of a furnace for pulling Cz-Si with a ”Dash-neck” [11]

While compound semiconductors were being developed, improvements to the Czochralski method for Silicon was largely focused on increasing yield and crystal diameter. Until William C. Dash [11] developed an improved technique in 1959 that it became possible to grow crystals without the extensive dislocations seen by Teal and Buehler. Dash discovered that by pulling a thin strand of crystal from the seed prior to growing the main body of the crystal allowed the growth process to stabilize and eliminate dislocations emerging from the seed crystal. Dash also discovered that in order to remove the dislocations during pulling of this ”Dash-neck”, the optimal growth conditions must be adapted to the orientation of the desired crystal orientation.

Throughout the 1960’s and 70’s the increasing availability of high-grade monocrystalline semiconductor materials made it possible to develop increasingly complex electronics, such as the microprocessor in 1971. This lead to the process, in a sense, self-improving by employing more advanced semiconductor-based electronics to achieve a higher degree of control and automation, allowing for faster production and larger boules.

3.3 Modern process

At its core, the modern Czocrhalski furnace (Fig.21) is very much alike the setup devised by Walther (Fig.19) or Dash (Fig.20). Although modern furnaces feature a number of improvements devised over the past 50 years, such as automation and improved thermal designs.

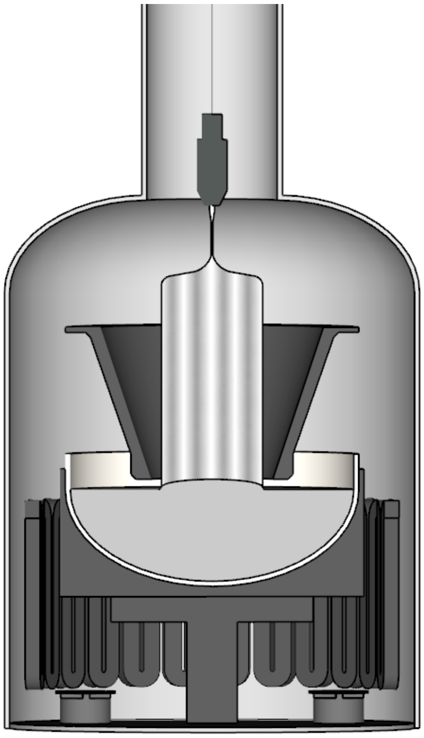

Figure 21: Conceptual schematic of a modern Czochralski furnace

Components of the furnace

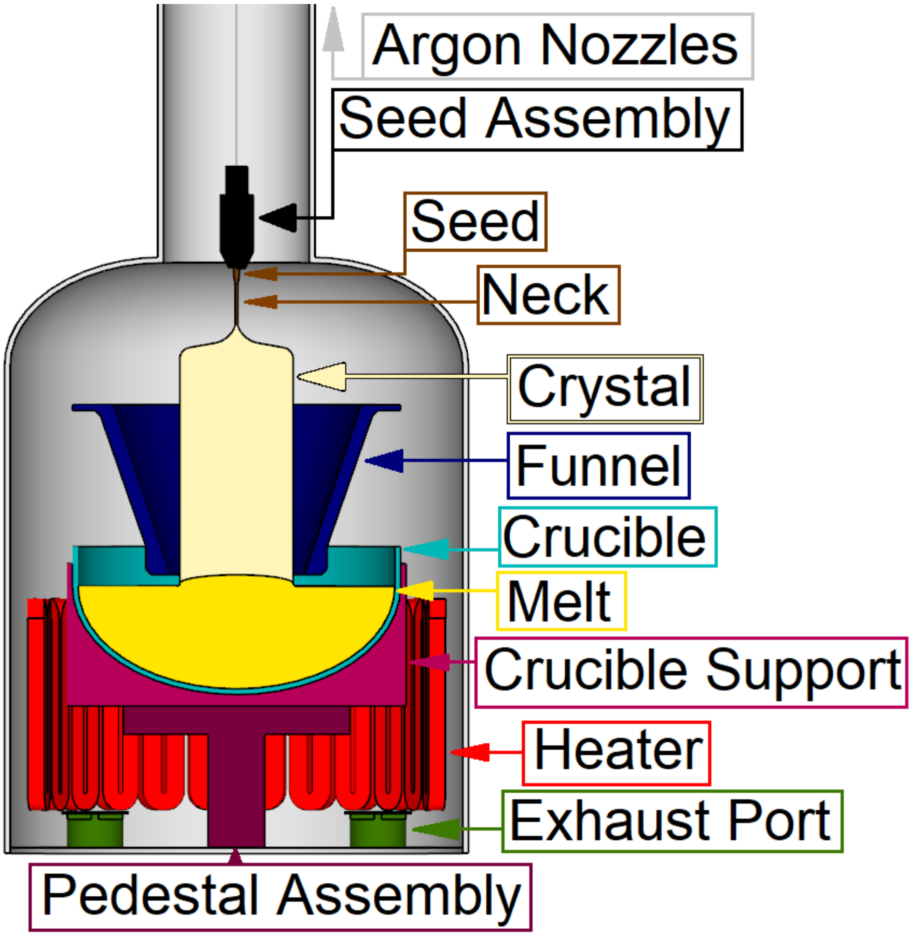

Figure 22: Labeled schematic of modern CZ-furnace

In Fig.22 we see the same schematic as shown in Fig.21, but color coded and labeled.

We can see the commonalities between this design and that of Czochralski's original design (Fig.17) in that they both have a stationary crucible containing the melt, and a movable carrier from which the crystal grows from. The differences begin with what was the carrier in Czochralski's original apparatus, where a modern furnace instead uses a seed crystal suspended from a weighted assembly, like what was introduced in the design of Gomperz (Fig.18). From the design of Walther (Fig.19), the modern furnace also feature rotation of both the seed assembly and the pedestal assembly, rotating the crystal and the crucible in opposite directions. The crystal growth also includes the "neck" introduced by Dash (Fig.20) to produce a dislocation-free crystal.

In addition to these features, the modern furnace also includes a funnel assembly, somewhat similar to what was depicted in the schematic of Dash's setup. This funnel is commonly a composite assembly consists of three main sections:

- A thick outer shell of high-density graphite designed to block the thermal radiation coming from the melt and lower furnace.
- A low density graphite foam to insulate the inner assembly from the outer radiation shield.
- A thinner, inner shell facing the crystal, designed to direct the flow of argon towards the crystal as well as reflect the thermal radiation emitted by the crystal up and away to aid cooling.

As shown by Huang et al. [12], the design of this funnel and the other insulation components not shown here can have a strong effect on both the power consumption and the thermal stress. The geometry of this assembly naturally also effect the atmospheric flow conditions near the melt surface, which was shown by Teng et al. [13] to have a direct effect on the Oxygen contamination of the crystal.

Another important feature of modern furnaces is the inert environment surrounding the crystal and melt. While the design of both Dash and Gomperz both touched on this by having at least a partially closed furnace modern furnaces are instead hermetically sealed and have a highly controlled internal atmosphere. Aside from a small concentration of CO and particles of Silicon oxides, the atmosphere is comprised purely of inert gas, usually Argon. The Argon is introduced by a spreading nozzle at the top of the furnace and flows downwards towards the exhaust ports, providing a small amount of cooling but mostly serves to drive the airborne contaminants (CO , SiO and SiO_2) away from the crystal and melt. This flow is relatively gentle, commonly having a mean flow velocity in the range of $0.95 - 2.15m/s$ [14] while being regulated by the extraction rate at the exhaust so that the furnace pressure is kept at very low pressures, commonly below $6.7kPa$ [14].

The crucibles are almost exclusively made from fused Quartz, like the ones shown in Fig.23, much like what was depicted in the Dash's design (Fig.20) from 1959, albeit their shape has changed as the amount of Silicon melt has increased.


Figure 23: Image of fused Quartz crucibles produced by Momentive Quartz

Quartz (SiO_2) is used in this process due to it being non-reactive with the molten Silicon which is paramount as the high temperatures ($\geq 1687K$) required to keep the melt from freezing, also makes the material highly reactive if a compatible contaminant is introduced. If such contamination occurs then the quality of the material will be influenced and can, in extreme cases, interfere with the growth process, leading to a premature termination of the process.

One of the major challenges with using a Quartz crucible is the fact that at the required temperatures, the crucible becomes largely plastic, having a structural integrity comparable to used chewing gum. Because of this, a crucible support assembly, commonly made from dense graphite, is tasked with maintaining the shape and integrity of the crucible so that the crucible itself only serves as an inert barrier between the melt and the support assembly.

Another factor when using Quartz is that once heated, especially during the initial heating, the quartz reacts to the presence of Carbon which is deposited by the graphite of the funnel and other heat shield components. This reaction can then produce Carbon monoxide(CO) and Silicon monoxide(SiO), the latter of which can degrade further to produce Silicon and Oxygen:

$$\begin{matrix} SiO_2 + C \rightleftharpoons SiO + CO \\ SiO_2 + Si \rightleftharpoons 2SiO \end{matrix} \rightarrow 2SiO \rightleftharpoons 2Si + O_2$$

This provides a source for Oxygen contamination in the crystal and commonly reacts to the Silicon at the surface of the melt to produce molecular SiO_2 which accumulates in the lower furnace as a yellow dust or a granular solid. This limits the maximum production cycle of modern furnaces as the exhaust filters and ports eventually become clogged, which in term disrupts the Argon flow and allows the oxides to contaminate the crystal and melt.

Stages of the process

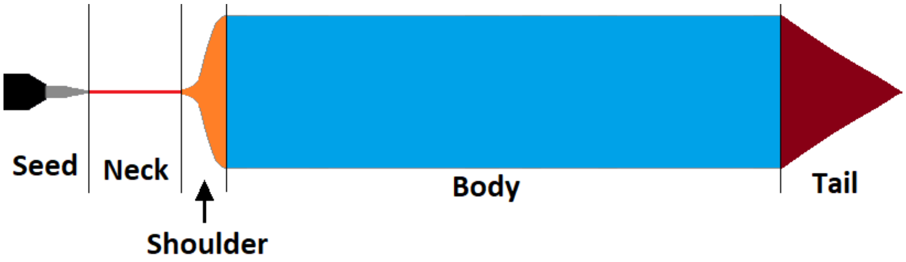

Figure 24: Labeled illustration of the sections of a finished boule

The process is largely divided into five principal stages, with the last four stages corresponding to a distinct section of the finished boule as show in Fig.24.

3.3.1 Melting

The first stage is naturally the melting stage, this is generally preceded by a flushing sequence wherein the atmosphere is repeatedly removed and replaced with Argon to ensure atmospheric purity. The melting stage itself is, in principle, very simply a stage where the crucible is heated while being slowly rotated, but due to other effects such as the Oxygen reaction previously mentioned, the events in this stage can have a significant effect on the finished material.

During this stage the main control mechanisms are the heater effect and gas flow, both of which are employed to melt the raw material while removing the released by-products.
In the beginning of this stage, the heater is generally set to at or near is maximum effect to expedite the process while the gas flow and pressure is maintained at a moderate level. As the material begins to melt, the heater effect is lowered to stabilize the melt temperature while the gas flow is increased to allow for the released Oxygen, CO and SiO to be evacuated before the process continues.

3.3.2 Neck

As shown in Fig.25, this is the stage where the technique developed by Dash enters the process. In general, the pull and rotation rate in this stage is higher than for the other stages of the process due to the low diameter of the crystal at this point.

But, as noted by Dash [11] the orientation of the crystal structure is a factor when attempting to remove the dislocations when growing a "Dash-neck". As Dash discussed, the preferred crystal orientations for this process are the ⟨100⟩ and ⟨111⟩ as this prevents screw dislocations from develop along the vertical axis. This in term prevents the dislocations from presenting a good surface lattice at the growth front, resulting in the dislocations terminating as they reach the lateral sides of the crystal.

This means that if the seed crystal orientation is ⟨100⟩ then the the axis of any screw dislocations will be normal to this, and to the vertical axis, thus it is preferred to have a smaller diameter so that the dislocations grow out and terminate faster. If the orientation is ⟨111⟩ then the screw dislocations grow along a 45° angle relative to the vertical axis and therefore it is preferable to have a higher rate of growth, meaning higher pull speed, in order to eliminate these dislocations.

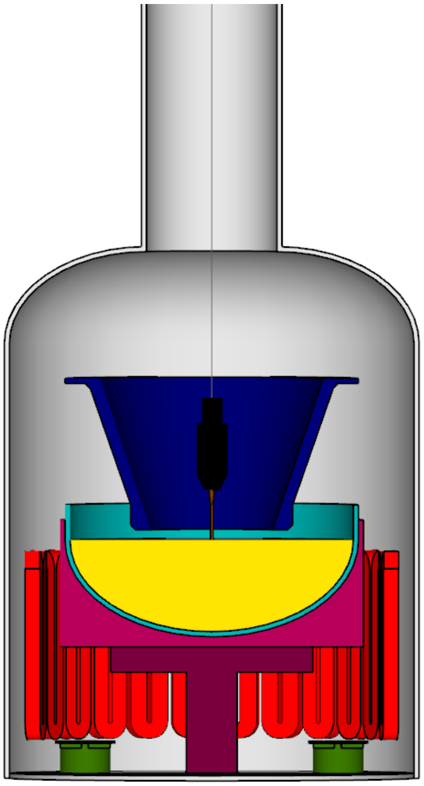

Figure 25: Simplified cross-section of the furnace near the melt surface during the necking stage

3.3.3 Shoulder

In Fig.26 we see the cross section of the crystal during the shoulder stage. The purpose of this stage is to increase the diameter of the crystal in advance of the growth of the usable mass of the body section. This is done by greatly lowering the pull rate so that lateral growth can occur while the rate of rotation is kept at a moderate rate so that anomalous growth is deterred which maintains the circular shape of the outer perimeter of the growth front.

Due to the high surface area relative to the current mass of the crystal and the fact that its surface is almost flat near the crystal-melt interface, the radiative cooling during this stage will cool the crystal rapidly. This causes the interface to form a conic shape that stretches downwards into the melt and often presents with four flattened bands expanding radially from the center of the shoulder where the neck meets the shoulder. These bands are artefacts of the cubic lattice structure of Silicon which drives the crystal to from square or cubic macroscopic shapes. While the overall shape of the crystal remains largely cylindrical, thanks to the rotation introduced by Walther [8], this can still be seen by four lines, commonly referred to as the "nodes", on the side of the crystal along the direction of growth.

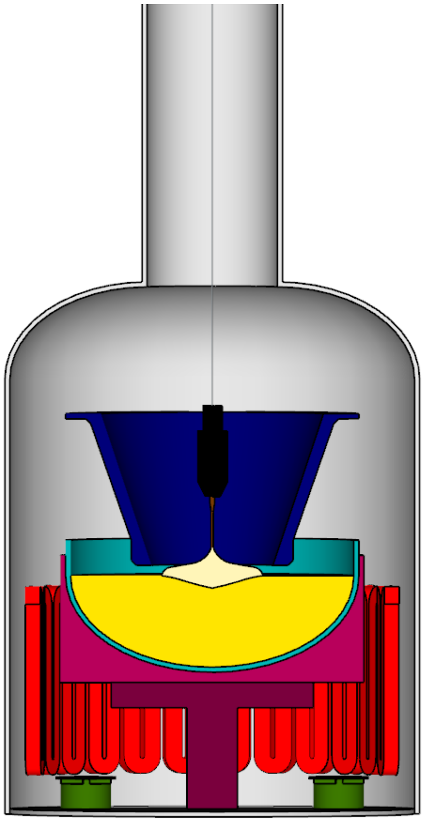

Figure 26: Simplified cross-section of the furnace near the melt surface during the shoulder stage

3.3.4 Body

In Fig.27 we can see the cross section of the crystal as the main body of the boule is being produced, this is also the same as depicted in Fig.21 and Fig.22.
As shown in Fig.24, this stage stretches along the majority of the final length of the boule and is where most of the mass is. Because this is the section that produces the usable material that will later be cut into wafers, it is preferable to grow this section as large as possible as to achieve the highest material yield. This is the reason why the shoulder stage is made so relatively flat in the modern process compared to earlier variants such as those produced by Dash.

It is also worth noting that the shape of the preceding shoulder stage can vary wildly depending on the desired diameter of the body stage, what is depicted in Figs.27 and 26 are examples of the shoulder configuration commonly used for 200mm boules. For the larger 300mm boules that have become increasingly popular in recent years, the shoulder section is often made to be have a more conic shape as to accommodate the larger diameter, weight, and subsequent strain on the crystal.

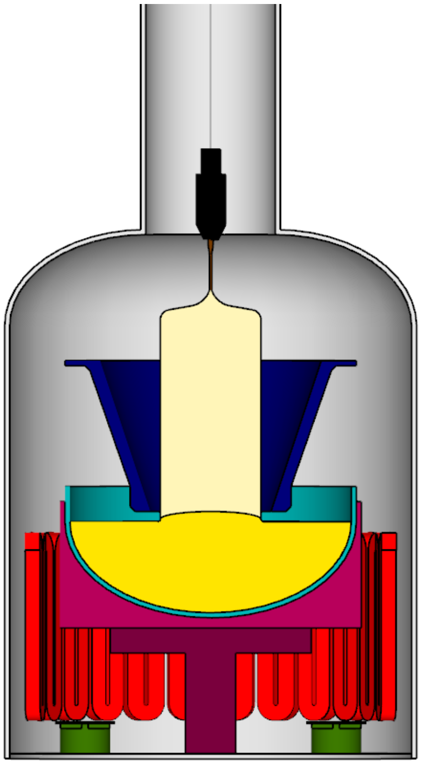

Figure 27: Simplified cross-section of the furnace near the melt surface during the main body stage

3.3.5 Tail

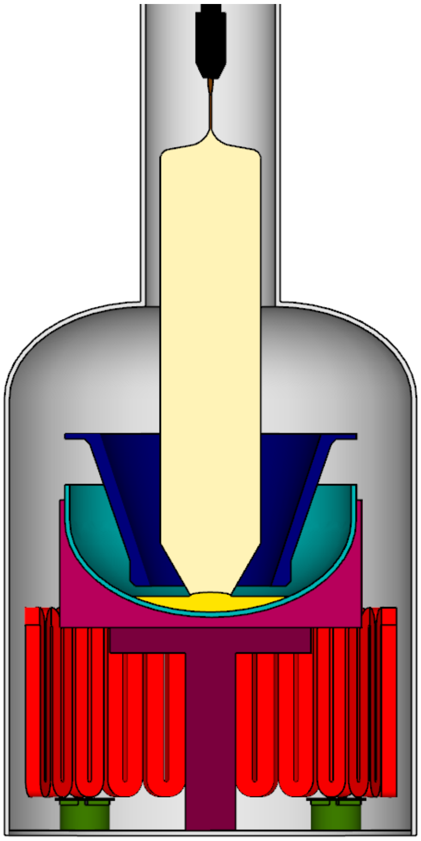

Figure 28: Simplified cross-section of the furnace near the melt surface during the tail stage

The final stage, as depicted in Fig.28, is the growth of a narrowing cone, in essence the reverse of the shoulder, that serves as a controlled termination of the growth process. Due to the high temperatures near the interface the lattice of the newly formed parts of the crystal remains malleable, due to this the shock of separating the crystal from the melt can induce significant slip dislocations in the crystal. The nature of these dislocations is dependent on the crystal orientation as this would dictate the slip planes, for instance a ⟨100⟩ will have slip dislocations at an angle of 45° relative to the vertical axis. Because of this, the extent of the slip dislocations caused by a separation shock is dependent on the radius of the interface at the time of separation, with the industry rule-of-thumb being that the dislocations travel atleast as far up the crystal as the diameter of the separation perimeter. Because of this it is beneficial to reduce the diameter as much as possible before separation and to do this by pulling a cone of lower angle than the expected slip angles so that any shock induced slip dislocations are contained within the tail cone.

3.4 Thermal conditions and crystal-melt interface

As mentioned in the preceding sections, the temperature field in and around the crystal, especially at the interface, is of paramount importance in the successful growth of the crystal, as was investigated by Hoyem and Tyndall [9] in 1929.

3.4.1 Heat exchange mechanisms

Surrounding the crystal, there are five principal heat exchanges:

1. Convective cooling with the Argon flow along the crystal walls and melt surface
2. Convective and conductive heating of the crystal from the melt through the interface, and the reciprocal cooling of the melt
3. Radiative cooling of the crystal and reciprocal heating of the exposed melt and upper heat shield components
4. Radiative cooling of the melt and upper heat shield components and reciprocal heating of the crystal and furnace inner hull
5. Released heat by the freeze energy of the crystal being grown at the crystal-melt interface

1 - Convection with Argon

As mentioned earlier in Sec.3.3, the atmospheric pressure inside the furnace rarely exceeds $6.7kPa$ [14] and has a mean flow rate of $2.15m/s$.
For the sake of simplicity, it is assumed that the atmosphere in the upper furnace consists entirely of Argon, which has a specific heat capacity of $c_p = 0.520\frac{kJ}{kgK}$[14], density of $\rho = 1.784g/l$, and a thermal conductivity of $\kappa = 1.78042 \cdot 10^{-4} {}^{W}\!/_{mK}$[16] at STP. The cooling effect is then given by $Q = h_c A \Delta T$ where we have the relationship:

$$h \propto \rho^{\alpha} {c_p}^{\beta} \kappa^{1-\beta} \tag{39}$$

Considering the simplified example where the crystal is a cylinder of radius 100mm and height 400mm and the gas acts like air with a laminar flow rate of $2.15m/s$ and a temperature difference of $1000K$ then the expected heat transfer effect would be slightly over $7.5kW$.
Taking into account that the pressure is 15 times lower in the furnace and that Argon has a much thermal conductivity it would be realistic to expect a cooling effect that is 15-20 times weaker than the air example, giving an expected effect of less than $500W$, which is negligible compared to other factors.

2 - Heat transfer at the interface

Crystalline Silicon has a thermal conductivity of approximately $21.6 {}^{W}\!/_{mK}$[17] near the melting point and the melt has a thermal conductivity of $45.6 {}^{W}\!/_{mK}$[18] at the melting point.
Combined with a specific heat capacity of $0.957 \frac{kJ}{kgK}$[20] for the crystal and $0.912 \frac{kJ}{kgK}$[22] for the melt at the melting temperature and respective densities $2.29 {}^{g}\!/_{cm^3}$[23] and $2.52 {}^{g}\!/_{cm^3}$[22] at melting point, we would expect the convective heat transfer coefficient to be significantly large.
Also considering the effective flow field over the interface driven by the rotation of the crucible relative to the crystal we can expect that the convection at the interface to be a significant conduit of heat into the crystal.

3 - Radiative cooling of the crystal

Heat transfer by radiation is described by Stefan-Boltzmann's law:

$$P(T) = \epsilon_s \frac{2\pi^5 k^4}{15c^2h^3} T^4 \cdot A \tag{40}$$

Considering the previous example case with Argon where the crystal is a 400mm tall cylinder of radius 100mm with a surface temperature of $1000K$ we see that with a surface emissivity of 0.71[24] then the cooling effect is in excess of $12.8kW$. However, in actuality the gross cooling would be expected to be somewhat higher as the true crystal has a higher surface area due to the shoulder section and the fact that the temperature, especially near the interface, is expected to be higher than what was assumed here.
A good portion of this is expected to be negated due to the radiation both reflected and emitted by the upper shield components, especially the funnel assembly. The exact heat transfer of this depends greatly on the geometry of the funnel and resulting view factor between them, as well as the composition of the funnel and resulting surface temperature of the inner surface. Though, considering that graphite is a near-black body material, with an emissivity often in excess of 0.9, it is expected that this will have a large impact on the cooling of the crystal.

4 - Radiative heating of the crystal from the melt

Another radiative heat transfer effect is the heating of the crystal by thermal radiation coming of the melt. Given that the surface emissivity of the molten Silicon is 0.183 [18] Then the expected total radiant emittance effect is expected to be approximately $21.3kW$ for a full 22" crucible with a surface temperature of $1700K$. Considering that one of the primary purposes of the funnel assembly is to shield the crystal from just this, it is expected that this effect would be relatively minor.
Even if it is assumed that all radiation is absorbed, which is unlikely due to the

shallow angle between incoming rays and the crystal surface, then the size of the window formed by the bottom aperture of the funnel would decrease this drastically.

Commonly, the clearing between the crystal and inner shield of the funnel near the melt is made as small as possible, usually in the area of 2cm depending on production spec and specific funnel design, and the bottom of the funnel being around 1cm above the melt. If we then construct and exaggerated example with an opening of 3cm and assume constant temperature of $1700K$ with a view factor of 1, then the expected heating would have an effect of approximately $1.88kW$, given by Stefan-Boltzmann's law.

Taking into account the mentioned mitigating factors, it is doubtful that this effect would exceed $1kW$ in reality, and this factor becomes negligible as well.

5 - Freeze heating at the interface

The last mechanism is also a rather weak one, but due to it occurring precisely at the interface, where the crystal is most sensitive to heat, it is included.

The freeze heating is when a substance transitions from a liquid state to a solid state, where the ordered nature of solid states wherein atoms (commonly) form covalent bonds that allow them to assume a lower energy state than what was possible in a liquid state. The energy difference must then be released in order for the transition to occur, this energy is called the latent heat of fusion and will effectively act as heat source in the Czochralski-process.

For Silicon, the latent heat of fusion is $50.55\frac{kJ}{mol}$ which equates to $1.800\frac{kJ}{g}$ given that the nominal molar mass of Silicon is $28.085\frac{g}{mol}$. Given that the density of Silicon near the melting point is $\rho = 2.29g/cm^3$ we expect to get a heat generation:

$$Q = H_F \cdot \rho \frac{dV}{dt} = H_F \cdot \rho \cdot \pi {r_0}^2 \Delta l = 1294kW \cdot v_p \left(\frac{cm}{s}\right) \tag{41}$$

Where v_p is the pull rate in cm/s.

This means that if, for instance, the crystal is being pulled at a rate of 10 cm pr. hour, or $2.777 \cdot 10^{-3} cm/s$, then the expected heating effect is $3.597kW$.

3.4.2 Thermal Stress

One of the important factors in preventing the formation of dislocation imperfections in modern crystals is management of the thermals stress induced by the temperature gradient throughout the crystal.
Thermal stress is, simply put, an internal pressure field inside the crystal that occurs due to the different parts of the crystal being cooled, and therefore contracting, at different rates.
The thermal stress is commonly described using the Cauchy stress tensor:

$$\sigma = \begin{bmatrix} \sigma_{xx} & \sigma_{xy} & \sigma_{xz} \\ \sigma_{yx} & \sigma_{yy} & \sigma_{yz} \\ \sigma_{zx} & \sigma_{zy} & \sigma_{zz} \end{bmatrix} = \begin{bmatrix} T_1 \\ T_2 \\ T_3 \end{bmatrix} \tag{42}$$

Where each of the T-vectors correspond to a stress applied to each of the three faces of a cubic unit cell with the components σ_{xx}, σ_{yy}, and σ_{zz} being the stress normal to the faces of the cell.
Due to the Cauchy tensor being so complex, it is often boiled down to a single value, such as von Mises stress. The von Mises stress equates the multi-axial stress described by the Cauchy tensor to a uni-axial stress. This is done by preservation of energy as the associated distortion energy of the Cauchy tensor is determined and from there an associated uni-axial stress of equivalent energy can be determined.
In the general term, this stress is derived from the Cauchy tensor as:

$$\sigma_{vm} = \sqrt{\frac{1}{2}\left[\left(\sigma_{xx} - \sigma_{yy}\right)^2 + \left(\sigma_{yy} - \sigma_{xx}\right)^2 + \left(\sigma_{zz} - \sigma_{xx}\right)^2 + 6\left({\sigma_{xy}}^2 + {\sigma_{yz}}^2 + {\sigma_{zx}}^2\right)\right]} \tag{43}$$

This is useful when evaluating ductile material as experimental data, where uni-axial stress and strain is commonly evaluated, can be compared to more complex structures of two or three dimensions. A shortcoming of the von Mises stress is that it assumes the direction of the true stress is irrelevant, which is more or less true for many plastic or ductile materials, but it is not always so with crystals.
Due to the highly ordered arrangement of the atoms in a crystal, both the stress-strain curve and the associated yield criterion has a degree of anisotropy, and the type of dislocations formed if the yield criterion is exceeded also depends on this. For instance, in Silicon, if the stress is predominantly shearing parallel to the crystal plane then the yield criterion would be lower and the crystal would be prone to slip dislocations. Similarly, if the stress is predominantly shearing normal to the crystal plane then the yield criterion would also be lowered, albeit not as much, and the crystal would then be prone to forming screw dislocations.

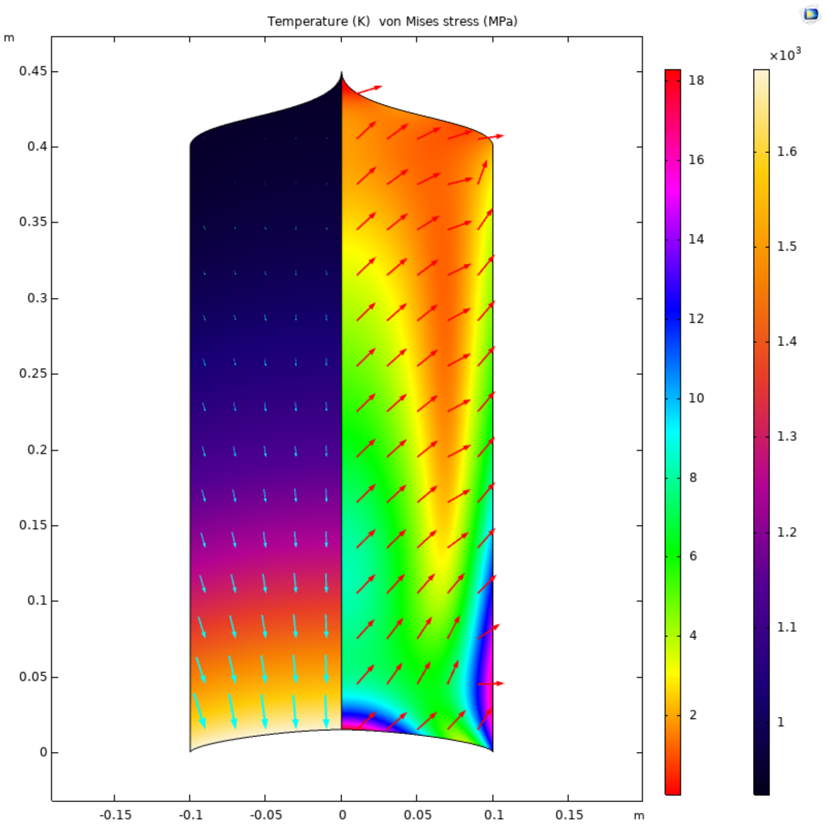

Figure 29: Result of simple simulation showing temperature field with gradient on left side and von Mises stress with net stress direction on right side

As seen in Fig.29, the temperature field is, as expected, simply a gradient from the upper parts of the crystal and walls that increases towards the interface where the temperature is $1687K$.
On the plot of the stress we see that there are two main areas of concern located at the peak of the interface and at the walls near the bottom of the crystal, these areas are where the local temperature variations caused by the heating at the interface and radiative cooling of the walls are the strongest.
It is also worth noting the direction of these stresses, at the hotspot just above the interface we see that the stress direction is angled up and out while at the wall hotspots we see a nearly horizontal stress. If we assume that this is a crystal of orientation $\langle 100 \rangle$ then we see that the crystal planes would make $45°$ angles to the vertical axis, meaning that the shearing force of the stress above the interface peak is close to being in the crystal plane, meaning that this could easily cause slip dislocations.

3.4.3 Interface Shape and thermal stress

Because the interface serves as the principal heat source for the crystal, the shape and deflection of the interface can have a big effect on the temperature field and subsequent induced thermal stress. As can be seen in Fig.30, an increase in the peak interface deflection has a strong effect on the thermal stress in the lower end of the crystal.

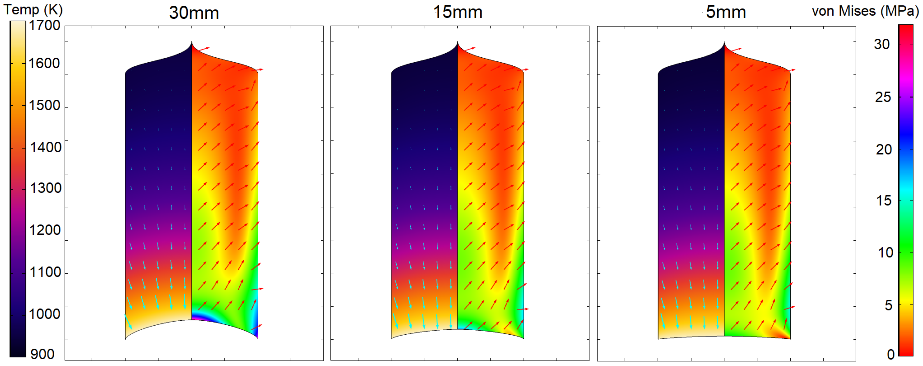

Figure 30: Comparison of stress and temperature field for different interface peak deflections

Note that the interface shape shown in Figs.30, 29, and 27 are all common shapes during the body-stage of the process. As discussed in INSERT SOURCE, the interface shape can vary depending on the process parameters, taking on an ”M”-shaped cross section as a consequence of the melt flow, which is commonly seen with high crucible/crystal rotation rates or with large-diameter (300mm+) crystals.

Though, for the purposes of this project, 200mm crystals grown using nominal parameters will be considered, and thus the interface will be evaluated as a concave parabolic surface of varying height.

4 Simulation

To provide an underlying frame of reference for this project, a simulation of the conditions in and around the crystal is computed. This simulation is done using COMSOL multiphysics 5.4/5.5 and will be designed as a 2D axis-symmetric stationary simulation. A stationary simulation as a snapshot of the conditions at a body-length of 400mm was chosen as the full growth process is needlessly complicated for the purposes of the project.

4.1 Geometry

This furnace design is loosely based on PVa TePla's EKZ-series Czochralski furnaces and is intended to serve as an example of a generic furnace design.
The crystal, marked in blue, is set at 200mm and a length of 400mm from the triple point intersecting the melt to the beginning of the shoulder cone. The crucible, shown in green, diameter is set as 600mm, slightly larger than the commonly used 22" used for this crystal diameter, and a fixed thickness of 10mm. The funnel design here is a composite design using a thick (5-6mm) outer layer and a thinner (2-3mm) inner layer, both comprised of dense graphite, these are then separated by a layer of high temperature insulation, here graphite felt. The funnel assembly is then held by a supporting plate of 7mm thick graphite, the purpose of which is to hold the funnel and direct the argon flow towards the lower furnace chamber. The funnel support then rests on a 1cm thick upper shield tube of graphite. The miscellaneous shielding of the lower furnace is separated into three components, all of which are 1cm thick and comprised of graphite. The lower furnace shields are separated from the inner hull of the furnace by insulation, here modeled as a single piece of graphite felt. The crucible support assembly is a simple cylindrical mould of graphite fit tightly around the crucible and has a minimum wall thickness of 40mm and a 20mm bottom thickness. The pedestal assembly is here modeled as a single-piece graphite component as the separation of components here mainly serves mechanical purposes and is thermodynamically irrelevant.

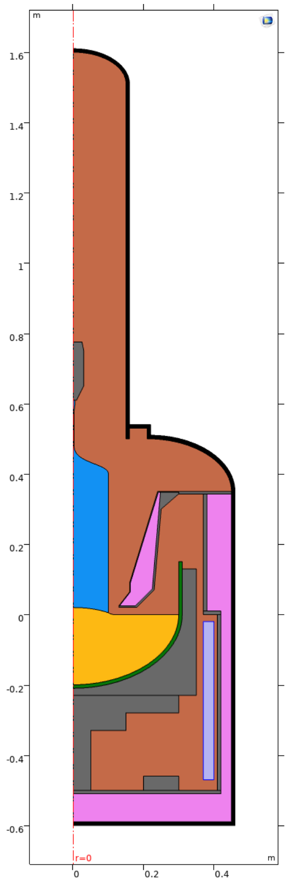

Figure 31: Cutaway of the simulated furnace geometry

4.2 Physics effects

Radiative heat transfer

The radiative heat transfer that dominates this system is emulated using the "Surface-to-Surface Radiation" physic in COMSOL multiphysics with every boundary facing the gas envelope being defined as a diffuse surface.

Conductive and convective heat transfer

The conductive and convective heat transfer is modeld using the "Heat Transfer in Solids and Fluids" physic which is applied over all domains of the simulation, with only the melt and the gas envelope being defined as fluid. The heater is emulated by defining it as a domain heat source of a specified constant power and allowing the heat transfer effects to carry the generated heat to the crucible. The freeze heating discussed in Sec. 3.4 is emulated as a boundary heat source at the crystal-melt interface, this is set to a fixed effect equal to the estimated freeze energy associated with a specific growth rate. A heat flux is applied to the outer boundaries of the furnace hull and a convective heat flux is applied, using water at 20C at a fixed flow velocity, this is done because a real furnace would have water cooling between the inner hull depicted here and an outer hull.

Gas flow

The gas flow is modeled as a turbulent flow using the "Turbulent Flow"-physic in COMSOL. This flow model is set as a compressible flow without swirling flow due to the high directionality of the flow. The inner boundary of the top of the furnace hull is defined as an inlet with a specified mass flow rate as its boundary condition. The outlet is naturally placed at the top boundary of the exhaust ports and is set as a pressure controlled outlet with the desired furnace pressure as to emulate the pressure control loop of the actual exhaust system. The turbulent flow is then coupled with the heat transfer physic through the "Nonisothermal Flow" interphysics bridge of COMSOL.

Thermal stress

The thermal stress is simulated using the "Solid Mechanics"-physic bridged to the heat transfer through the "Thermal Expansion" bridge of COMSOL. This is only defined for the crystal, which is defined as an isotropic linear elastic material.

4.3 Simulation mesh

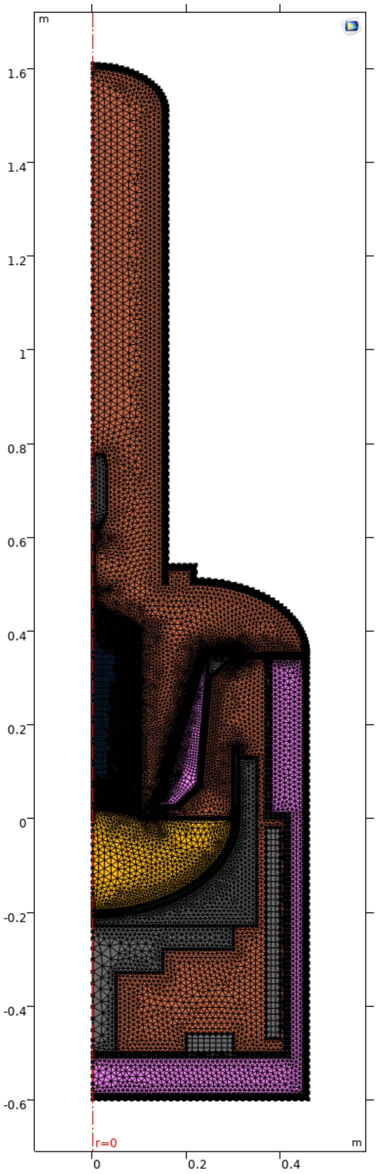

Figure 32: Overlay of physics mesh over geometry

The mesh structure and element size for each domain is defined with the highest density being around the crystal, as can be seen in Fig. 32. The mesh for strictly rectangular domains such as the heater and exhaust port are set as simple mapped rectangular elements with a max element size of 1.29cm. The furnace shielding as well as the crucible support are defined as a triangular mesh with a max element size of 5cm. The furnace tank insulation and pedestal assembly is defined as a coarse triangular with max element size 15cm. The domains of the crucible and funnel, including funnel support and insulation, are meshed using a fine quadratic mesh with max element size 6mm. The fluids, both melt and gas envelope, are meshed as a triangular with max size 1.6cm. The mesh of the crystal is a fine triangular of max size 5mm.

In addition to this, a two-layer boundary layer mesh is applied to all edges between the crystal, melt and gas envelope. Adaptive remeshing is also applied to the crystal, allowing for 2 alterations with an element growth factor of 1.2.

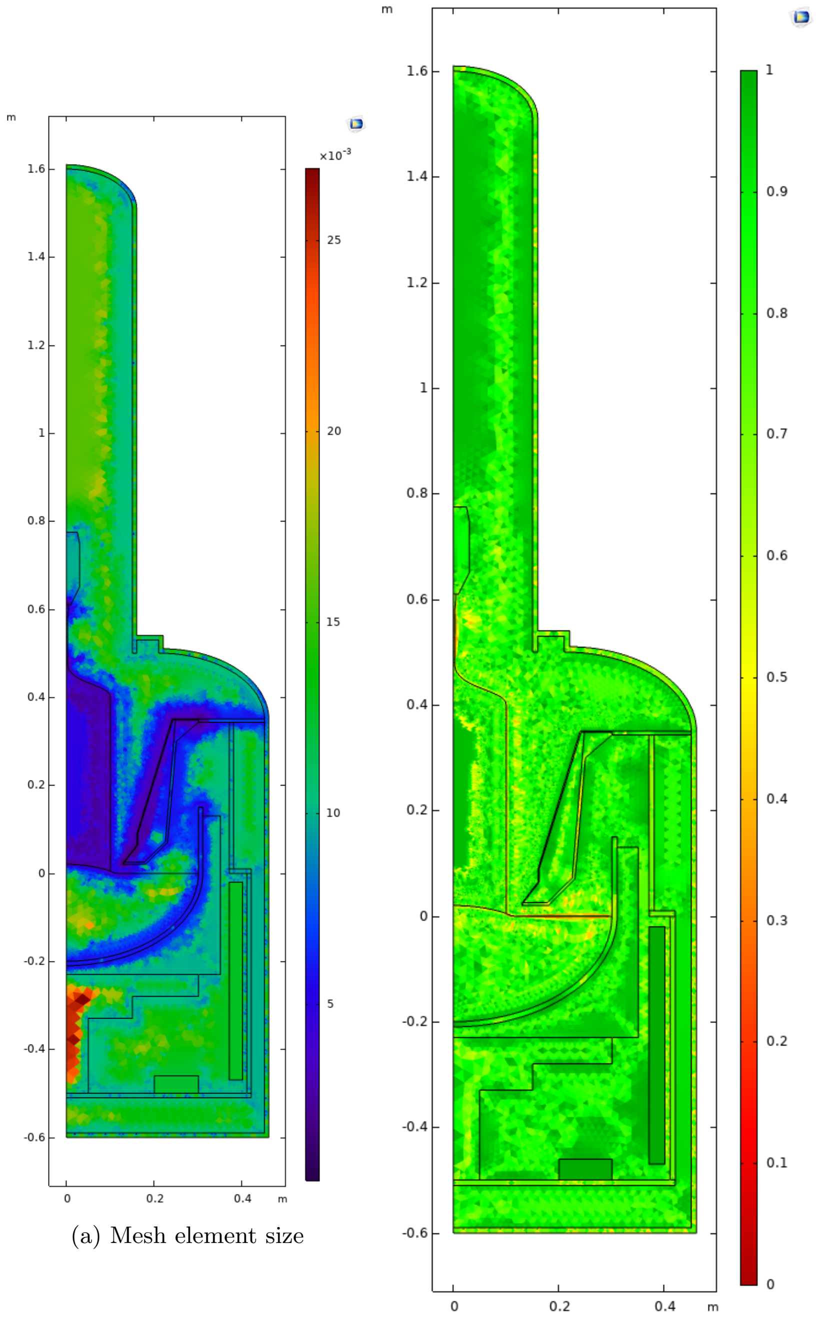

(a) Mesh element size

(b) Mesh element quality

Figure 33: Mesh metrics

4.4 Simulation Results

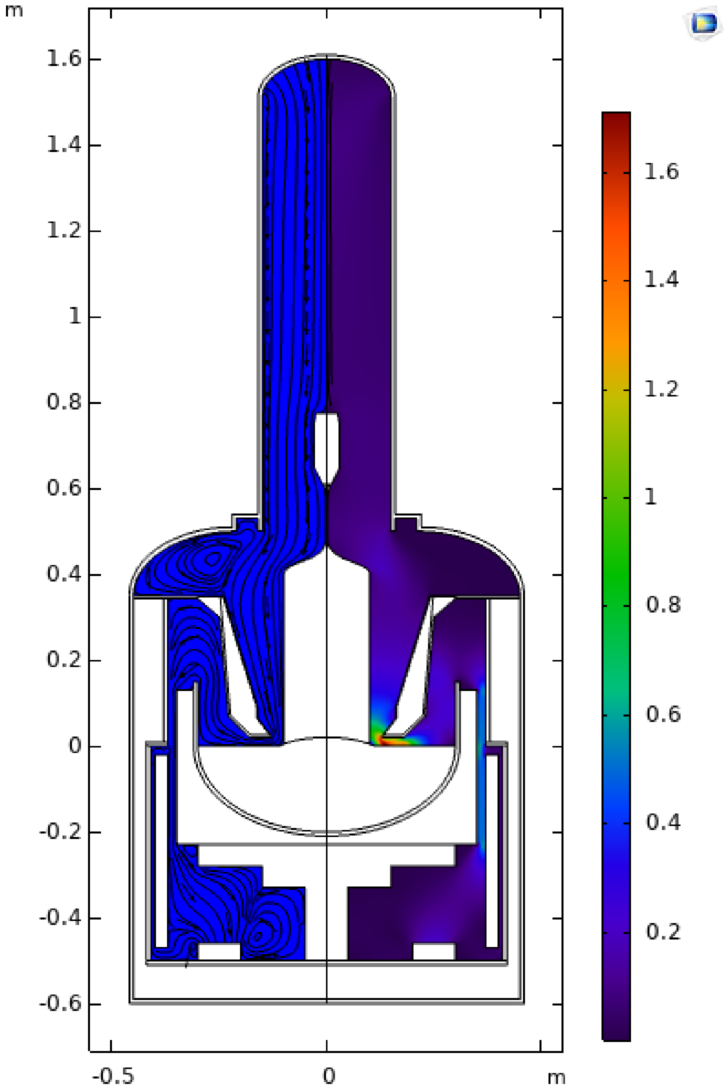

Figure 34: Gas flow results showing flow velocity in m/s on the right and flow lines on the left

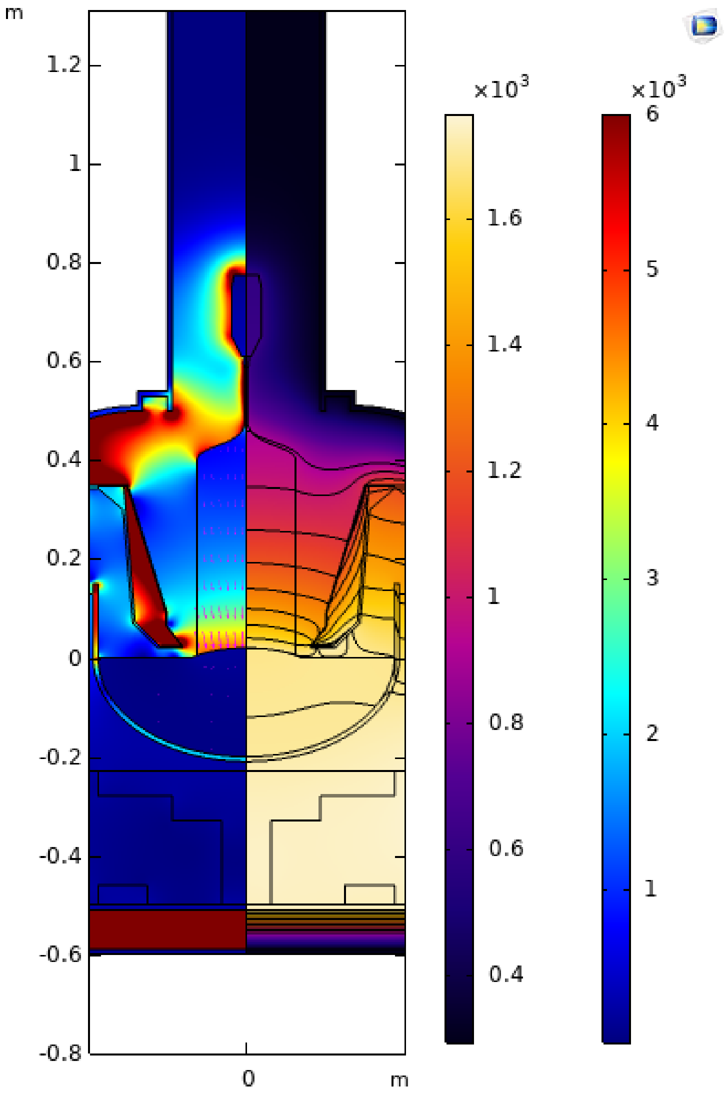

Figure 35: Temperature plot showing temperature field to the right and gradients to the left

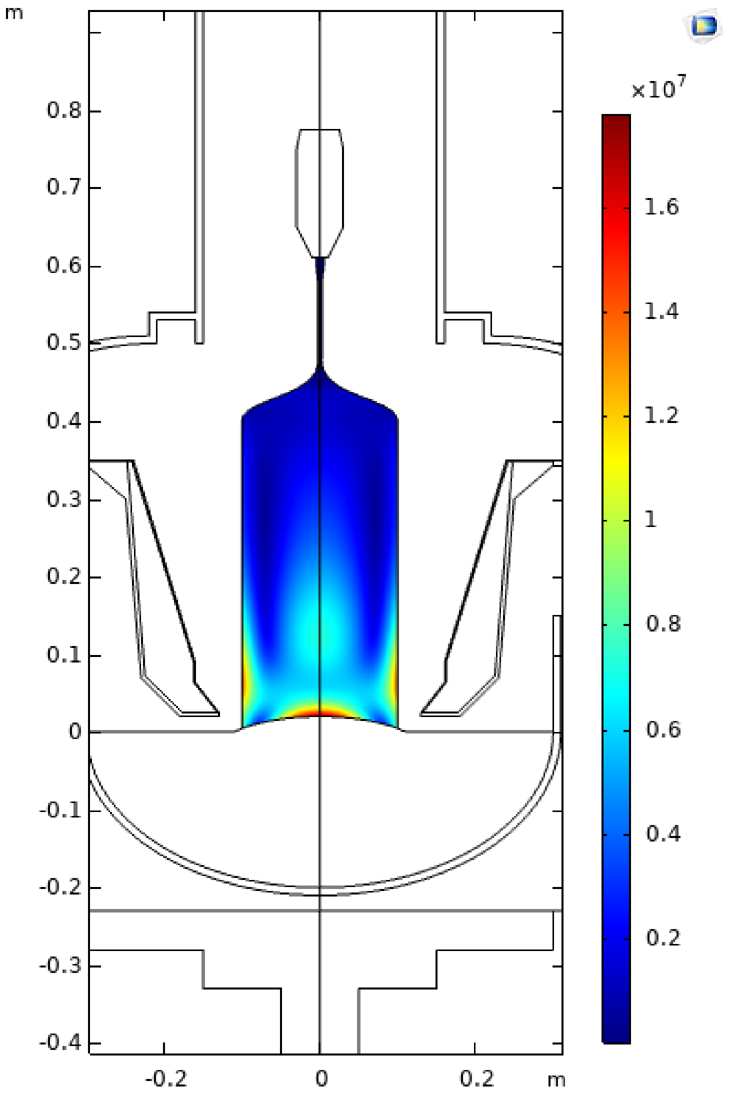

Figure 36: Thermal stress induced by gradients, von Mises (Pa)

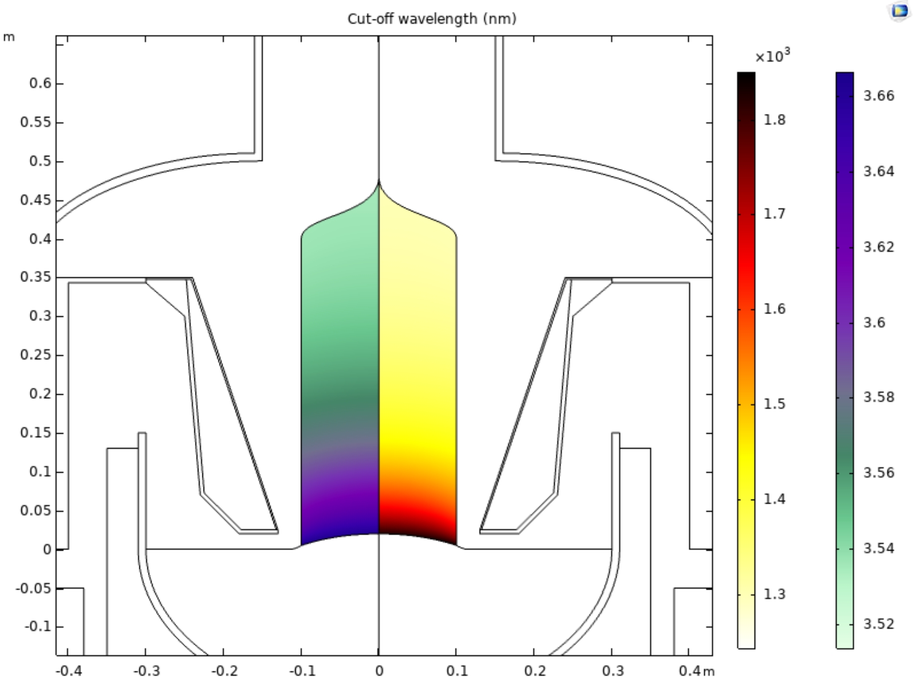

Figure 37: Additional plot showing the optical properties of the crystal with band gap wavelength on the right in nm given by Varshni's equation[41] and estimated refractive index on the left given by Frey[43]

5 Measuring methods

5.1 Transmittance scan

5.1.1 Principle

The transmittance scan method is where a laser beam is aimed at a normal angle to the side of the crystal, either via a mirror assembly or directly as shown in Fig.38, while a detector assembly on the opposite side attempts to capture the transmitted beam. The principle is then that if the beam travels through the bulk of the crystal then it should be attenuated as described by the model of Sec.2.4.4 and should then be detectable. If the beam instead intersects the interface then the metallic nature of the molten silicon will reflect the beam, causing it to significantly deviate, which would in term decrease the transmittance due to a longer beam path and non-normal angle to the crystal wall upon exiting. It should then be possible to determine the interface peak height by laterally scanning the crystal by varying the entry height of the laser beam and denoting the interface peak as the point where the exit-beam can no longer be captured, either from deflection or attenuation.

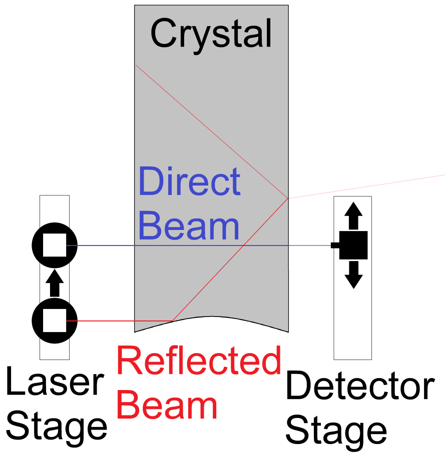

Figure 38: Simple sketch of experimental setup

5.1.2 Benefits and challenges

The benefits of this method is its simplicity, since the angle of incidence is approximately normal to the crystal walls, it is inherently less sensitive to misalignment and errors. This robustness combined with the expected high quality of beam capture and high transmittance makes this method a relatively practical and reliable method of determining the interface deflection.

The challenges of this method are then the unknown angle the beam makes with the local surface of the crystal due to its texture, this then means that as the detector moves further away from the crystal walls, it would have to cover much more area to capture the beam. Since, in an actual furnace, it would naturally not be possible to have either detector or laser anywhere near the crystal due to the high temperatures, it would be necessary to rely on reflectors to relay the beam. A problem here is that since the beam is now orthogonal to the growth axis then the lowest point this method could scan would be at the height of the bottom of the mirrors. Even assuming that reflectors that could handle temperatures in the region of 1500K, this practically limits the minimum scan height to at least 10mm, as placing the mirrors lower than this would interfere with the function of the funnel assembly.

5.2 Interface reflection

5.2.1 Principle

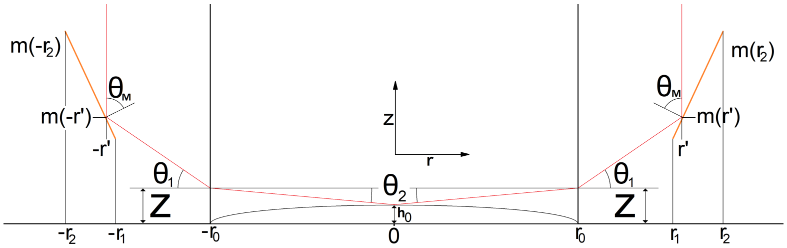

Figure 39: Simple sketch of beam geometry

The principle of the reflection method is to aim a laser into the crystal at an oblique angle in attempt to get the beam to reflect off of the pseudo-flat peak of the interface as is shown in Fig.39. Since the peak of the interface is presumed at the center, this implies that if a beam can be reflected off of the interface such that its path is symmetrical about the central axis of the crystal then it must hit the interface peak. If such a point can be found then the height of the peak can be estimated as:

$$\widehat{h}_0\left(r'|\theta_M, r_0, m\left(r\right)\right) = m\left(r'\right) - \frac{r' - r_0}{\tan\left(\pi - 2\theta_M\right)} - \frac{\sin\left[2\theta_M - \frac{\pi}{2}\right]}{\sqrt{1 - \frac{n_{Ar}{}^2}{n_{Si}{}^2}\sin^2\left[2\theta_M - \frac{\pi}{2}\right]}}\frac{n_{Ar}}{n_{Si}}r_0 \tag{44}$$

5.2.2 Benefits and challenges

The benefit of this method versus the transmittance scan is that the beam is no longer orthogonal to the central axis and thus the requirement that the reflectors be placed at the bottom of the funnel assembly and the subsequent limitation no longer apply.

While the same challenges apply to this method as for the transmittance scan, the inclusion of additional angles and the reflection off of the interface makes this method highly fragile. As shown in Figs.40 and 41, deviation in either the angles of the mirrors or in the laser can cause significant errors in measurement.

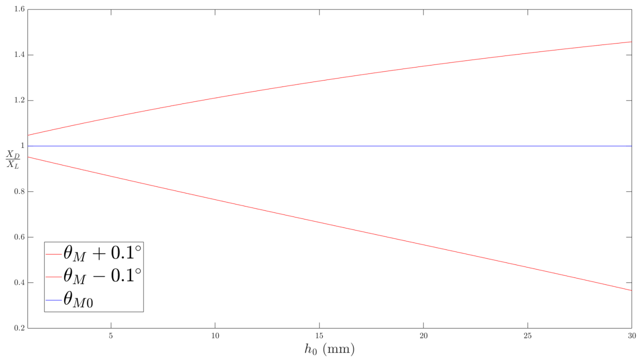

Figure 40: Plot of differential between laser position and detector position due to misalignment of the mirrors

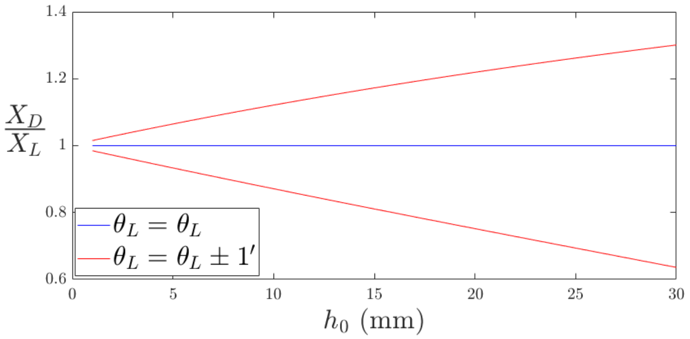

Figure 41: Differential between laser and detector position due to error in laser angle

6 Measuring the interface height

6.1 Samples

In the experiments of this project, three samples have been provided courtesy of Norwegian Crystals AS who produce mono-Si for solar cells using the Czochralski-method.
These three samples are of incomplete boules where a process anomaly has caused the crystal to separate from the melt during the body-stage of the pulling process. This abrupt termination of the pulling process causes the interface to begin cooling immediately after separation, which in term solidifies the interface. This makes the bottom of these ”body-pops” an effective snapshot of what the interface looks like during the body-stage, making them ideal analogues for lab testing.

6.1.1 Sample 1

Sample 1, shown in Fig.42, is a solid crystal section of diameter 213mm aborted at a body length of approximately 276mm and weight 23.65kg. The process was aborted due to the loss of the mono-crystalline structure, possibly due to either excessive pull speeds, insufficient cooling, contaminants in the melt or a combination of the three. The loss of structure is evident by the absence of the vertical nodes up to 44mm above the separation plane, as shown in Fig.43.

The bottom surface of Sample 1, which is the solidified crystal-melt interface,

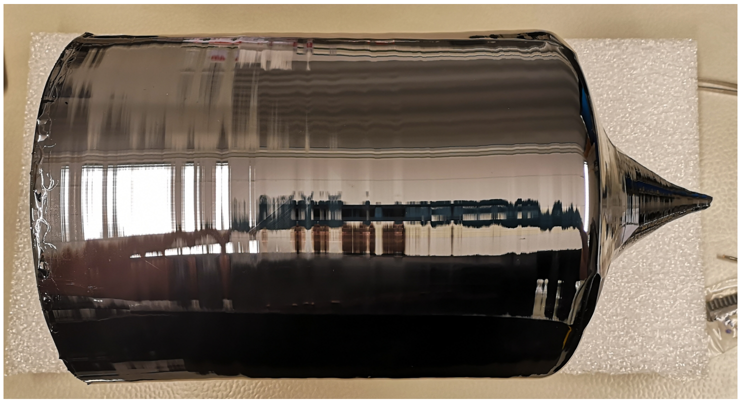

Figure 42: Lateral photo of Sample 1

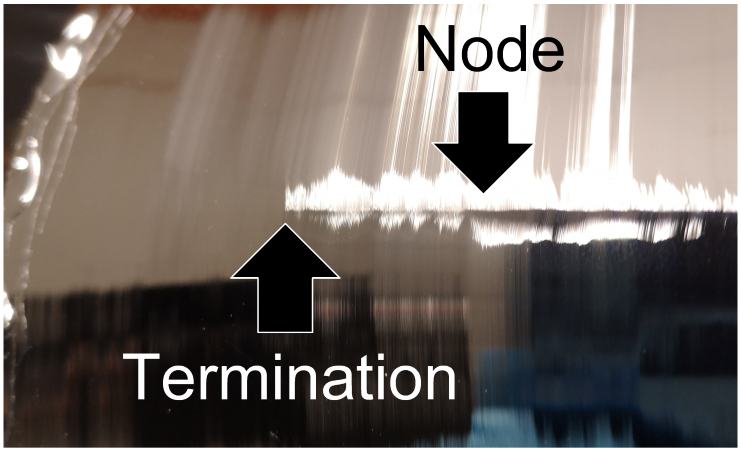

Figure 43: Close-up of Sample 1, showing the node termination point

is shown in Fig.44 and was measured to have a peak deflection of approximately 19.66±0.002mm at its center. The abnormally high interface deflection indicates that the structure loss is likely due to unfavourable thermal conditions, the exact kind the measurement system proposed in this project aims to be able to detect in-situ.

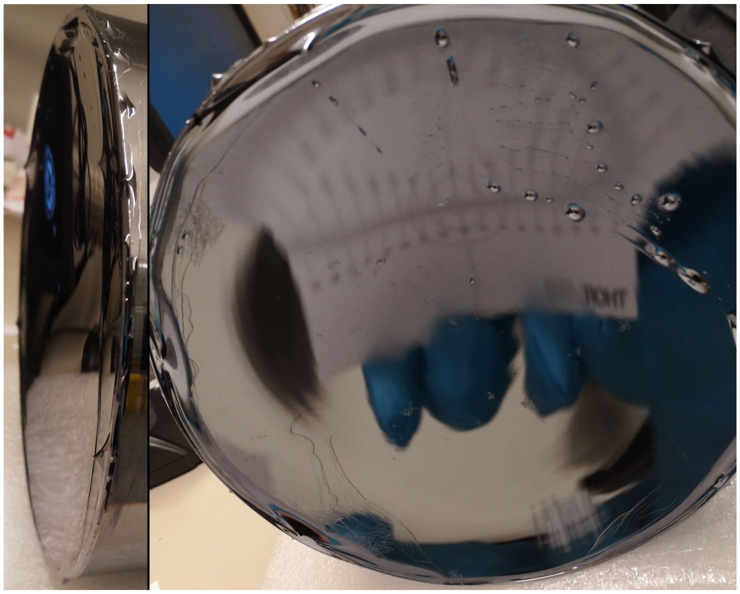

Figure 44: Close up of Sample 1 interface, as seen from the edge (left) and center (right) with a ThorLabs allignment card to demonstrate the parabolic shape

6.1.2 Sample 2

Sample 2, as depicted in Fig.45, is another crystal section of diameter 211mm of approximate body length 162mm and weight 10.07kg. As evident by the discolouration, this sample was aborted due to an unexpected power loss during production and not a loss of structure, as is seen by the nodes remaining intact all the way to the separation plane.

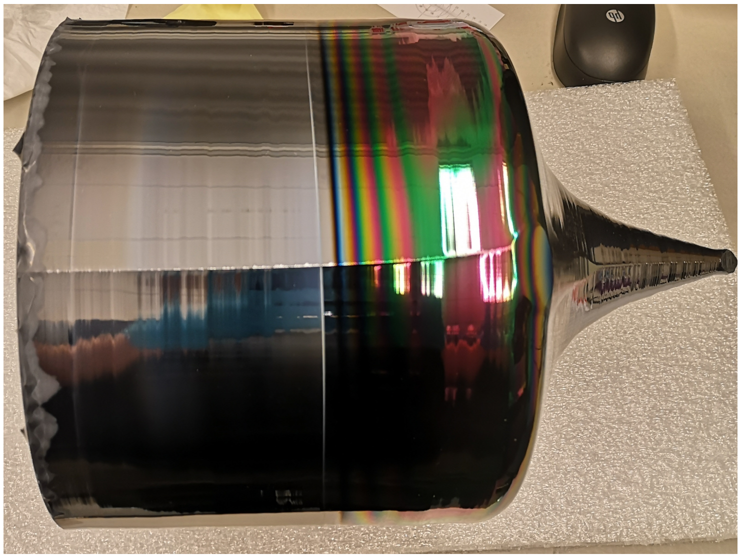

Figure 45: Lateral photo of Sample 2

While the crystalline structure is expected to be largely intact near the interface, unlike Sample 1, it is expected that there are some localized dislocations near the interface due to the separation shock affecting the adjacent solidified material. This unstable section of the crystal would, at the time, have had a very high temperature, making the net energy required to break the covalent bonds relatively weak and vulnerable to dislocations. Also note the two distinct regions of discolouration, with the topmost commonly being due to interruptions in the gas flow which causes airborne particles to collect on the surface resulting in an iridescent ”rainbow” discolouration. While subtle, the lower region has a slight matte white discolouration compared to Sample 1. This is a common indicator of the crystal being exposed to Oxygen in a high temperature environment.

Figure 46: Close up photo of Sample 2 interface

The peak deflection of the bottom surface was measured to $10.96 \pm 0.02 mm$ at its center and as can be seen in Fig.46, the interface is not as perfect as that of Sample 1. This is likely due to a more gradual cooling of the interface and surrounding melt prior to the pop, but can also be an indication of contamination due to interruptions in the gas flow.

6.1.3 Sample 3

Sample 3, as shown in Fig.47, is another 212mm diameter crystal section which was terminated by a power interruption, like Sample 2. This sample has an approximate body length of 389mm and weighs in excess of 34kg.

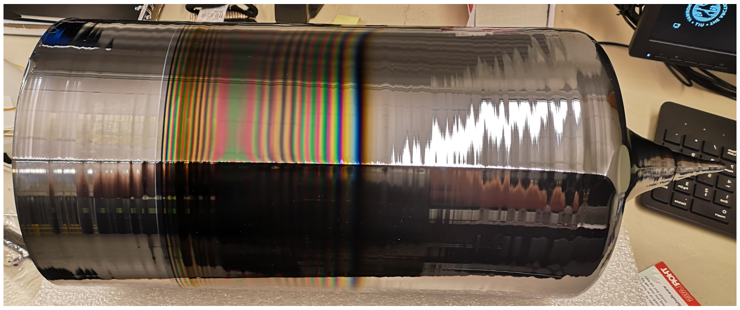

Figure 47: Lateral photo of Sample 3

As can be seen in Fig.47, Sample 3 exhibits the same kinds of discolourations as Sample 2 (Fig.45) which can be more clearly seen as Sample 3 also has a ”clean” section before the iridescent discolouration. Because Sample 3 has three distinct regions and a large volume of presumed ”good” material, it serves as a good candidate for observing the transmittance through bulk material.

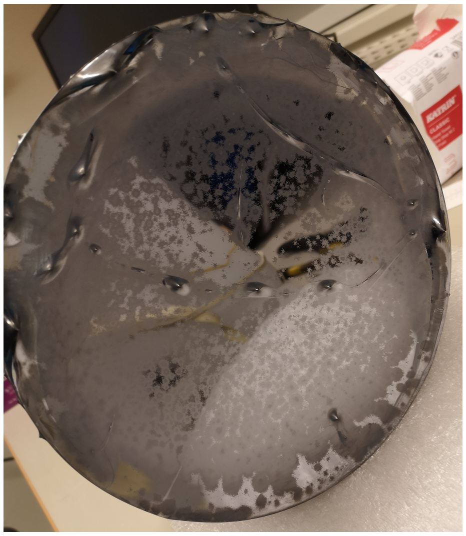

Figure 48: Close up photo of Sample 3 interface

The interface of Sample 3, as shown in Fig.48, was measured to have a maximum deflection of $13.76 \pm 0.02mm$ at its center and can be seen to have the same ”mouldy” imperfections as that of Sample 2.

6.2 Setup

6.2.1 Equipment list

Laser

The laser used is a 2550nm DFB TEC-cooled laser diode from NanoPlus (See Appendix A for datasheet) mounted in a TO5 cubic heat sink. The laser is driven by a ThorLabs LDC8005 LD current control module and the TEC-element by a ThorLabs TED8040 TEC controller, both mounted in a PRO800 benchtop system. During the interface reflection experiment an oscilloscope serving as a function generator(Keysight InfiniiVision DSO-X 2002A) was added as a function generator to provide a modulation signal to the LDC8005.

Detector

The detector used is a PDA10D2 from ThorLabs which is a fixed gain amplified detector using an extended range InGaAs photodiode. Data from the detector is output to a National Instruments USB-6009 DAQ and read as a differential voltage.

Mechanical devices

For this project, four mechanical stages are used:

- Standa 7T175-100 Manual translation stage for holding and moving the samples
- Standa 8MT175-50 Motorized translation stage for moving the laser
- Standa 8R151-30 Motorized rotation stage for rotating the laser
- Standa 8MT50-150BS1 Motorized translation stage for moving the detector
- ThorLabs XRR1 manual rotation stage for setting detector angle

The motorized stages are controlled using a 8SMC5-USB-B9-2 and a 8SMC5-USB in series to provide 3-axis control.

Optical Components

- LA5315-D 1/2” CaF_2 Plano-Convex lens, focal length 20mm
- LJ5386RM-D 1/2” CaF_2 Cylindrical lens, focal length 20mm

- LPNIRA050-MP2 12.5mm Linear polarizer
- WPLH05M-2500 1/2” Half-Wave plate

Software

All control and data acquisition is performed using Python (3.8.6 x64) with the pyximc library to interface with the 8SMC5 controllers and the nidaqmx library for data acquisition from the NI DAQ device. See Appendix C for scripts.

6.2.2 Configuration

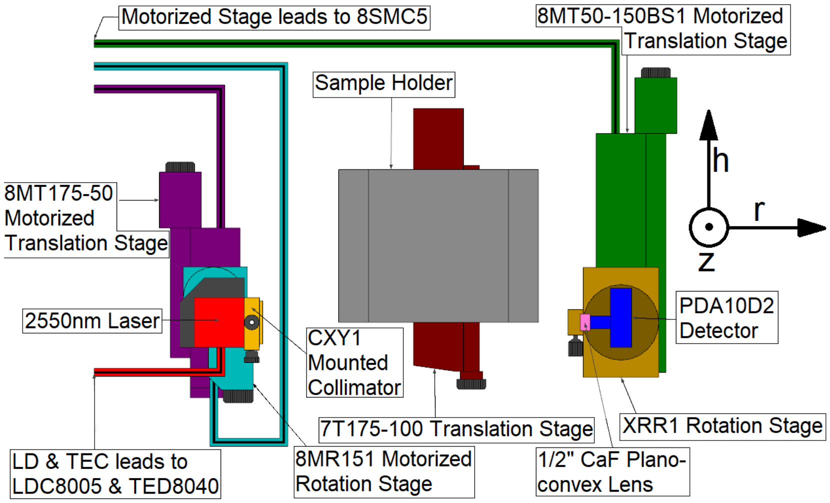

Figure 49: Schematic of experimental setup

A schematic of the setup is depicted in Fig.49 utilizing the components listed in Sec.6.2.1. Various mounting plates and posts, not listed in the equipment list were also used. The sample holder assembly, shown in grey in Fig.49, was purpose-built to fit the samples and handle the weight of Sample 3.

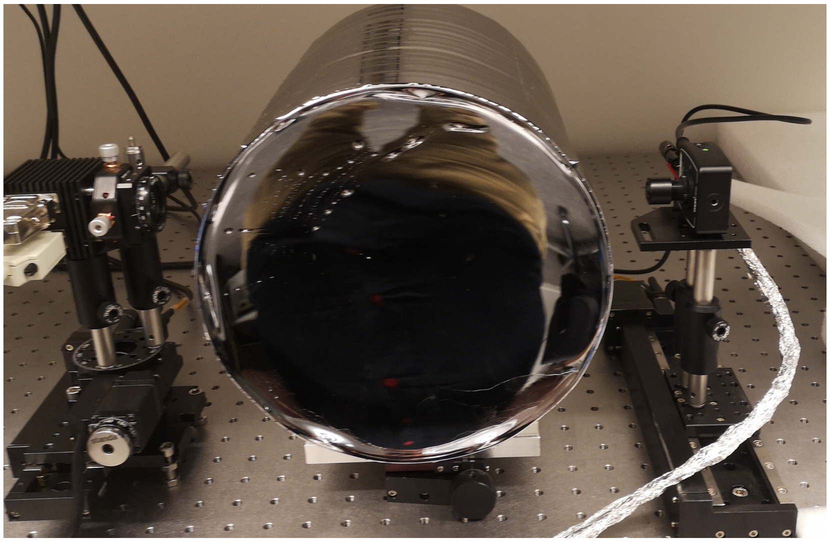

Figure 50: Image of setup during transmission scan of Sample 1. Note the absence of the XRR1 rotation stage on the detector and the presence of the WPLH05M-2500 half-wave plate on the laser

6.3 Signal Capture

6.3.1 Detector Response

The PDA10D2 detector used in these experiments is based on an extended range InGaAs photodiode with a responsivity of 0.92 A/W for a wavelength of 2550nm(See Appendix B). Considering the NI DAQ has an input impedance of $144k\Omega$, the transimpedance gain and resistance scaling factor is then $10V/mA$ and ≥ 0.999, giving a voltage response of $9.197V/mW$ read at the DAQ.
As depicted in Fig.49, the detector also include a mounted lens at the end of a 1/2" closed lens tube. The purpose of this is to extend the effective sensing area of the detector. Given that the detector photodiode is circular with a radius of $r_D = 0.5mm$, the effective sensor area was expanded using the LA5315-D plano-convex lens. Assuming that the paraxial approximation is valid, this gives the condition for ray capture:

$$-r_D \leq \left(1 - \frac{l}{f}\right) x + l\theta_i \leq r_D$$

Setting the distance l between the lens and photodiode to the focal length of 20mm then, assuming that the photodiode is insensitive to incident angle, the beam can be captured as long as the angle of incidence to the lens is:

$$l = f \Rightarrow \left(1 - \frac{l}{f}\right) = 0 \Rightarrow |l\theta_i| \leq r_D \Rightarrow |\theta_i| \leq \left[\frac{r_D = 0.5}{f = 20} rad \approx 1.432\right]$$

This can be seen in Fig.51 which depicts the measured detector response during an open-air calibration run.

Alignment of the system was achieved using a calibration sequence(See Appendix C), which moved the detector(RunSweep.py) to find the optimal relative position and then changed the incident angle(ChangeAspect.py) to find the optimal angle. The sequence was then repeated until both angle and relative position converged. After alignment, the detector was found to become saturated(10V output) for an LD current of 57.44mA, corresponding to a laser output of 2.1mW. Given the determined responsivity of 9.197V/mW and a peak-to-baseline difference of 9.87V, this gives a received signal strength of 1.073mW. The open-air transmittance is thus approximately 51.1%. This may be due the distance between the lens and photodiode not being exactly 20mm, which would cause the much larger beam(3mm diameter) to only partially hit the detector active area.

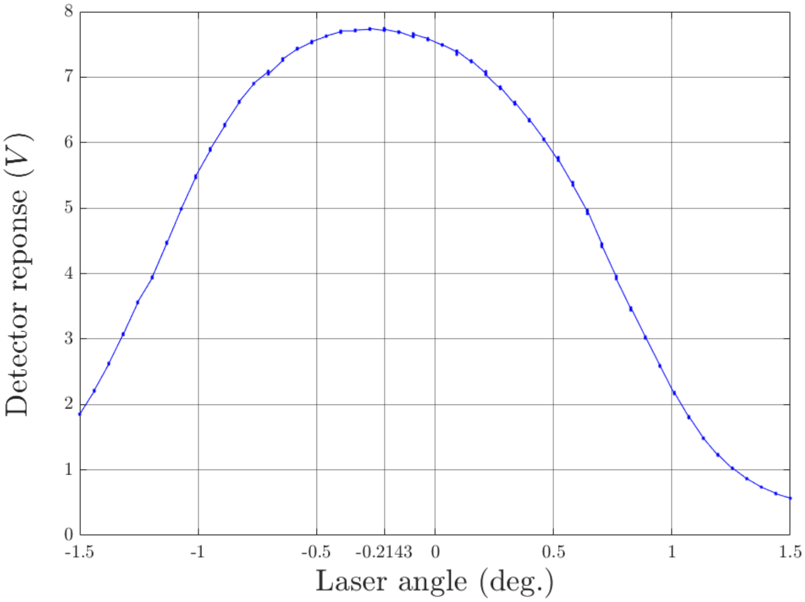

Figure 51: Plot of detector output over changing angle of incidence

6.3.2 Detector Noise

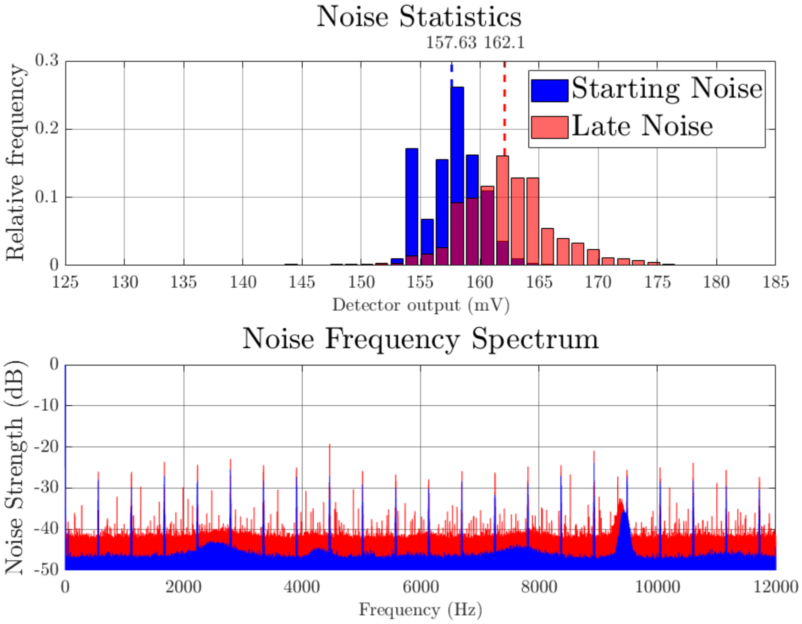

Figure 52: Distribution and frequency spectrum of received noise

The noise signal shown in Fig.52 was recorded under nominal conditions with the detector aperture completely covered. The captured signal is then purely noise from the photodiode, amplifier and DAQ. As can be seen in Fig.52, the noise signal typically has a DC-component of around 160mV and has a distribution with a longer tail towards the lower end with a maximum and standard deviation of 63.90mV and 4.991mV, respectively.
Considering that the specifications for the PDA10D2 detector states an output offset between 75mV and 375mV with a noise RMS of 2.5mV, this noise is not atypical. Factoring in the stated typical absolute accuracy of the DAQ being 7.73mV, we can expect to see regular read errors in excess of 11mV with deviations exceeding 40mV.

It is also worth noting that both the DC offset and the severity of the noise about this appears to increase as the detector remains active for long periods of time as the ”Starting Noise” readings were taken within the first 15 minutes of power-on while the ”Late Noise” was taken after approximately 1 hour.

Overall, this means that the noise presents a significant challenge in regards to getting good readings for the critical areas surrounding the interface, where the signal is expected to be quite weak.

6.4 Signal Processing

As was made clear in Sec.6.3.2, methods to mitigate the noise must be implemented to obtain valid measurements of both transmittance and to detect the presence of a weak signal.
The simplest post-processing method to eliminate the noise signal is then to apply a moving mean function to the data, effectively constricting the bandwidth of the data to the low-frequency range.

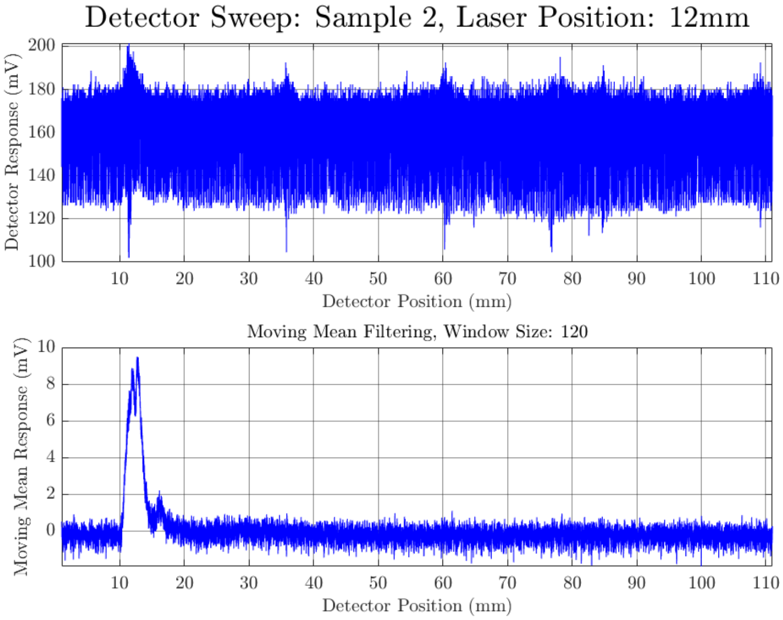

Figure 53: Raw signal and moving mean response for a detector sweep of sample 2 at a laser height of 12mm

Fig.53 shows the results of a detector sweep of sample 2 for a laser position of 12mm.
This was performed by aligning the laser to insert the beam at a height of 12mm relative to separation plane(approximately 1mm above the interface peak) at a normal angle of incidence. The detector was then initially placed at -10mm relative to the separation plane and then moved to 100mm at a rate of 2mm/s while continuous measurements were taken by the DAQ.

As can be seen, the response can be considered adequate, with a SNR of 6.9dB and a clear peak at approximately 12.7mm, meaning an offset of 0.7mm from the laser position.
However, as the response is still relatively weak and will only get weaker as the

source signal becomes weaker, this may not be sufficient for the expectedly low signal strength resulting from poor beam captures during the reflection scan.
For this, a 50Hz square wave modulation signal is provided to the LDC8005 driver and an appropriate matched filter is applied to the received signal. The discrete time matched filter($\mathbf{h}_I$) for a signal $\mathbf{s}$ that maximizes the SNR is generally defined as:

$$\mathbf{h}_I = \frac{1}{\sqrt{\mathbf{s}^H {\mathbf{R}_n}^{-1} \mathbf{s}}} {\mathbf{R}_n}^{-1} \mathbf{s}, \tag{45}$$

where $\mathbf{R}_n$ denotes the covariance matrix of the noise and $\mathbf{s}^H$ denotes the conjugate transpose of the expected signal $\mathbf{s}$.
Though, assuming that the noise is purely stochastic then the elements of $\mathbf{R}_n$ would approach zero and thus $\mathbf{h}_I$ can be approximated as the complex conjugate of the signal template and can be applied as:

$$\mathbf{y}[n] = \sum_k \mathbf{h}_I [n-k] \, \mathbf{x}[k] \tag{46}$$

Since the source signal is the 50Hz square wave that modulates the laser, this can be achieved by simply convolving the received signal with the same square wave 1/2 cycle out of phase.

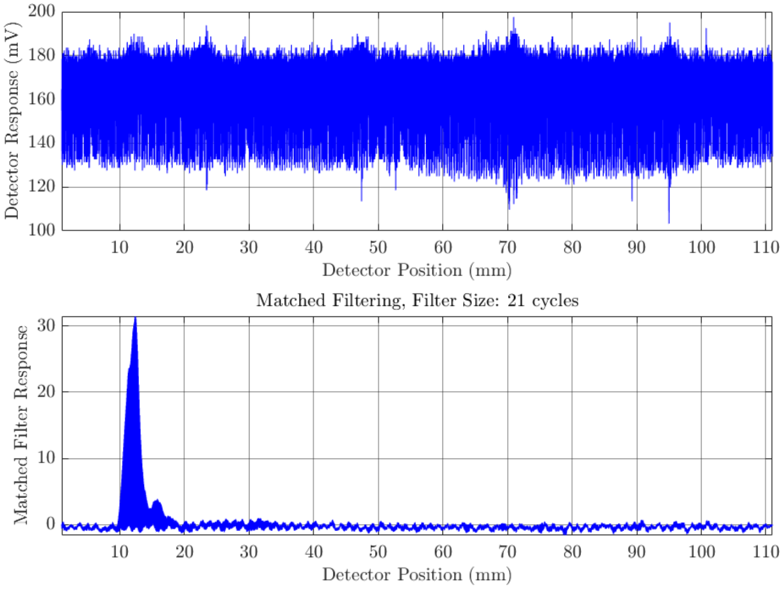

Figure 54: Raw signal and matched filter response for the same sweep as in Fig.53, with a 50Hz square wave modulation of the laser

While the signal peak is not as apparent in the raw signal of Fig.54 as in Fig.53, the filter response shows a very clear signal with a peak at 12.3mm and an improved SNR of 12.8dB.

Conclusion

The matched filtering response proved to have an SNR of 12.8dB compared to the 6.9dB of the moving mean filter, meaning that the matched filter returned a usable signal 3.89 times stronger than the moving mean. This means that the matched filter is vastly superior to the moving mean filter when it comes to sensitivity and precision.

However, to take full advantage of the matched filtering, at least 17 cycles of the filter must be applied to produce reliably good results. In the implementation using the convolve function of the numpy module, this then means that the filtering of large datasets takes significantly longer than the moving mean filter. This means that the moving mean filter is superior when it comes to speed, which is a considerable factor when it comes to large scans.

The superior speed and handling of large measurements of the moving mean filter makes it well suited for the transmittance scan, where the signal is expected to be relatively strong and many large measurements are taken.
The superior sensitivity and precision of the matched filter makes it well suited for the reflection scan, where the received signal is expected to be weak due to poor captures(as will be discussed in Sec.6.6).

6.5 Transmittance scan

6.5.1 Hypothesis

As mentioned in Sec.5.1, it is expected that the beam will travel along a direct path through the bulk crystal, both entering and exiting the crystal approximately normal to the sample walls and strongly deviate if it reflects off the interface.

This means that if the laser height is greater than the interface peak height then it is expected that the transmitted beam can be captured by the detector at a height approximately equal to that of the laser. However, as also mentioned in Sec.5.1, a challenge is the fact that the surface of the crystal is not perfectly flat, but rather "layered" appearance as can be seen from images of the samples. This then means that while the laser and detector may be aligned to the normal of the crystals center axis, the angle between the laser beam and the wall at both entry and exit points may not be. This then means that a difference between the entry and exit height may occur due to the refraction from the varying surface angles.

The exact maximum deviation of the surface angle is not currently known as an appropriate measuring device was not available, but since these the deviations were too small to be measured using a calliper and the overall texture is very smooth to the touch it can be assumed that these angles are relatively small. Under the overarching assumption that the laser and detector are perfectly aligned and that the maximum slope of the walls does not exceed $\pm 2.000°$ then the maximum discrepancy between entry and exit height for a 210mm crystal can be found to be $\pm 5.200mm$ assuming a refractive index of $n(2.55\mu m) = 3.439 \pm 0.0516$[34][35][36][37]. Assuming the same conditions at the exit-point then the maximum angle of incidence to the local surface of $\pm 3.419°$ resulting in a refracted beam of angle $\pm 9.833°$ relative to the center axis normal. With a median distance from the wall to the detector of approximately 42mm, this adds an additional deviation of $7.280mm$ meaning that the transmitted beam can be found as far as $12.480mm$ away from the laser height in the extremes.

As discussed in Sec.2.4.2, the wavelength of 2550nm is well within region B where the intrinsic absorption(band-to-band) cannot occur and thus the only absorption is that caused by free carriers and multi-photon interactions. As the laser is relatively weak, outputting 6.4mW at the max LD current of 100mA with a beam diameter of 3mm resulting in an output intensity of $905.4W/m^2$, the expected two-photon absorption is expected to be negligibly weak[39]. Thus, the primary source of absorption should be the free carrier absorption, which according to the model described in Secs.2.4.5 and 2.4.7 should be $0.0659 \leq \alpha\left(2.55\mu m\right) \leq 0.1272$ and $0.1414 \leq \alpha_S\left(2.55\mu m\right) \leq 0.2731$ according to the findings of Schroder[31].

Given the detector sensitivity, refractive index of Silicon and open air transmittance, the received signal should then be:

$$V = P_{LD} \cdot \exp\left(-\alpha \cdot D_C\right) \cdot \left(1 - R\right)^2 \cdot T_0 \cdot VR_{Det} \tag{47}$$

Which, for an LD current of 100mA and assuming the model of this work holds then the expected detector response should be between 3.67V and 1.01V, or 0.752V and 47.3mV using Schroder's model.

6.5.2 Procedure

The experimental procedure is as follows:

- Adjust height of detector and laser to the same as the height of the crystal center
- Run recalibration sequence through open air to ensure alignment
- Calibrate crystal height, setting zero as the point where detector output stabilizes at 5V for 100mA(6.4mW) laser output
- Initiate scan sequence for a specified laser heights, normally every mm over the range of the laser stage(0-50mm)
- For each laser position, scan detector over -10mm to 100mm relative calibrated laser zero-position

6.5.3 Results

Sample 1

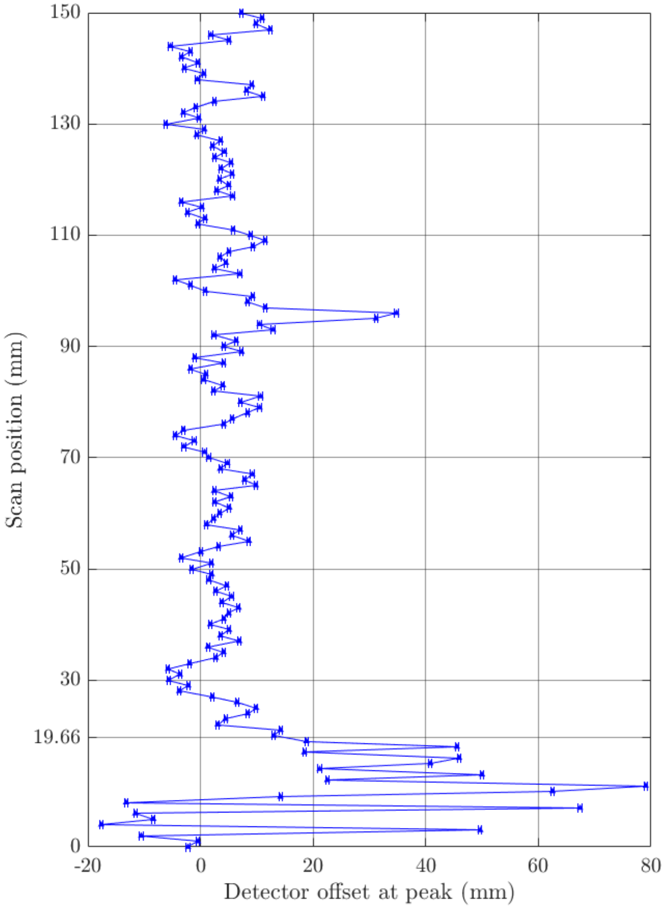

Figure 55: Position of detector at best capture of transmitted beam relative to laser position for sample 1

The graph in Fig.55 shows the position of the detector relative to the laser when the peak signal is registered, corresponding to the best capture for that detector sweep. For laser positions below the interface height of 19.66mm the beam is expected to at least partially intersect the interface and thus either be deflected upwards, leading to no capture or a weak capture at a high positive offset. As is seen in Fig.55, the expectations are generally met, showing erratic results due conforming to a weak signal(false positives) and possibly weak captures at high offsets. The lowermost results where the offsets are predominantly negative can to a degree also be attributed to false positive with the notable exceptions when the laser height is close to the beam diameter(3mm) such that a portion of the beam ”leaks” below the bottom plane of the sample. In such cases we would expect to receive a relatively strong signal since it travels through open air and we would expect the best capture to occur when the detector is slightly below the sample bottom plane giving a slight negative offset.

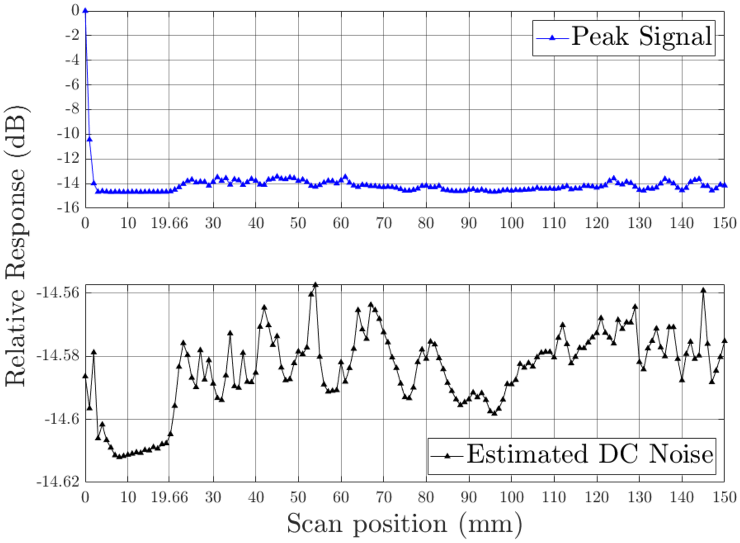

Figure 56: Peak detector response (top) and estimated DC component of noise(bottom) relative to calibration response for sample 1

The top plot in Fig.56 shows the relative magnitude of the detected peaks marked in Fig.55 compared to the calibration response, which was here 5.188V including noise. The mentioned beams partially passing below the sample can be seen at laser positions 1mm and 2mm with relative signal strength -10.4dB and-14.0dB, respectively. From 2mm to approximately the interface height(20mm) we find the mean response to be -14.6dB and -14.2dB for the remaining length up to 150mm.

The bottom plot in Fig.56 showing the estimated DC component of the noise was compared to the same calibration noise and therefore to scale with the peak signal. It assumed that the extremes of the detector sweep (-10mm and 100mm) were sufficiently far from the peak that no signal was present there. It was therefore assumed that every reading within 0.2mm of the extremes ($N = 1200$) was pure noise and the noise DC component was defined as the mean of these samples. As the plot indicates, the DC noise remains largely constant, having a mean of -14.6dB from 2-20mm and -14.6dB from 20-150mm and varies with 0.06dB over the entire range.

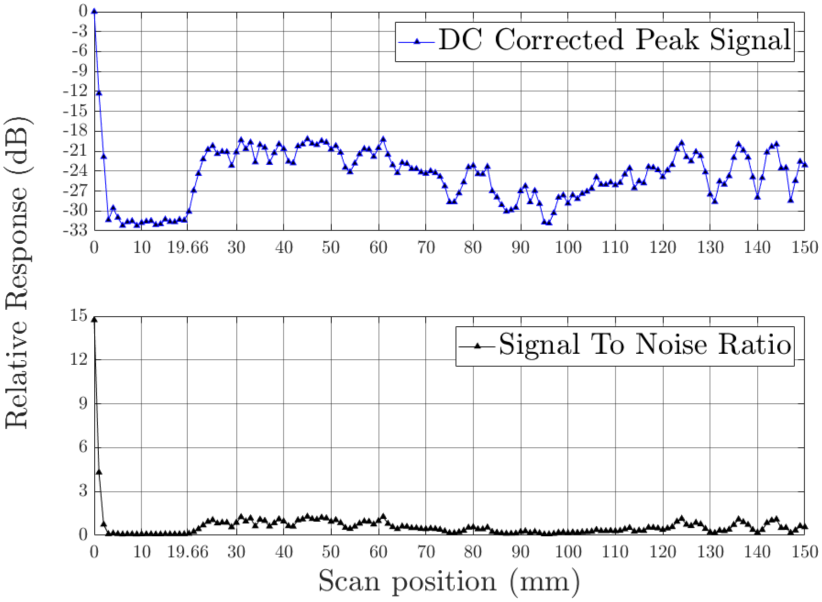

Figure 57: Peak response relative to DC noise (top) and estimated SNR compared to DC noise(bottom) relative to calibration response for sample 1

The plots in Fig.57 are then the comparison of the two plots of Fig.56, with the top plot being the difference between the peak signal and the baseline created by the noise DC and the bottom being the ratio of raw signal versus noise DC. As the top plot of Fig.57 shows, the mean strength of the corrected signal from 2-20mm is -31.0dB before rising to -20.8dB at 24mm with a mean strength of -24.0dB from 20-150mm. The SNR plot then shows a mean ratio of 0.13dB for scan positions in the range 2-20mm and 0.57dB for 20-150mm.

Sample 2

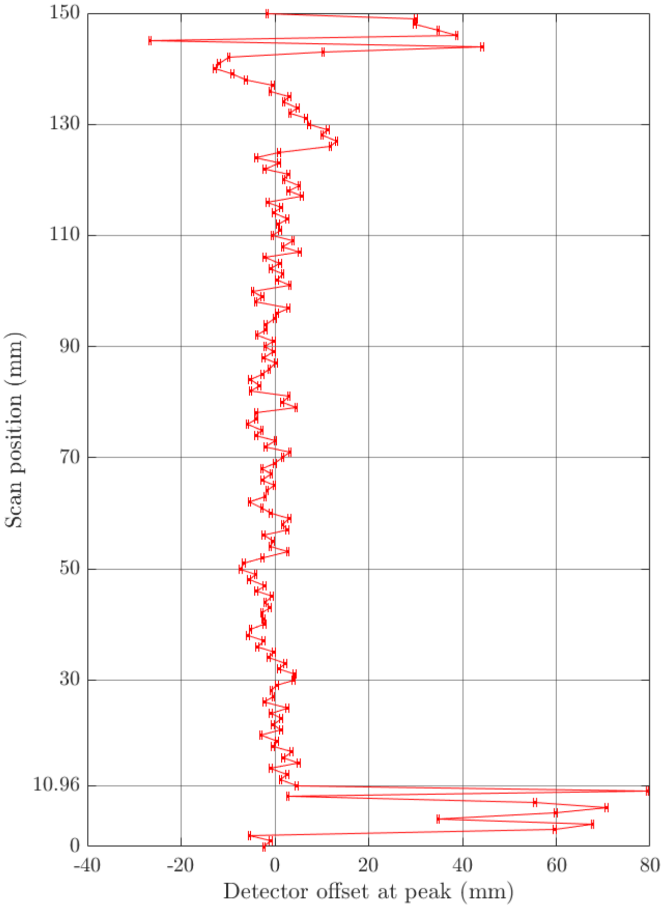

Figure 58: Position of detector at best capture of transmitted beam relative to laser position for sample 2

As can be seen in Fig.58, the same behaviour as was seen in Fig.55 is also present for the peak offsets for sample 2. The offsets in the scan range of 0-2mm are all weakly negative, conforming to the beam "leaking" below the sample, while the remaining 3-10mm shows the same positive and erratic offsets as was seen in Fig.55. It is however worth noting the resurgence of the erratic peak offsets after approximately 140mm after being relatively close to the expected offset of

0, having a mean absolute offset of 3.05mm in the scan range 11-140mm with a maximum deviance of 13.11mm occurring at 127mm.

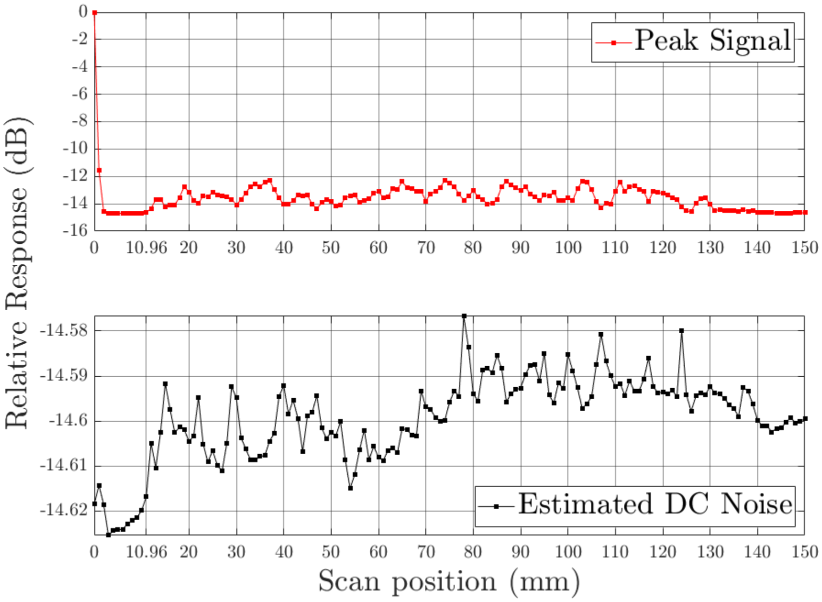

Figure 59: Peak detector response (top) and estimated DC component of noise(bottom) relative to calibration response for sample 2

In Fig.59 we see the same measurement quantities as in Fig.56 and the same general behaviour with the exception of a fading tail as the scan position approaches 150mm. The strength of the peaks from the ”leaking” beams occurring for scan positions 1 and 2mm are -11.6dB and -14.6dB, respectively. For scans below the interface peak (3-11mm) the mean peak strength is -14.7dB followed by -13.5dB up to 140mm and -14.7dB in the range 141-150mm.
The estimated DC noise was estimated in the same way as for Fig.56 and is again, relatively constant with an overall mean of -14.6dB and varies with 0.05dB over the entire range.

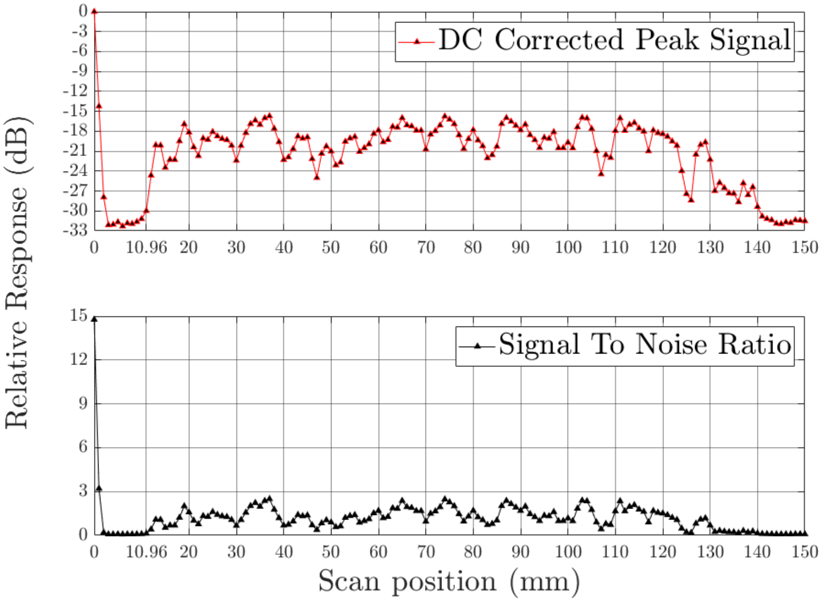

Figure 60: Peak response relative to DC noise (top) and estimated SNR compared to DC noise(bottom) relative to calibration response for sample 2

In the corrected signal peaks shown in the top plot of Fig.60 the mentioned fade-out as the scan height exceeds 140mm becomes more apparent as the signal peak returns to the same level as that below the interface at 10.96mm. The mean corrected strength is then -31.4dB below the interface peak (3-11mm), -31.6dB above the fade-out at 140mm, and -20.3dB in the range 12-139mm between these two with a peak of -15.7dB at 37mm.
In comparison to sample 1, we see that the SNR for sample 2 is significantly higher, having a peak of 2.49dB at 37mm with a mean of 0.1dB for 3-11mm, 1.25dB for 12-140mm, and 0.09dB for 141-150mm.

Sample 3

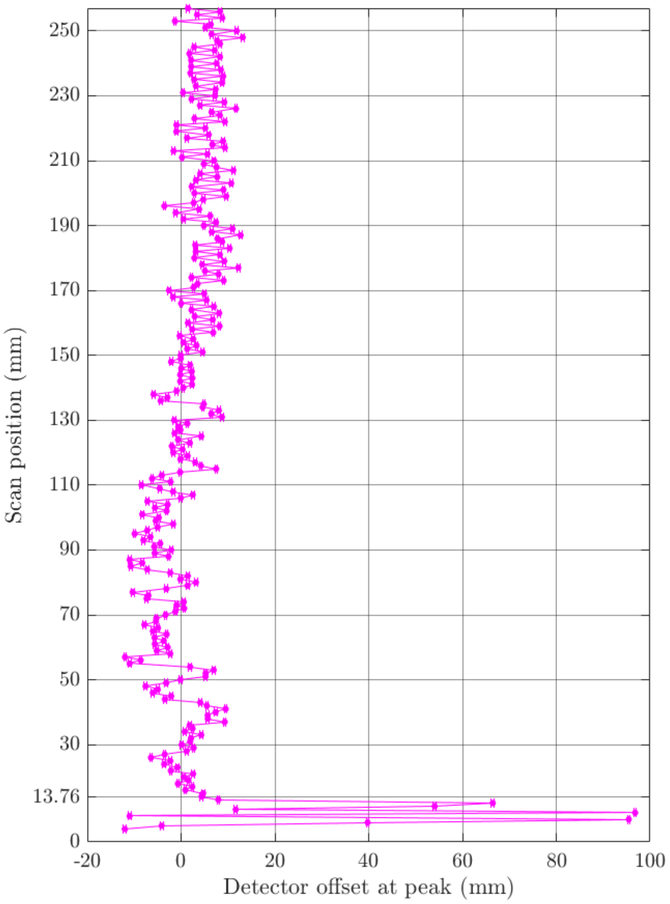

Figure 61: Position of detector at best capture of transmitted beam relative to laser position for sample 3

In the peak offsets shown in Fig.61 we see the same kind of varying peak position below the interface height of 13.76mm as can be seen in Figs.55 and 58 as well as a generally well behaved peaks from there on. It is however worth noting that there appears to be a trend of the offset increasing with the scan height, something which could indicate a misalignment of the sample or a mismatched detector scan speed.

Overall we see a mean absolute deviation of 4.58mm with a maximum of 13.13mm at 248mm.

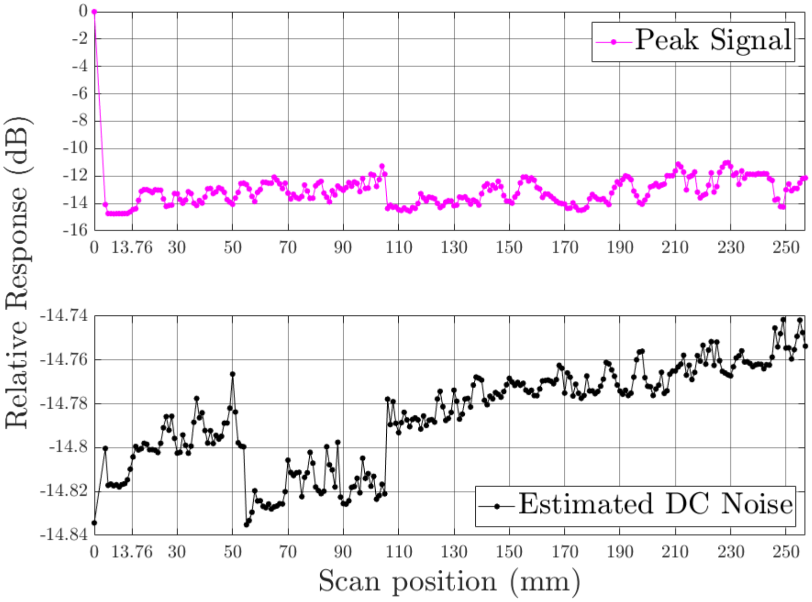

Figure 62: Peak detector response (top) and estimated DC component of noise(bottom) relative to calibration response for sample 3

From the top plot of Fig.62 it is apparent that the signal is generally stronger than for samples 1 and 2, having a mean of -14.7dB below the interface(up to 14mm) and -13.1dB for the remaining 243mm, giving a difference of 1.6dB compared to 1.2dB and 0.5dB for samples 2 and 1, respectively.

The overall noise DC signal strength is here -14.6dB with a maximum peak-to-peak deviation of 0.1dB and has a notable deviation from 55-105mm where the mean is -14.7dB.

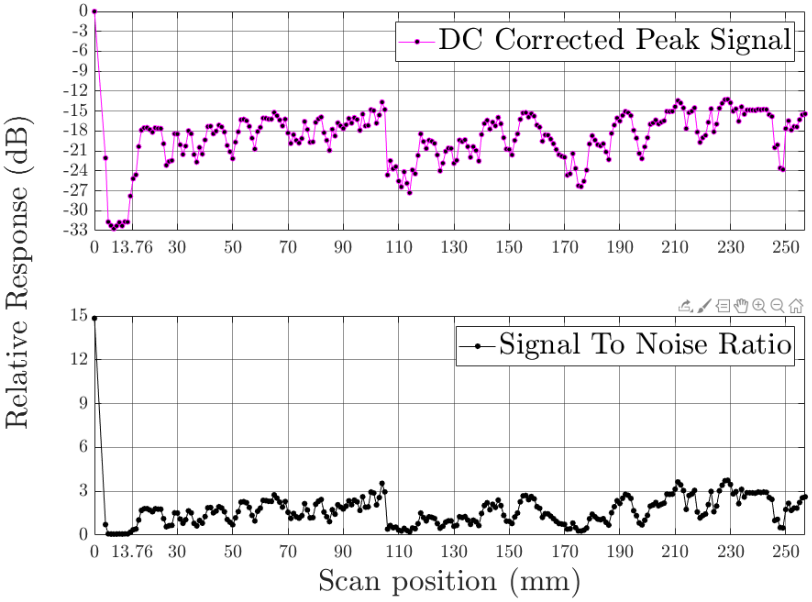

Figure 63: Peak response relative to DC noise (top) and estimated SNR compared to DC noise(bottom) relative to calibration response for sample 3

After correction for the DC noise we can see that the peak signal, as shown in the top plot of Fig.62, is significantly stronger than that of samples 1 and 2 shown in Figs.56 and 59. The mean strength of the signal below the interface is -32.0dB, comparable to the -31,0dB of sample 1 and -31.4dB of sample 2, but for positions above 14mm the mean is here -18.6dB with a maximum -13.3dB at 219mm.

Likewise, the SNR is also significantly better with an overall mean of 1.6dB with a peak of 3.8dB at 229mm and a mean of 0.1dB below the interface peak.

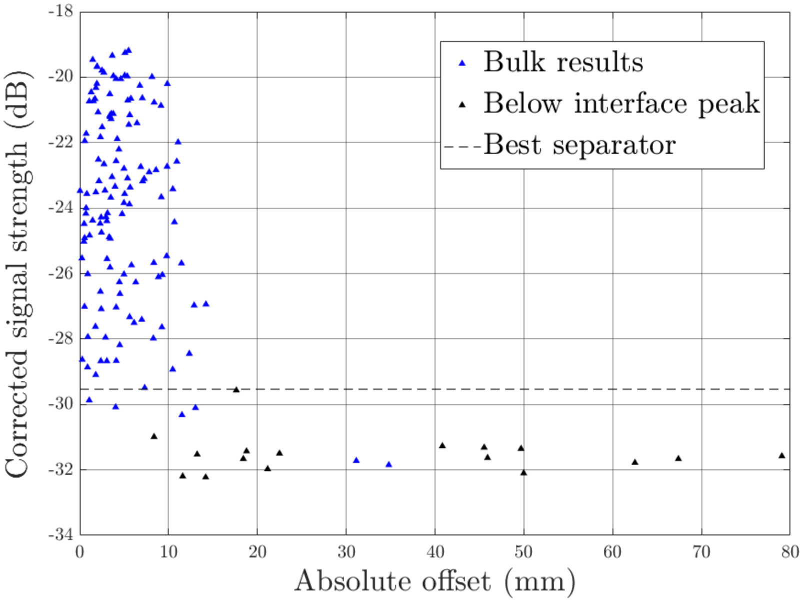

Figure 64: Plot of absolute offset of captured beam vs. corrected signal for sample 1

In Fig.64, the grouping of the bulk results(through cylindrical parts of the crystal) are compared to the grouping of the results for scan positions below the interface peak. The best separator, shown in dashed black, was determined as a naive linear classifier of the signal strength set to minimize the product of the classification errors for the results. The classifier was determined as a threshold of -29.5dB and resulted in a 95.4% correct classification of the bulk results and 100% of the below interface results. Applying this classifier to the results shown at the top of Fig.56 returned a lowest positive for the scan at 21mm, meaning that the classifier determined that the interface peak must be between 20mm and 21mm.

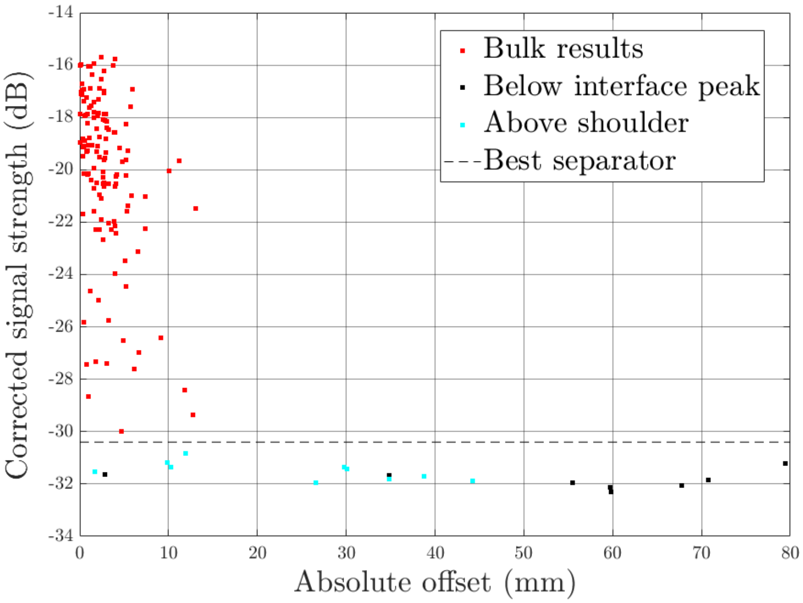

Figure 65: Plot of absolute offset of captured beam vs. corrected signal for sample 2

In Fig.65, the equivalent plot to Fig.65 for sample 1 is shown. As was pointed out previously, the transmittance through sample 2 is generally better up to approximately 140mm. To be fair to the classifier, the results from the shoulder section(above 140mm) were separated from the bulk and considered equivalent to the below interface results. The classifier was then trained in the same manner as for sample 1. The result was a threshold of -30.4dB, resulting in a 100% correct classification of both bulk and zero(below interface and above shoulder) results. Applying the classifier to the results shown in Fig.59 returned a lowest positive for 11mm, meaning a maximum peak between 10mm and 11mm.

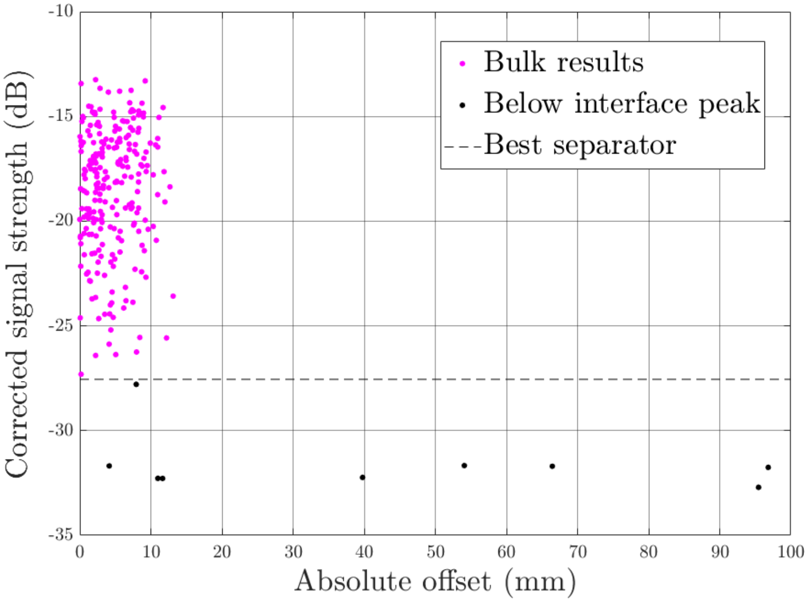

Figure 66: Plot of absolute offset of captured beam vs. corrected signal for sample 3

In Fig.66, the absolute offset versus corrected signal strength is shown. Since the source dataset for this contains the most measurements, this dataset may be considered a better picture of the statistics of the measurements. Training a classifier for this yielded a threshold of -27.6dB, resulting in a 100% correct classification of the results. Applying the classifier to the results shown in Fig.62 returned 14mm as the lowest positive, meaning a detected maximum peak between 13mm and 14mm.

6.6 Interface reflection

6.6.1 Hypothesis

As with the transmittance scan, the expected absorption coefficient is in the range of 0.0659 to 0.2731. Given that the standard angle is 15° relative to the crystal axis normal, the refracted beam should have an angle of 4.32° assuming $n = 3.439$. Assuming a crystal diameter of 210mm and a perfect hit on the flat of the interface peak then the entry and exit points should be approximately 7.92mm above the interface peak. Under the assumption of symmetry this results in a total path length of 210.60mm. Compared to the expectations for the transmittance for the transmittance scan, the additional 0.60mm in the path length (assuming absorption is isotropic) would then result in a maximum additional loss of 1.63°(-0.07dB). Furthermore, an internal angle of 4.32°

make contact with the flat of the interface peak having an incidence angle of approximately 85.7° which is far beyond the critical angle of 16.9°, meaning that total internal reflection applies. For the entry and exit points, assuming symmetry (prefect peak hit) then the transmissivity given by the Fresnel equations is approximately 0.686 at the entry and exit points.

Given the expected internal angle of 4.32° the total path length of the beam is negligibly longer(approx. 0.60mm for crystal diameter 210mm) and thus the detector response can be determined as between 3.55V and 0.979V for the model of Sec.2.4.2 or 0.727V and 45.7mV for Schroder's model.

The main challenge in this experiment is the alignment, since the effective detector area is only 12.7mm in diameter and can only accept angles within a 1.43° half angle cone it is extremely difficult to get a good capture. While some good captures were made in the transmittance scan, the added reflection off of the interface introduces both another yaw angle(in the horizontal plane) and a pitch angle (vertical plane) that would interact with the other angles, making the entire system significantly more sensitive to misalignment or deviations in the crystals walls, bulk, or interface. Because of this, it is expected to get very poor captures and thus very weak and brief signals, this is to a degree mitigated by the use of matched filtering in post-processing as this greatly enhances the modulated signal as discussed in Sec.6.4.

6.6.2 Procedure

The procedure for the reflection scan proceeds in a similar sequence as with the transmission scan:

- Adjustment and recalibration like with the transmittance scan
- Aligning the sample separation plane with the zero of translation stages
- Setting angle of the detector to a base angle (commonly 15°)
- The laser is set to an angle in a range of -1° and 1° around the base angle

- For each angle a scan cycle consisting of a set of laser positions is scanned
- For each laser position, the detector sweeps 25mm around the expected position of the output beam
- For each complete angle scan, the scan attempts to narrow the range to locate a cluster of readings consistent with a reflection off of the interface peak

6.6.3 Results

Raw Reference

The raw reference samples were taken by performing simple scans like for the transmission scan only with a set angle for the detector and laser. The purpose of this was to obtain reference data for the deflection and signal change as the laser reflects off of the interface peak.

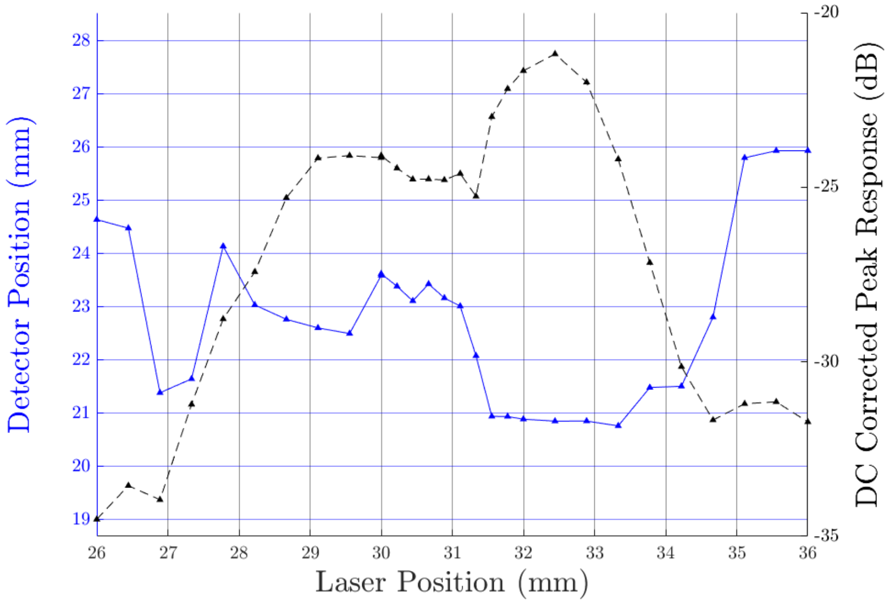

Figure 67: Detector position of at best capture (left axis) and DC corrected peak response(right axis) for sample 2, laser angle: 10°, detector angle: 10°

As seen in Fig.67 showing a sweep with symmetric laser and detector angles of 10°, the signal amplitude follows an "M" shaped curve with a center dip at 31.33mm where the amplitude is -25.3dB and the detector position is 22.08mm. If we then consider the idealized assumptions:

- The crystal walls are perfectly flat and vertical
- The interface peak is perfectly flat and horizontal
- The incident angle of the beam to the detector is normal

Then the beam can be traced forward from the laser and backwards from the detector using Snell's law. Given the approximate distance from the crystal wall to the laser being 84.1mm and from the wall on the other side to the detector being approximately 33.2mm and an assumed refractive index of 3.439 then the intersection should have occurred at a radial position of 1.72mm away from crystal center towards the laser and at a height of 11.03mm relative to the bottom of the sample. Considering the interface peak was measured to be 10.96mm for sample 2, this is a reasonable measurement of the interface peak.

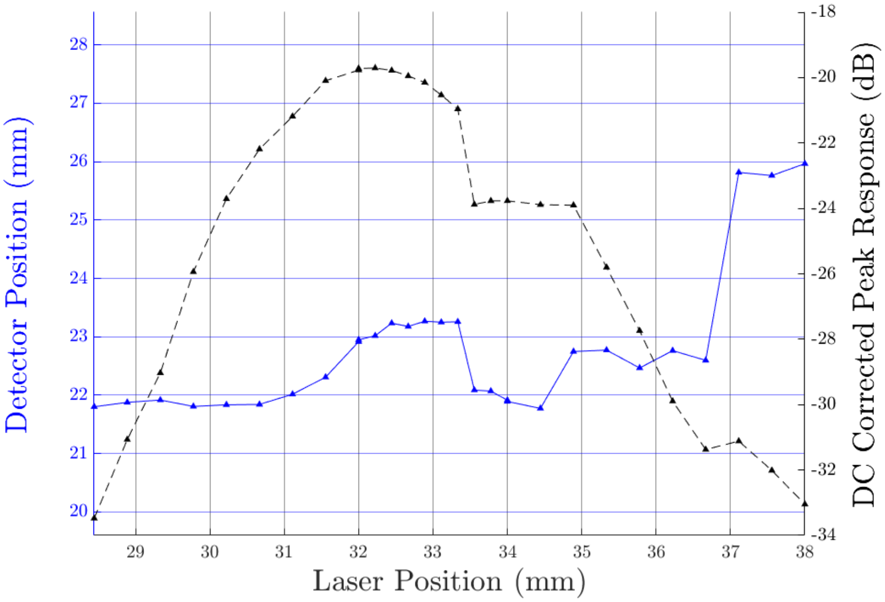

Figure 68: Detector position of at best capture (left axis) and DC corrected peak response(right axis) for sample 2, laser angle: 11°, detector angle: 10°

As can be seen in Fig.68, a similar amplitude curve and detector position is also present for the asymmetrical case with a laser angle of 11° and a detector angle of 10°. Here we see a dip at a laser position of 33.56mm with a signal strength of -23.9dB and a detector position of 22.09mm, using the same methods, this corresponds to the beam being reflected at a radial position of 3.22mm from the interface center and a height of 11.12mm.

Sample 1

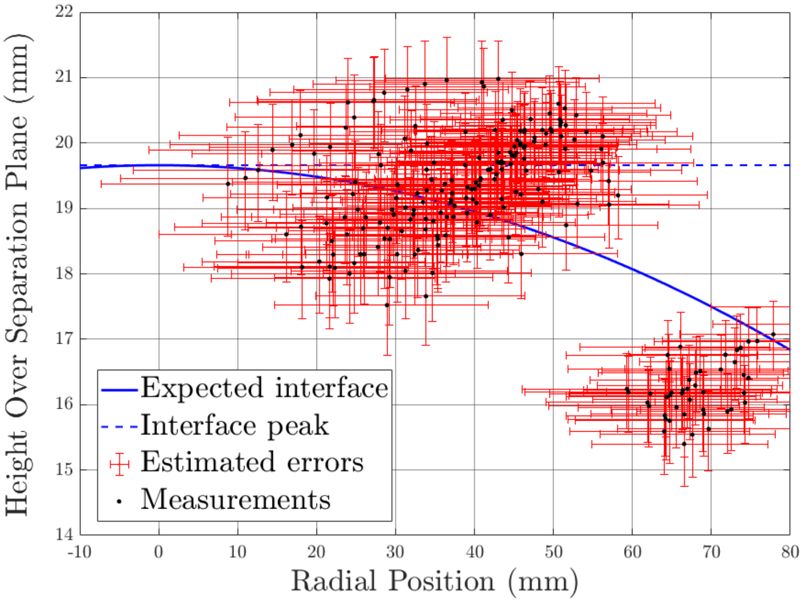

Figure 69: Estimated position and height of beam-interface encounter

The black dots in Fig.69 represent the estimated reflection points for a normal incident angle into the detector while the red errors correspond to the range of possible reflection points for incident angles within the 1.43° half angle cone of the detector lens.

The estimated radial and vertical coordinates of the reflection were determined in the same manner as in Sec.6.6.3 using the known position and angle of the laser and the detector. For this section of the experiment, the laser and detector assemblies were altered to prevent the components from scraping the sample during scanning. The distance from the laser to the crystal wall was reduced to $L_0 = 76$mm and was offset $L_a = 22$mm down the h-axis (parallel to sample center axis) and the detector was moved to a distance of $L_{CD} = 42$mm from the crystal wall. Because of the offset, the reference position of the laser was altered as:

$$L_{LC} = L_0 + L_a \sin\theta_L \quad x_L = x_0 + (1 - \cos\theta_L)\, L_a$$

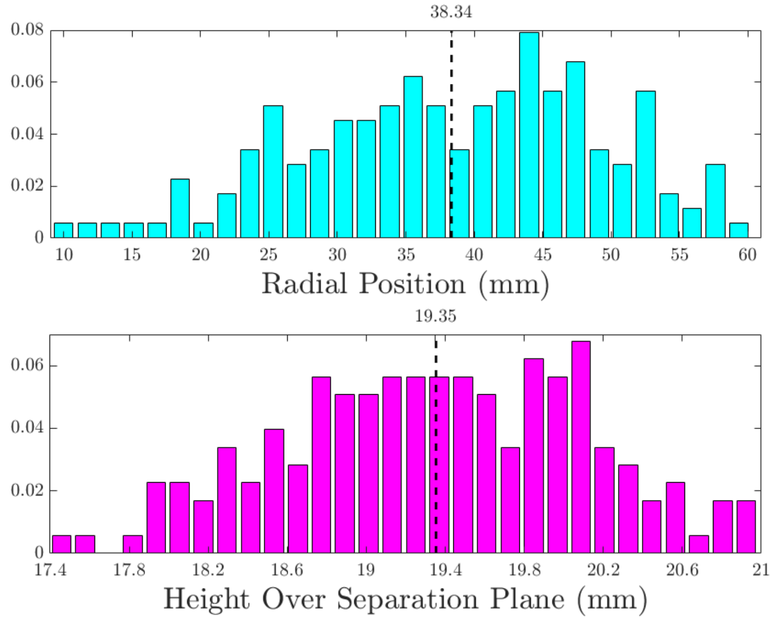

Figure 70: Histogram of estimated radial and vertical coordinates of reflection points for sample 1 with means marked in dashed black

The histograms shown in Fig.70 show the distributions of the coordinates of registered interface reflections for the main cluster shown as the topmost cluster in Fig.69. As is shown in Fig.70, the mean of the radial position is 38.34mm off center towards the detector side, which is a significant error as the expected interface described in Fig.5 will have an angle exceeding 1° for radial positions more than 4.94mm away from the center given the known peak deflection of 19.66mm.

The mean height of the estimated reflection points is shown in Fig.70 to be 19.35mm, corresponding to a 1.58% error compared to the known peak height of 19.66mm.

As mentioned in Sec.6.6.1, it is expected that the addition of the interface reflection will result in the quality of beam captures being very poor, as can be seen in Fig.71.

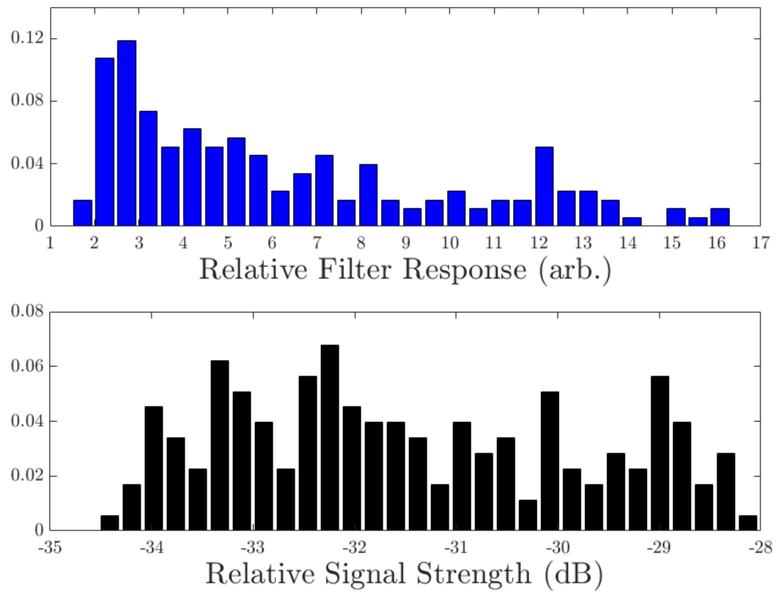

Figure 71: Histogram of matched filter response(top) and signal strength(bottom) for the reflectance scan of sample 1

The mean signal strength of the registered reflections, shown in the bottom plot of Fig.71, was found to be -31.5dB with a peak of -28.1dB. Compared to the results seen in Sec.6.5.3, this is about the same as we would expect to find for significant angle offsets, like what was found below the interface peaks. As the topmost histogram shows, while the signal is weak, there is a notable response from the matched filter, indicating that a signal element modulated to a 50Hz square wave is weak but present. The values of the filter response shown in the histogram are computed as the value of the peak of the raw response relative to the mean of the filter response for each sweep. The resulting mean response was then found to be 6.303 sweep means with a peak of 16.080 means.

Sample 2

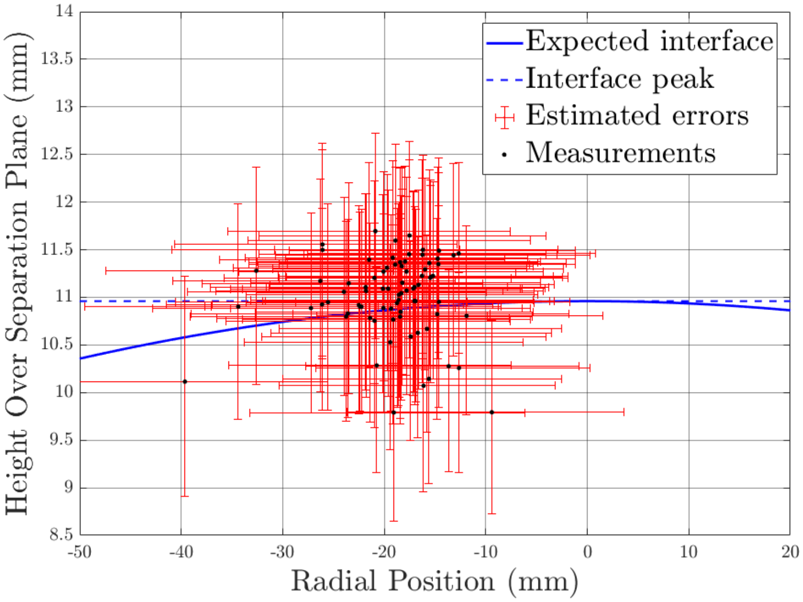

Figure 72: Estimated position and height of beam-interface encounter

The results shown in Fig.72 show the same quantities as that of Fig.69 with the same setup. Compared to the results from Fig.69 we see that there are fewer measurements that register as valid beam captures but that the grouping is tighter and conform better to the expected response at the interface peak.

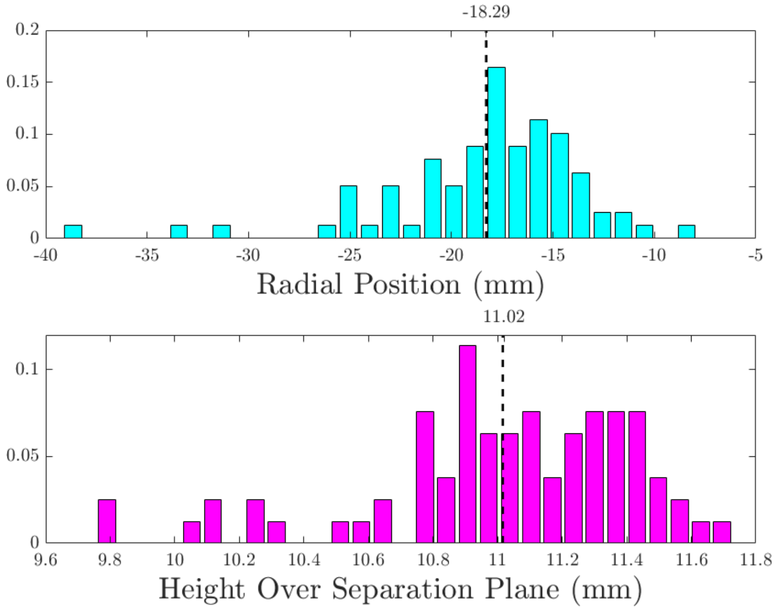

Figure 73: Histogram of estimated radial and vertical coordinates of reflection points for sample 1 with means marked in dashed black

As shown in Fig.73, the spread of both the radial and vertical positions are both smaller than that shown in Fig.70 and show a significanly tighter spread about their respective means. The mean of the radial positions shown in the top histogram of Fig.73 was found to be 18.29mm from the center towards the laser with error bounds reaching both to and above the sample center, providing a good argument for the reflections hitting the interface peak at the sample center.

Looking at the plot of the height over separation plane we can see that the minimum and maximum heights were found to be 9.79mm and 11.70mm, giving a range of less than 1mm. The mean result for the peak deflection was then found to be 11.02mm, deviating 0.06mm from the known deflection of 10.96mm corresponding to an error of 0.51%.

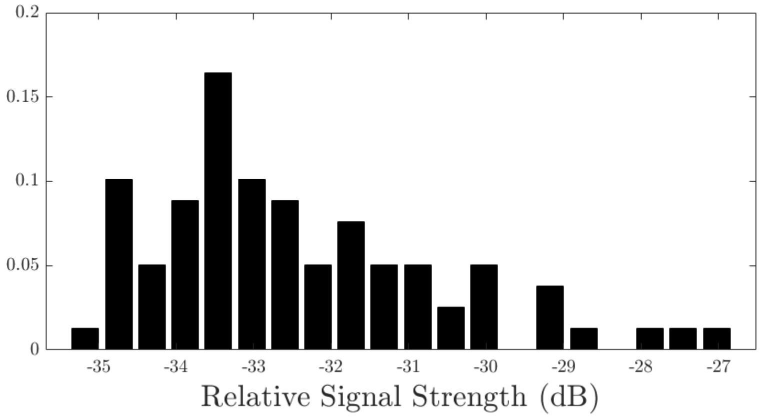

Figure 74: Histogram of received signal strength for sample 2 reflectance scan

As with sample 1, the signal strength is vanishingly small, as is shown in Fig.74 to have an overall mean of -32.4dB and a maximum of -27.0dB.

Sample 3

After several attempted scans, no signals of sufficient strength were received and thus no reflected beams were successfully captured, producing no valid results.

6.6.4 Conclusion

Sample 1

As shown in Fig.70, the mean detected interface peak was determined to be $19.35 \pm 0.79mm$ at a mean radial position of $38.34 \pm 14.41mm$, with 76.6% of captured beams registering as valid reflections with estimated reflection points within the crystals.

Sample 2

The results shown in Fig.73 returned a mean interface peak height of $11.02 \pm 1.21mm$ at a radial position of $-18.29 \pm 14.19mm$. The ratio of valid reflections versus number of captured beams was 34.2%.

7 Analysis of experimental data

7.1 Transmittance scan

7.1.1 Sample 1

As could be seen in the results of the transmittance scan, there is a clear and consistent change in behaviour once the scan passes the peak interface height both in signal and peak location.

Looking at the response curve for sample 1 we can see that the peak detector response was at a height of 45mm and had a peak of 60.37mV as can be seen in Fig.75.

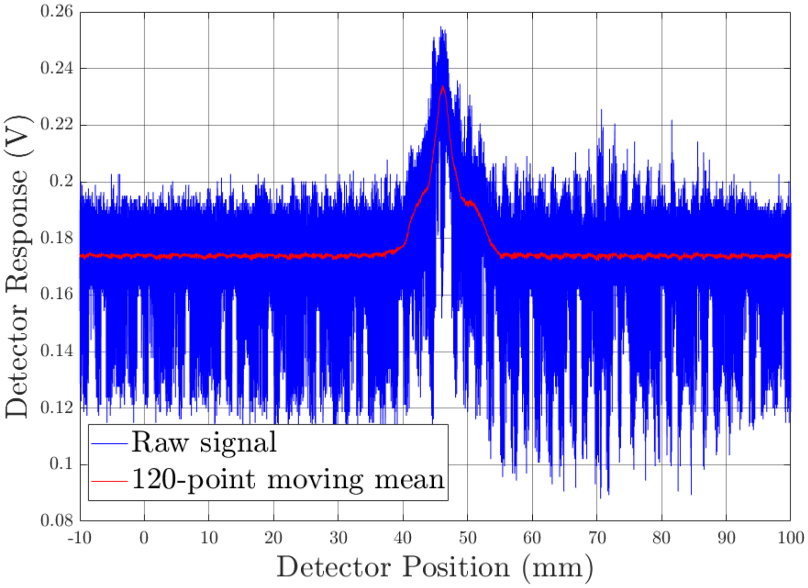

Figure 75: Full sweep dataset for laser position 45mm Sample 1

Factoring in the known open air transmittance and correcting for reflection this corresponds to a loss of -23.85dB across the crystal, which implies an absorption coefficient of 0.2603 cm^{-1}, as can be seen in Fig.76.

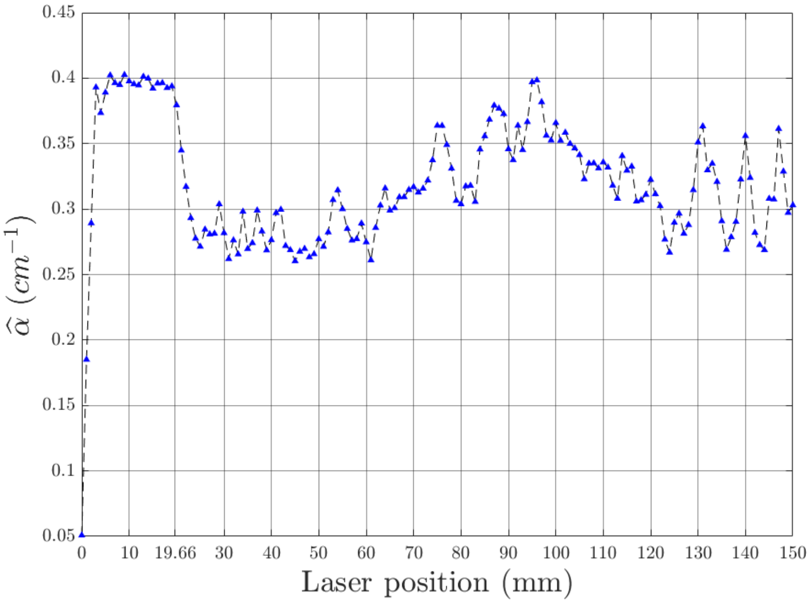

Figure 76: Estimated absorption coefficient for sample 1, assuming beam crosses full diameter and has a normal angle of incidence

The model derived in Sec.2.4.7 predicted a maximum of 0.1272 cm^{-1} while Schroder's model[31] predicted a maximum of 0.2731, which implies that Schroder's model is more accurate.

Given that Sample 1 is a product of a structure loss, it is also a strong possibility that there are internal dislocations that may be adding to the absorption and scattering. In addition to this, it is worth noting the drop in transmittance from approximately 62mm which then stretches to approximately 122mm, a possible explanation being shown in Fig.77.

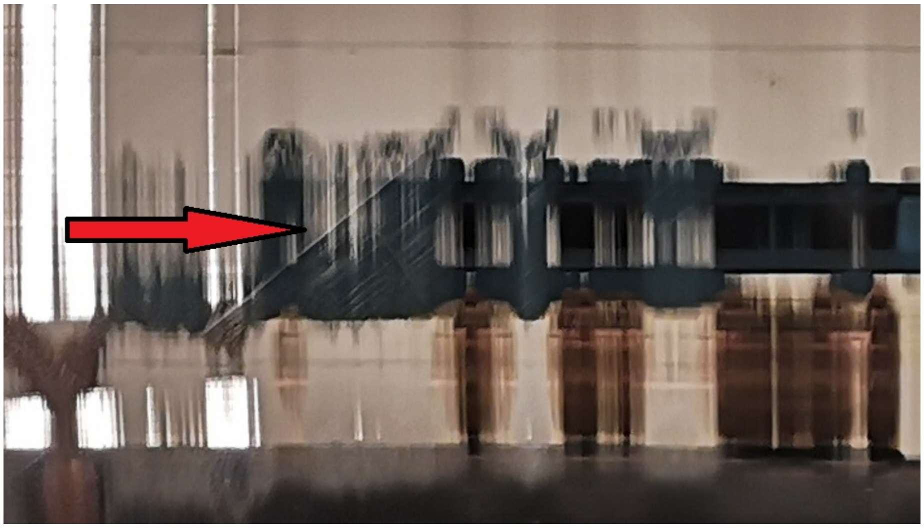

Figure 77: Close up image of Sample 1, showing slip lines

While they may appear as simple scratches, the lines shown in Fig.77 are not caused by external damage, these slip lines commonly appear as hair-thin parallel lines radiating from the nodes at approximately 45° angles(depending on crystal orientation). The presence of such lines indicates the occurrence of macroscopic slip dislocations and are a common precursor to a structure loss, as it was with this sample.

We can see similar dislocations pictured in Fig. 1 of the works of Meyer et al.[45] where it was shown that such dislocations in both Germanium and Silicon have a measurable effect on the local optical properties. It was shown that carrier mobility was generally lowered by the presence of the dislocations, which would lead to a higher absorption coefficient as discussed in Sec.2.4.5. Furthermore, Meyer showed that the mobility surrounding the dislocations were anisotropic, having a higher mobility in parallel than normal to the dislocations the effects of which are illustrated in Fig.78.

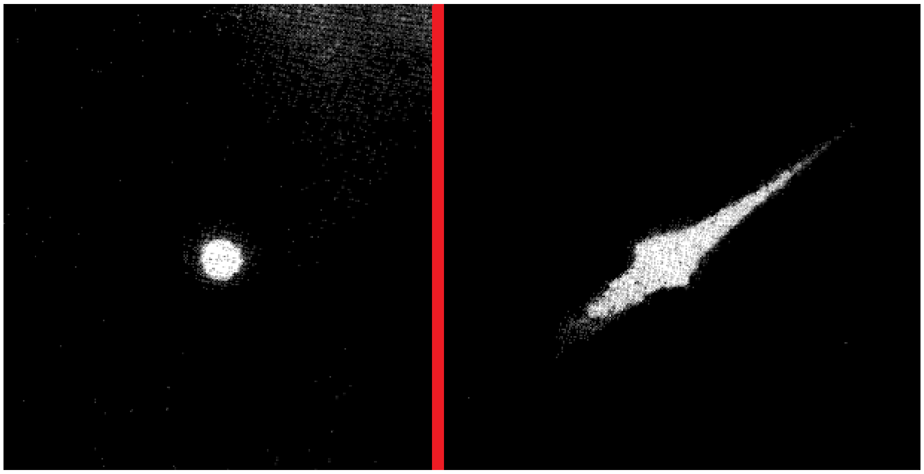

Figure 78: Comparison between radiation picture of undeformed Si and deformed Si with slip dislocations, cropped from Figs. 6 and 7 of Meyer et al.[45]

This effect implies a polarization dependence in the transmission as well as a dependence on the crystals angle of rotation.
Considering that the laser is strongly polarized approximately orthogonal to the central axis and the crystal rotation is approximately 45° relative to the nodes, we would expect the beam to intersect the dislocations having both TM and TE polarization components. Since the slip planes emanate from the nodes, marked by the slip lines, it can then be expected that a beam aligned to the center axis intersects several dislocation layers of alternating orientation. This in term would lead to scattering parallel to each dislocation, most of which would be largely normal to the next slip dislocation, resulting in the beam being increasingly scattered and subsequently absorbed as it passes through more dislocations.

7.1.2 Sample 2

As can be seen in Fig.59, the transmittance through sample 2 is notably higher than that of sample 1. After factoring in the open air transmittance of 51.1%, the surface transmission of 48.7% and the transmittance at the calibrated zero-point of -10.7dB, the mean relative response of -20.3dB and max of -15.7dB correspond to a transmittance of -24.9dB and -20.4dB through the crystal. These transmittances then imply an absorption coefficient of $0.27cm^{-1}$ and $0.22cm^{-1}$, respectively.
As shown in Fig.79, the estimated absorption coefficient $\widehat{\alpha}$ sharply drops from approximately $0.4cm^{-1}$ to below $0.3cm^{-1}$ as the scan position goes above the interface peak at 10.96mm. The absorption coefficient stays within a relatively narrow range(0.22-0.32) up to 125mm, the estimate then begins fluctuating before returning to the no-signal level of approximately $0.4cm^{-1}$ as the beam begins interacting with the shoulder section of the sample.

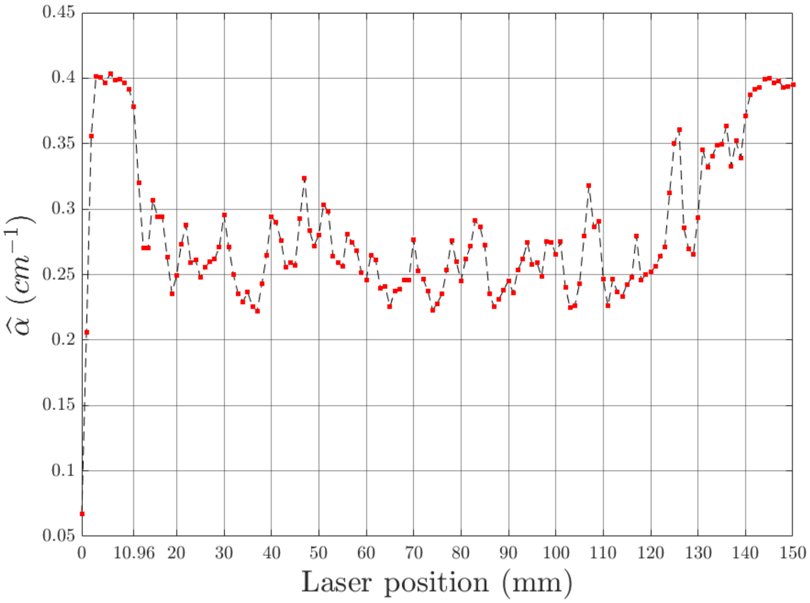

Figure 79: Estimated absorption coefficient for sample 2, assuming beam crosses full diameter and has a normal angle of incidence

7.1.3 Sample 3

As suggested in Sec.6.1, the results show that the transmittance through sample 3 is comparatively better than that of both sample 2 and, by far, sample 1.

The relative corrected transmittance mean of -18.6dB and max of -13.3dB, corresponding to a crystal transmittance of -23.2dB and -17.9dB, implies a mean absorption coefficient of $\overline{\alpha} = 0.25cm^{-1}$ and a minimum of $0.20cm^{-1}$.

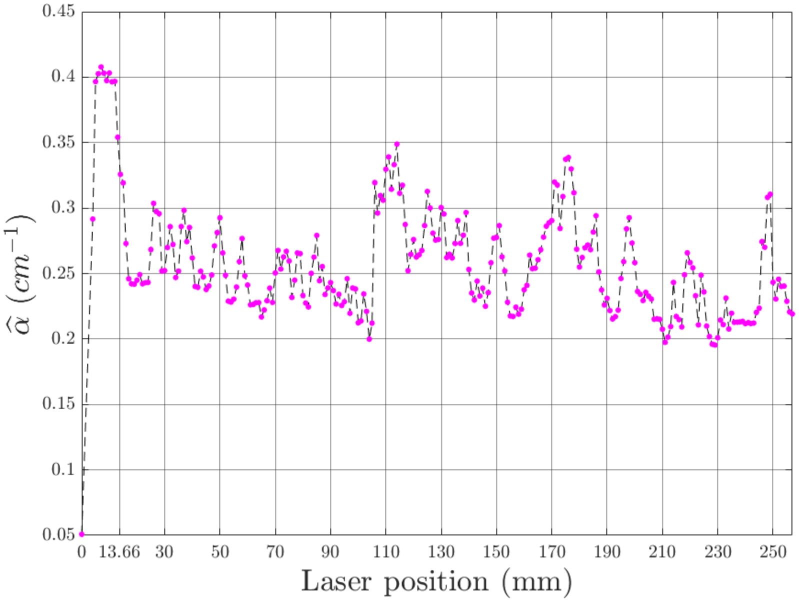

Figure 80: Estimated absorption coefficient for sample 3, assuming beam crosses full diameter and has a normal angle of incidence

As is shown in Fig.80, the absorption coefficient again drops drastically from approximately $0.4cm^{-1}$ to below $0.3cm^{-1}$ as the scan position passes the interface peak. The estimate for the coefficient appears to stay within a narrow range up to 105mm. As the scan position reaches 106mm, the estimate jumps from 0.21 to 0.32 and proceeds to vary greatly for the remainder of the scans. The likely cause of this can be seen in the lower plot of Fig.62, showing the estimated noise DC component dropping noticeably between 55mm and 105mm compared to the rest of the scans. A likely cause of this was the order and time of the separate scans. As the 8MT175-50 translation stage of the laser only has a travel range of 50mm and the 7T175-100 stage of the sample holder has a range of 150mm, this means that a maximum of 150mm can be scanned before the sample must be removed and the sample holding assembly moved to expose a new range. Due to the length(389mm) of sample 3 it presented as the best candidate for a more extensive transmittance scan, which would require it to be moved at least once in addition to initial setup and post-scan cleanup. Due to the fact that sample 3 is quite heavy(34kg+) and has to be carried by hand, I elected to get it over with at the beginning of the day. Because of the initial position, the range 55-105mm was then scanned first before moving on to 4-54mm, 160-156mm, then, after reconfiguring the placement of the sample holding assembly, 157-207mm, and 208-258mm. As shown in both Sec.6.3.2 and the various plots of the DC noise, the noise of the detector becomes stronger and more distributed the longer it is active. The detector was then "cold" when the 55-105mm scan was performed and gradually became more noisy during the 4-54mm scan, leading to the gradual increase appearing as a sudden jump from 105mm to 106m when, in reality, those two measurements were taken almost an hour apart.

7.2 Interface Reflection

7.2.1 Sample 1

Given the measured interface deflection of $19.66 \pm 0.002mm$ and the detector angle of 10°, the entry and exit heights of the beam are then $27.62mm$ above the separation plane. Considering the laser-crystal distance of $L_0 = 76mm$, an offset of $L_a = 22mm$ from the rotation axis of the laser and a crystal-detector distance of $L_{CD} = 42mm$, the optimum laser position would then be $50.26mm$ and detector position of $38.88mm$. Because the required laser position is above the maximum travel range of the laser assembly, the standard calibration method of aligning both laser and detector against each other at the separation plane(height of 0mm) is not possible. Instead, the alignment was done by using an indicator card to determine when the oblique beam intersects the bottom edge of the sample and setting that as effective zero. Because of the laser being relatively weak and the VRC6H detector card both being highly sensitive to temperature and having a slow response, the alignment cannot be considered as accurate as when it is obtained by the auto-alignment sequence.

Another issue is the alignment of the sample and setup, as was a significant challenge with sample 2. The results shown in Fig.69 were obtained on the third attempt, after realigning the setup twice. One of the reasons why the alignment was so challenging for sample 2 was the fact that the high interface deflection means a high change in the surface angle of the interface. Assuming that the interface can be described as a parabola, then the angle of the interface, relative to the r-axis, can be determined as:

$$I\left(r\right) = h_0 \left[1 - \left(\frac{r}{r_0}\right)^2\right] \Rightarrow \theta_I\left(r\right) = \arctan\left[\frac{d}{dr} I\left(r\right)\right] = \arctan\left[-2\frac{h_0}{{r_0}^2}\right] \tag{48}$$

where r_0 is the body radius, and h_0 is the peak deflection. This means that for a specified maximum interface angle, the reflection maximum offset form crystal center can be defined as:

$$|r| \leq -\frac{{r_0}^2}{2h_0} \tan\left(\theta_{Max}\right) \tag{49}$$

Given the interface deflection of 19.66mm for sample 1, the maximum allowed deviation for a given angle is 55.7% compared to sample 2 and 70.0% compared to sample 3, giving a relative surface area of 31.1% and 49.0%, respectively.

7.2.2 Sample 2

For sample 2, it was found that approximately 34.2% of the detected beams registered as valid reflections, with the remaining 65.8% of captures shown in Fig.81.

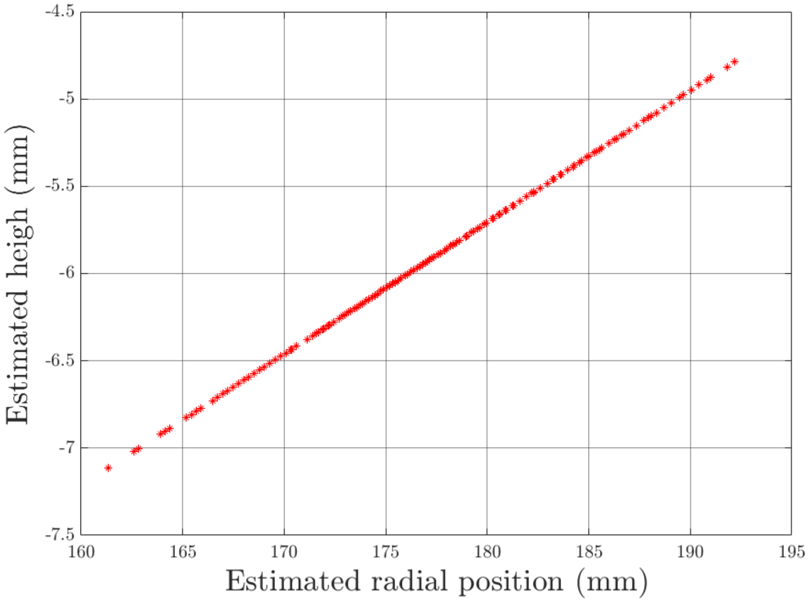

Figure 81: Returned reflection point estimates for invalid beam captures of sample 2 reflections

As Fig.81 shows, the estimated "reflection" points returned for the majority of the measurements fall outside the sample, due to the peak detection returning zero during the test. As can be seen in the script in Appendix C, this means that the matched filter response had a peak less than 50% greater than the mean response. While this can be caused by the beam either missing the interface or that it hit at a position where the local surface angle was too far from horizontal for the beam to be captured.
Considering that the detector can accept angles deviating by up to 1.43° from 15°, under the assumption of perfectly flat crystal walls then the internal angle

after reflection can vary by approximately 0.4° in either direction. This means that the absolute angle of the interface at the point of reflection must be less than 0.2°. Considering what was discussed in Sec.7.2.1, this means that for an interface height of 10.96mm and a nominal radius of 105.5mm, the radial position of the interface reflection must be within 1.77mm of the peak at the center.

This presents a small target vulnerable to many distortions, but considering that sample 1, with a radial limit of 0.99mm, received over twice as many valid reflections as sample 2 it seems unlikely that this is the cause.

In the works of Liao et al.[47] it was shown that for accelerated cooling rates, the interface between a solid crystal and the liquid material begins forming a step-like facets instead of a locally planar interface. Considering the imperfections seen on the bottom of the interfaces of both sample 2 and 3, it is possible that the "mold"-like groups seen in Figs.46 and 48 are such step imperfections. As stated in Sec.6.1, the growth process for both sample 2 and 3 were aborted due to a sudden power loss, meaning that the influx of heat by the heating elements would have stopped immediately while the cooling system would have switched to backups and remained operational. Therefore, it is very possible that the effective cooling rate of the crystal would have accelerated sufficiently to cause facets like what was shown in Fig. 9 of Liao[47]. If this is the case, then the interior aspect of the facets may cause the interface to act more like a diffuse surface than a perfect mirror. The near perfect mirror properties seen in Fig.44 for the sample 1 interface versus the imperfect interface of sample 2 may therefore be the reason why so few usable captures were obtained.

7.2.3 Sample 3

As stated, no reflected beams were successfully captured from the interface of sample 3.

This may be, in part, due to the imperfections in the interface surface as is suspected for sample 2. Another considerable factor is, again, the size and weight of sample 3. Having a length of 389mm plus shoulder and neck, placing sample 3 onto the sample holder means a significant overhang on both sides. This means that the lengthwise support is relatively poor and can lead to the sample, and thereby the interface, having an angle in the h/z-plane. Attempts were made to remedy this by placing makeshift supports under the ends in an attempt to level the sample, but the expected accuracy of this is quite poor.

Due to the sample holder being required to hold the full 34kg+ of sample 3, it was made from aluminium. To prevent the holder from damaging the samples, a packaging foam was placed between the samples and the holder. This foam was approximately 10mm thick and is semi-rigid, this means that while it performed perfectly for samples 1 and 2, the weight of sample 3 was sufficient for the foam to begin compressing. After the failed attempts at measuring sample 3, the sample was removed and the foam was shown to have been compressed to less than 6mm over approximately 3 hours. This means that even if adequate alignment was achieved at the beginning of the test, the gradually compressing foam padding may have shifted the sample down the z-axis. This would have both shifted the z-axis position of the beam entry point and would have caused the height of the added sample supports to become misaligned, resulting in the sample no longer being level.

8 Conclusion

The absorption spectrum of doped mono-crystalline Silicon was modelled using the expression:

$$\begin{aligned}\alpha_{Ex,B+A_i}\left(\nu,T\right) = \chi\left(h\nu\right)&\left\{\frac{C_1\left(T\right)}{E_{g,D}(\mathbf{0},T)^2[h\nu - E_{g,D}\left(\mathbf{0},T\right)]^2}+\right.\\ &\left.\frac{C_2\left(T\right)}{E_{g,D}(\mathbf{p}_0,T)^2[h\nu - E_{g,D}\left(\mathbf{p}_0,T\right)]^2} + \frac{C_3\left(T\right)}{{E_a}^2\left(T\right)\left[h\nu - E_a\left(T\right)\right]^2}\right\},\\ &\times D\eta\left(\mathbf{p}_0,T\right)\left(h\nu - E_g\left(T\right)\right)^2 h\nu + C_{FCA}\left(\nu,T\right)\nu^{-2}N\end{aligned}$$

with the step function $\chi\left(h\nu\right) = \begin{cases}1 : h\nu \geq E_g\left(T\right)\\ 0 : h\nu < E_g\left(T\right)\end{cases}$, the coefficient $D = \frac{e^2\left(4m_v m_v\right)^{\frac{3}{2}}}{48\pi m^2}$ and the relative Fermi-Dirac distribution of phonons $\eta\left(\mathbf{p}_0\right) = 2n\left(\mathbf{p}_0\right) + 1 = \frac{e^{\frac{\Omega(\mathbf{p}_0)}{kT}}+1}{e^{\frac{\Omega(\mathbf{p}_0)}{kT}}-1}$.

The temperature dependence of the energies $E_{g,D}\left(\mathbf{0},T\right)$, $E_{g,D}\left(\mathbf{p},T\right)$, and $E_a\left(T\right)$ being modelled using the Varshni equation:

$$E\left(T\right) = E\left(0\right) + \frac{\alpha T^2}{T+\beta}$$

The temperature dependece of the coupling coefficients $C_1\left(T\right)$, $C_2\left(T\right)$, and $C_3\left(T\right)$ were modelled using an exponential function:

$$C\left(T\right) = \gamma e^{\delta T}$$

The parameters of which were determined as:

Energy	$E_x\left(0\right)$	α	β	Coef.	γ	δ
$E_{g,D}\left(\mathbf{0},T\right)$	3.432	$-2.6\cdot10^{-4}$	844.1	$C_1\left(T\right)$	35.56	$1.12\cdot10^{-3}$
$E_{g,D}\left(\mathbf{p},T\right)$	3.866	$-1.8\cdot10^{-3}$	522.2	$C_2\left(T\right)$	413.5	$-1.98\cdot10^{-3}$
$E_a\left(T\right)$	0.331	$-7.7\cdot10^{-2}$	$2.7\cdot10^{6}$	$C_3\left(T\right)$	63.31	$-2.76\cdot10^{-4}$

And, the free carrier coefficient C_{FCA} defined as:

$$C_{FCA}\left(\nu,T\right) = \frac{q^3}{4\pi^2\varepsilon_0 c n\left(\nu,T\right)\left(m^*\left(T\right)\right)^2\mu\left(T\right)},$$

with the refractive index:

$$n\left(\nu\right) = \sqrt{11.67316 + \frac{\nu^2}{c^2} + \frac{0.004482633c^2}{\nu^2 - \left(1.108205c\right)^2}}$$

The absorption coefficient at 1687K was then estimated as $1.56 \cdot 10^4 cm^{-1}$ for $\lambda = 1.10 \mu m$, $13.7 cm^{-1}$ for $\lambda = 2.55 \mu m$, and $9.82 cm^{-1}$ for the optimum wavelength of $\lambda = 2.16 \mu m$ for a dopant concentration of $2.8 \cdot 10^{16} cm^{-3}$.

The peak interface deflections for three samples were measured using a transmittance scan:

Sample	True Deflection	Measured	Threshold	Classification Error
1	19.66mm	20-21mm	-29.5dB	5.34%
2	10.96mm	10-11mm	-30.4dB	0%
3	13.76mm	13-14mm	-27.6dB	0%

Measurements were also taken by ray tracing of the beam reflected off of the interface:

Sample	True Deflection	Measured
1	19.66mm	$19.35 \pm 0.79 mm$
2	10.96mm	$11.02 \pm 1.21 mm$
3	13.76mm	N/A

The tests confirm that a measurement system as shown in Fig.1 could work in theory, albeit the significant challenges of alignment in a practical setting. However, given the minimum absorption found for 1687K being $9.82 cm^{-1}$ at $\lambda = 2.16 \mu m$, Silicon was found to not be effectively transparent for the conditions expected during production.

9 Future work

As stated in Sec.2.4, there is a sever lack of available data regarding the absorption near the intrinsic absorption edge for elevated temperatures. As such, the first thing that needs to be done, should this concept advance, is to take detailed readings of the absorption at temperatures near 1687K.

Should this system ever be attempted to be implemented, it would also require a significantly more sensitive detector than the PDA10D2 used here. It would also require a much larger aperture as to deal with the inevitable misalignment issues we would expect in praxis.

References

[1] S. Rühle *Tabulated values of the Shockley–Queisser limit for single junction solar cells.*
Solar Energy, Vol. 130, p. 139, Jun 2016.
`https://doi.org/10.1016/j.solener.2016.02.015`

[2] K. Jiptner, B. Gao, H. Harada, Y. Miyamura, M. Fukuzawa, K. Kakimoto, and T. Sekiguchi *Thermal stress induced dislocation distribution in directional solidification of Si for PV application.*
Journal of Crystal Growth, Vol. 408, p. 19, Dec 2015.
`https://doi.org/10.1016/j.jcrysgro.2014.09.017`

[3] Y. Shiraishi, S. Meada, and K. Nakamura *Prediction of solid–liquid interface shape during CZ Si crystal growth using experimental and global simulation.*
Journal of Crystal Growth, Vol. 266, Iss. 1-3, p. 28, May 2004.
`https://doi.org/10.1016/j.jcrysgro.2004.02.026`

[4] B. E. A. Saleh and M. C. Teich *Fundamentals of Photonics, 2nd ed..*
John Wiley & Sons, Hoboken, New Jersey, 2007.
ISBN:978-0-471-35832-9

[5] M.A. Green *Self-consistent optical parameters of intrinsic silicon at 300 K including temperature coefficients.*
Solar Energy Materials and Solar Cells, Vol. 92, Iss. 11, p. 1305, Nov 2008 .
`https://doi.org/10.1016/j.solmat.2008.06.009`

[6] R. Uecker *The historical development of the Czochralski method.*
Journal of Crystal Growth, Vol. 401, p. 7, Sep 2014.
`https://doi.org/10.1016/j.jcrysgro.2013.11.095`

[7] E v Gomperz *Untersuchungen an Einkristalldrähten.*
Zeitchrift für Physix, Vol. 8, Iss. 1, p. 184, Dec 1922.
`https://doi.org/10.1007/BF01329591`

[8] H. Walther *Preparation of Large Single Crystals of Sodium Chloride.*
Review of Scientific Instruments, Vol. 8, Iss. 11, p. 406, Jul 1937.
`https://doi.org/10.1063/1.1752200`

[9] A. G. Hoyem and E. P. T. Tyndall *An Experimental Study of the Growth of Zinc Crystals by the Czochralski-Gomperz Method.*
Physical Review, Vol. 33, Iss. 1, p. 81, Jan 1929.
`https://doi.org/10.1103/PhysRev.33.81`

[10] P. L. Moody and C. Kolm *Syringe-Type Single-Crystal Furnace for Materials Containing a Volatile Constituent.*
Review of Scientific Instruments, Vol. 29, Iss. 12, p. 1144, Sep 1958.
`https://doi.org/10.1063/1.1716102`

[11] William C. Dash *Growth of Silicon Crystals Free from Dislocations.*
Journal of Applied Physics, Vol. 30, Iss. 4, p. 459, Apr 1959.
`https://doi.org/10.1063/1.1702390`

[12] L.Y. Huang, P.C. Lee, C.K. Hsieh, W.C. Hsu, and C.W. Lan *On the hot-zone design of Czochralski silicon growth for photovoltaic applications.*
Journal of Crystal Growth, Vol. 261, Iss. 4, p. 433, Feb 2004.
`https://doi.org/10.1016/j.jcrysgro.2003.09.039`

[13] Y.Y. Teng, J.C. Chen, C.C. Huang, C.W. Lu, W.T. Wun, and C.Y. Chen *Numerical investigation of the effect of heat shield shape on the oxygen impurity distribution at the crystal–melt interface during the process of Czochralski silicon crystal growth.*
Journal of Crystal Growth, Vol. 352, Iss. 1, p. 167, Aug 2012.
`https://doi.org/10.1016/j.jcrysgro.2011.12.070`

[14] N. Machida, Y. Suzuki, K. Abe, N. Ono, M. Kida, and Y. Shimizu *The effects of argon gas flow rate and furnace pressure on oxygen concentration in Czochralski-grown silicon crystals.*
Journal of Crystal Growth Vol. 186, Iss. 3, p. 362, Mar 1998.
`https://doi.org/10.1016/S0022-0248(97)00491-0`

[15] O.A.Noghabi, M. M'Hamdi, and M. Jomâa *Effect of crystal and crucible rotations on the interface shape of Czochralski grown silicon single crystals.*
Journal of Crystal Growth Vol. 318, Iss. 1, p. 173, Mar 2011.
`https://doi.org/10.1016/j.jcrysgro.2010.11.113`

[16] E.W. Lemmon and R.T. Jacobsen *Viscosity and Thermal Conductivity Equations for Nitrogen, Oxygen, Argon, and Air.*
International Journal of Thermophysics Vol. 25, Issue 1, pp 21-69, Jan 2004.
`https://doi.org/10.1023/B:IJOT.0000022327.04529.f3`

[17] C.J. Glassbrenner and G.A. Slack *Thermal Conductivity of Silicon and Germanium from 3°K to the Melting Point.*
Physical Review, Vol. 134, Iss. 4A, A1058, May 1964.
`https://doi.org/10.1103/PhysRev.134.A1058`

[18] H. Nagai, Y. Nakata, T. Tsurue, H. Minagawa, K. Kamada, S.E. Gustafsson and T. Okutani *Thermal Conductivity Measurement of Molten Silicon by a Hot-Disk Method in Short-Duration Microgravity Environments.*
Japanese Journal of Applied Physics, Vol. 39, 1405, Mar 2000.
`https://doi.org/10.1143/JJAP.39.1405`

[19] C. N. Berglund *Temperature-Modulated Optical Absorption in Semiconductors.*
Journal of Applied Physics, Vol. 37, Iss. 8, p. 3019, Jan 1966.
`https://doi.org/10.1063/1.1703156`

[20] K. Yamaguchi and K. Itagaki *Measurement of high temperature heat content of silicon by drop calorimetry.*
Journal of Thermal Analysis and Calorimetry, Vol. 69, Iss. 3, p. 1059, Jul 2002.
`https://doi.org/10.1023/A:1020609517891`

[21] J. R. Chelikowsky and M. L. Cohen *Nonlocal pseudopotential calculations for the electronic structure of eleven diamond and zinc-blende semiconductors.*
Physical Review B, Vol. 14, Iss. 2, p. 556, Jul 1976.
`https://doi.org/10.1103/PhysRevB.14.556`

[22] W. Rhim and K. Ohsaka *Thermophysical properties measurement of molten silicon by high-temperature electrostatic levitator: density, volume expansion, specific heat capacity, emissivity, surface tension and viscosity.*
Journal of Crystal Growh Vol. 208, Iss. 1-4, p. 313, Jan 2000.
`https://doi.org/10.1016/S0022-0248(99)00437-6`

[23] R. Endo and Y. Fujihara *Calculation of the density and heat capacity of silicon by molecular dynamics simulation.*
High Temperatures-High Pressures Vol. 35, Iss. 5, p. 505, Jan 2003.
`https://doi.org/10.1068/htjr135`

[24] T. Satō *Spectral Emissivity of Silicon.*
Japanese Journal of Applied Physics Vol. 6, No. 3, p. 339, Mar 1967.
`https://doi.org/10.1143/JJAP.6.339`

[25] Samuel N. Rea *Czochralski silicon pull rate limits.*
Journal of Crystal Growth Vol. 54, Iss. 2, p. 267, Aug 1981.
`https://doi.org/10.1016/0022-0248(81)90471-1`

[26] B. Van Zeghbroeck *Principles of Electronic Devices*
`http://apachepersonal.miun.se/~gorthu/halvledare/Energy%20bands.htm`

[27] W. S. Chow *Theory of Phonon-Assisted Optical Absorption in Semiconductors.*
Physical Review Vol. 185, Iss. 3, p. 1056, Sep 1969.
`https://doi.org/10.1103/PhysRev.185.1062`

[28] D. Dunn *Absorption in the Electron-Optical-Phonon System.*
Physical Review Vol. 166, Iss. 3, p. 822, Sep 1967.
`https://doi.org/10.1103/PhysRev.166.822`

[29] J. Singh *Physics of semiconductors and their heterostructures.*
Singapore, McGraw-Hill, 1993.
ISBN: 0070576076 9780070576070

[30] Bart J. Van Zeghbroeck *Principles of Semiconductor Devices.*
`https://ecee.colorado.edu/~bart/book/eband6.htm`

[31] D. K. Schroder, R. N. Thomas, and J. C. Swartz *Free Carrier Absorption in Silicon.*
IEEE Journal of Solid-State Circuits Vol. 13, Iss. 1, Feb 1978.
`https://doi.org/10.1109/JSSC.1978.1051012`

[32] J. Šik, J. Hora, and J. Humlíček *Optical functions of silicon at high temperatures.*
Journal of Applied Physics Vol. 84, Iss. 11, p. 6291, Dec 1998 .
`https://doi.org/10.1063/1.368951`

[33] C. Schinke, P.C. Peest, J. Schmidt, R. Brendel, K. Bothe, M.R. Vogt, I. Kröger, S. Winter, A. Schirmacher, S. Lim, H.T. Nguyen, and D. MacDonald *Uncertainty analysis for the coefficient of band-to-band absorption of crystalline silicon.*
AIP Advances, Vol. 5, Iss. 6, 067168, Jun 2015.
`https://doi.org/10.1063/1.4923379`

[34] D. Chandler-Horowitz and P. M. Amirtharaj *High-accuracy, midinfrared* $\left(450cm^{-1} \leq \omega \leq 4000cm^{-1}\right)$ *refractive index values of silicon.*
Journal of Applied Physics, Vol. 97, Iss. 12, Apr 2005
`https://doi.org/10.1063/1.1923612`

[35] D. F. Edwards and E. Ochoa *Infrared refractive index of silicon.*
Applied Optics, Vol. 19, Iss. 24, 1980
`https://doi.org/10.1364/AO.19.004130`

[36] H. H. Li *Refractive index of silicon and germanium and its wavelength and temperature derivatives.*
Journal of Physical and Chemical Reference Data, Vol. 9, Iss. 3, Oct 2009
`https://doi.org/10.1063/1.555624`

[37] C. D. Salzberg and J. J. Villa *Infrared Refractive Indexes of Silicon Germanium and Modified Selenium Glass.*
Journal of the Optical Society of America, Vol. 47, Iss. 3, 1957
`https://doi.org/10.1364/JOSA.47.000244`

[38] D. K. Schroder, R. N. Thomas and J. C. Swartz *Free Carrier Absorption in Silicon.*
IEEE Journal of Solid-State Circuits, Vol. 13, Iss. 1, Feb 1978
`https://doi.org/10.1109/JSSC.1978.1051012`

[39] G. F. Sinclair, N. A. Tyler, D. Sahin, J. Barreto, and M. G. Thompson *Temperature Dependence of the Kerr Nonlinearity and Two-Photon Absorption in a Silicon Waveguide at 1.55*μm*.*
Physical Review Applied, Vol. 11, Iss. 4, Apr 2019
`https://doi.org/10.1103/PhysRevApplied.11.044084`

[40] M. Dinu *Dispersion of phonon-assisted nonresonant third-order nonlinearities.*

IEEE Journal of Quantum Electronics, Vol. 39, Iss. 11, Nov 2003.
`https://doi.org/10.1109/JQE.2003.818277`

[41] Y. P. Varshni *Temperature dependence of the energy gap in semiconductors.*
Physica, Vol. 34, Iss. 1, 1967.
`https://doi.org/10.1016/0031-8914(67)90062-6`

[42] J. Batista, A. Mandelis, and D. Shaughnessy *Temperature dependence of carrier mobility in Si wafers measured by infrared photocarrier radiometry.*
Applied Physics Letter, Vol. 82, Iss. 23, Apr 2003.
`https://doi.org/10.1063/1.1582376`

[43] B. J. Frey, D. B. Leviton, and T. J. Madison *Temperature-dependent Refractive Index of Silicon and Germanium.*
NASA Conference Paper, SPIE Astronomical Telescopes and Instruments Conference, May 2006.
`https://ntrs.nasa.gov/search.jsp?R=20070021411`

[44] N. Cavassilas and J. Autran *Energy and temperature dependence of electron effective masses in silicon.*
Journal of Applied Physics, Vol. 92, Iss. 3, May 2002.
`https://doi.org/10.1063/1.1490620`

[45] M. Meyer, M. H. Miles, and T. Ninomiya *Some Electrical and Optical Effects of Dislocations in Semiconductors.*
Journal of Applied Physics, Vol. 38, Iss. 11, Feb 1967.
`https://doi.org/10.1063/1.1709153`

[46] V. Alex, S. Finkbeiner, and J. Weber *Temperature dependence of the indirect energy gap in crystalline Silicon.*
Journal of Applied Physics, Vol. 79, Iss. 9, Jan 1996.
`https://doi.org/10.1063/1.362447`

[47] T. J. Liao, Y. S. Kand, and C. W. Lan *In situ observation of crystal/melt interface and infrared measurement of temperature profile during directional solidification of silicon wafer.*
Journal of Crystal Growth, Vol. 499, Oct 2018.
`https://doi.org/10.1016/j.jcrysgro.2018.08.004`

Appendix A: Laser datasheet(scan)

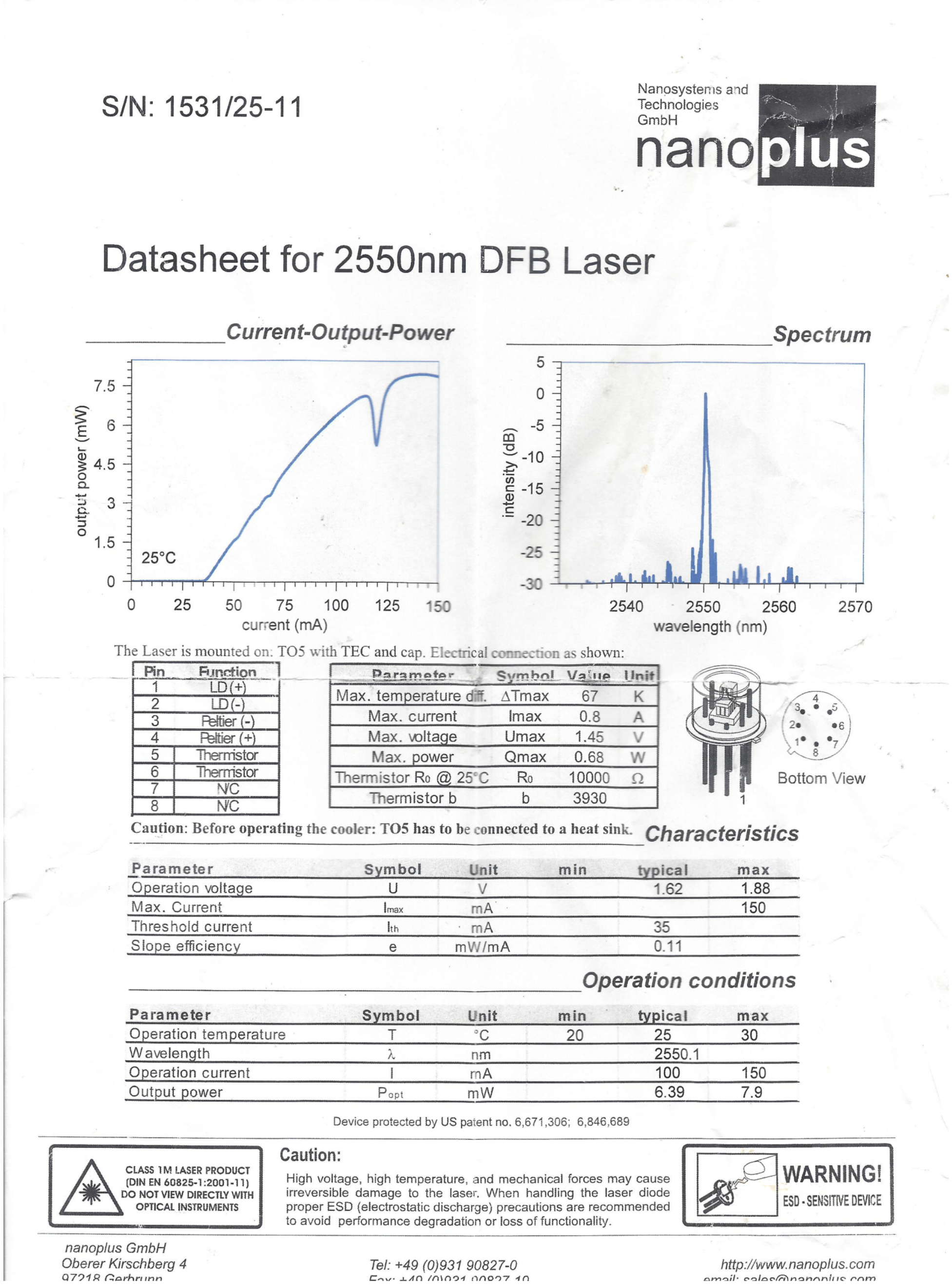

S/N: 1531/25-11

Nanosystems and
Technologies
GmbH
nanoplus

Datasheet for 2550nm DFB Laser

The Laser is mounted on: TO5 with TEC and cap. Electrical connection as shown:

Pin	Function
1	LD(+)
2	LD(-)
3	Peltier (-)
4	Peltier (+)
5	Thermistor
6	Thermistor
7	N/C
8	N/C

Parameter	Symbol	Value	Unit
Max. temperature diff.	ΔTmax	67	K
Max. current	Imax	0.8	A
Max. voltage	Umax	1.45	V
Max. power	Qmax	0.68	W
Thermistor R_0 @ 25°C	R_0	10000	Ω
Thermistor b	b	3930	

Caution: Before operating the cooler: TO5 has to be connected to a heat sink.

Characteristics

Parameter	Symbol	Unit	min	typical	max
Operation voltage	U	V		1.62	1.88
Max. Current	I_{max}	mA			150
Threshold current	I_{th}	mA		35	
Slope efficiency	e	mW/mA		0.11	

Operation conditions

Parameter	Symbol	Unit	min	typical	max
Operation temperature	T	°C	20	25	30
Wavelength	λ	nm		2550.1	
Operation current	I	mA		100	150
Output power	P_{opt}	mW		6.39	7.9

Device protected by US patent no. 6,671,306; 6,846,689

Caution:

High voltage, high temperature, and mechanical forces may cause irreversible damage to the laser. When handling the laser diode proper ESD (electrostatic discharge) precautions are recommended to avoid performance degradation or loss of functionality.

nanoplus GmbH
Oberer Kirschberg 4
97218 Gerbrunn

Tel: +49 (0)931 90827-0
Fax: +49 (0)931 90827-10

http://www.nanoplus.com
email: sales@nanoplus.com

Appendix B: Excerpt from PDA10D2 manual

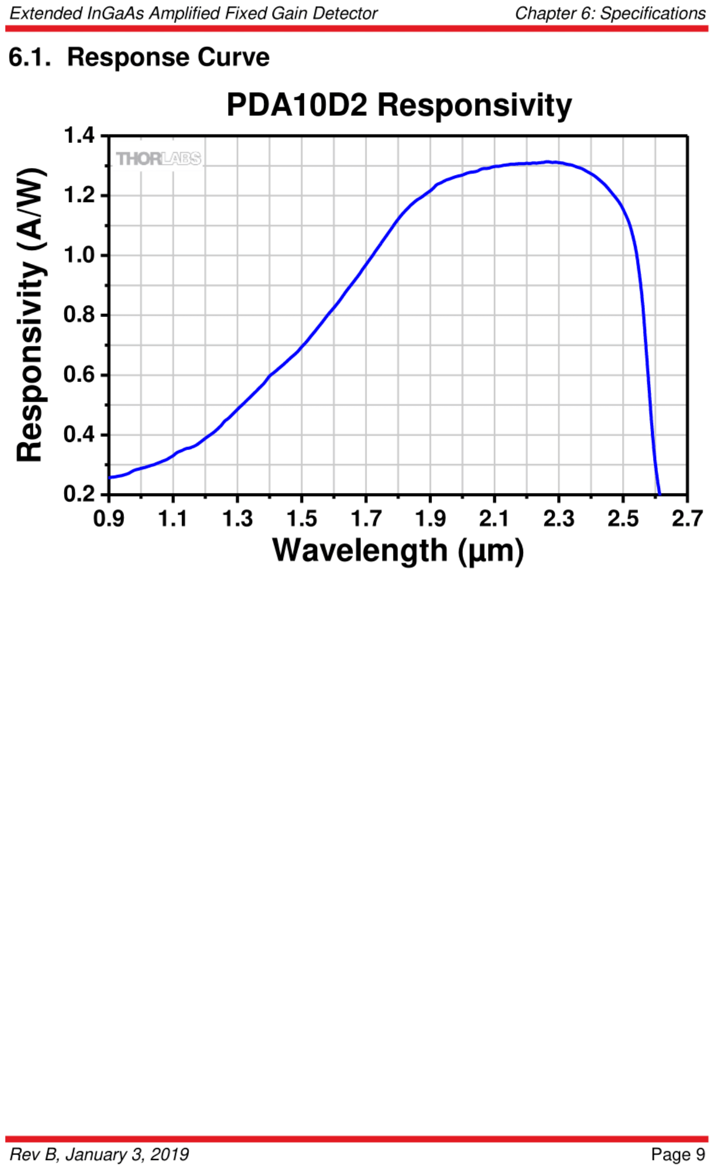

Extended InGaAs Amplified Fixed Gain Detector *Chapter 6: Specifications*

6.1. Response Curve

Rev B, January 3, 2019 Page 9

Appendix C: Python scripts

Listing 1: Initialization of environment

```
from ctypes import *
import time as t
import os
import sys
import platform
import tempfile
import re
import urllib.parse
import math
import numpy as np
import nidaqmx
import csv
from nidaqmx.constants import AcquisitionType, Edge
from nidaqmx.stream_readers import AnalogSingleChannelReader
import numpy.random as nr
from matplotlib import pyplot as plt

#---------------------------------------------------------------------------

cur_dir = os.path.abspath(os.path.dirname(__file__)) #Directory of this file
ximc_dir = os.path.join(cur_dir,"ximc")
ximc_package_dir = os.path.join(ximc_dir, "crossplatform", "wrappers", "python")
sys.path.append(ximc_package_dir)  # add ximc.py wrapper to python path

libdir = os.path.join(ximc_dir, "win64")
os.environ["Path"] = libdir + ";" + os.environ["Path"]  # add dll
os.add_dll_directory(libdir) #Add lib dll to OS lib-directory

try:
    from pyximc import *
except ImportError as err:
    print ("Can't␣import␣pyximc␣module!")
    exit()
except OSError as err:
    print ("Can't␣access␣library␣dll␣file!")
    input()
    exit()
#Check if lib can be imported

sbuf = create_string_buffer(64)      #String buffer
lib.ximc_version(sbuf)               #Set sbuf as library version
print("Successfully␣loaded␣ximc␣library,␣version:␣"+sbuf.raw.decode().rstrip("\0"))

lib.set_bindy_key(os.path.join(cur_dir,"ximc", "win32",
"keyfile.sqlite").encode("utf-8"))
#Set bindy keyfile for networked devices(not implemented)

probe_flags = EnumerateFlags.ENUMERATE_PROBE + EnumerateFlags.ENUMERATE_NETWORK
enum_hints = b"addr=192.168.0.1,172.16.2.3"
devenum = lib.enumerate_devices(probe_flags, enum_hints)
#Temp values for enumeration and flagging of detected devices
print("Detecting␣devices\n--------------------")
```

```
dev_count = lib.get_device_count(devenum)    #Count detected devices
if dev_count == 0:
    print("No␣devices␣detected!\nExit␣or␣restart?␣(E/R)")
    #Holds for input if no devices detected
    c=input();
    if c=="E" or c=="e":
        exit()  #Exits script
    elif c=="R" or c=="r":
        os.startfile(__file__)
        sys.exit()  #Restarts script

else:
    print("Devices␣found:␣" + repr(dev_count))
    controller_name = controller_name_t()
    for dev_ind in range(0, dev_count):
        enum_name = lib.get_device_name(devenum, dev_ind)
        result = lib.get_enumerate_device_controller_name(devenum, dev_ind,
        byref(controller_name))
        if result == Result.Ok:
                #Generates and displays list of enumerated devices
            print("Device␣#{}␣at:␣".format(dev_ind)
             + repr(enum_name.decode('UTF8'))
             + ".␣Name:␣" + repr(controller_name.ControllerName.decode('UTF8'))
              + ".")
```

Listing 2: Device initialization

```
Las_id=0
Det_id=1
LasTh_id=2
#Axis identifiers for connected stages


Las=lib.get_device_name(devenum,Las_id)
Det=lib.get_device_name(devenum,Det_id)
LasTh=lib.get_device_name(devenum,LasTh_id)
#Adresses of devices

devid=[lib.open_device(Las),lib.open_device(Det),lib.open_device(LasTh)]
#Open and assign devices

dsdx=[400,200,100]
#Steps pr. mm for translation, pr. deg for rotation
```

Listing 3: General control commands

```
def GetSpeed(devid,dsdx):
        #Returns vector of current set speed of all devices in mm/s
    mvst1=move_settings_t()
    mvst2=move_settings_t()
    mvstA=move_settings_t()

    #Fetch current move settings for all devices
    lib.get_move_settings(devid[0],byref(mvst1))
    lib.get_move_settings(devid[1],byref(mvst2))
    lib.get_move_settings(devid[2],byref(mvstA))
```

```
    Speed=[mvst1.Speed/dsdx[0],mvst2.Speed/dsdx[1],mvstA.Speed/dsdx[2]]
    #Create array of speed for all devices
    return Speed

def SetSpeed(devid,dsdx,dxdt): #Sets speed of all devices to dxdt in mm/s
    mvst1=move_settings_t()
    mvst2=move_settings_t()
    mvstA=move_settings_t()

    #Fetch current move settings for all devices
    lib.get_move_settings(devid[0],byref(mvst1))
    lib.get_move_settings(devid[1],byref(mvst2))
    lib.get_move_settings(devid[2],byref(mvstA))

    #Update settings with new speed, in steps
    mvst1.Speed=int(dsdx[0]*dxdt[0])
    mvst2.Speed=int(dsdx[1]*dxdt[1])
    mvstA.Speed=int(dsdx[2]*dxdt[2])

    #Assign updated move settings to devices
    lib.set_move_settings(devid[0],byref(mvst1))
    lib.set_move_settings(devid[1],byref(mvst2))
    lib.set_move_settings(devid[2],byref(mvstA))

def GetPos(devid,dsdx): #Returns position in mm, whole steps only
    x_pos1=get_position_t()
    x_pos2=get_position_t()
    ang=get_position_t()

    est1=engine_settings_t()
    est2=engine_settings_t()
    estA=engine_settings_t()


    #Fetch position structs
    lib.get_position(devid[0],byref(x_pos1))
    lib.get_position(devid[1],byref(x_pos2))
    lib.get_position(devid[2],byref(ang))


    #Fetch engine settings
    lib.get_engine_settings(devid[0],byref(est1))
    lib.get_engine_settings(devid[1],byref(est2))
    lib.get_engine_settings(devid[2],byref(estA))

    #Decode microstep fraction
    umode=[2**(est1.MicrostepMode-1),2**(est1.MicrostepMode-1),
    2**(estA.MicrostepMode-1)]

    #Calculate whole step positions in mm
    SPos=[x_pos1.Position/dsdx[0],x_pos2.Position/dsdx[1]
    ,ang.Position/dsdx[2]]

    #Calculate microstep positions in mm
    uPos=[x_pos1.uPosition/(umode[0]*dsdx[0]),
    x_pos2.uPosition/(umode[1]*dsdx[1]),
```

```
    ang.uPosition/(umode[2]*dsdx[2])]

    #Determines total position
    Pos=[-round(SPos[0]+uPos[0],4),-round(SPos[1]+uPos[1],4),
    round(SPos[2]+uPos[2],4)]

    return Pos


def Arrived(devid,dsdx): #Returns 1 if stage has stopped moving

    sts1=status_t()
    sts2=status_t()
    stsA=status_t()

    lib.get_status(devid[0],byref(sts1))
    lib.get_status(devid[1],byref(sts2))
    lib.get_status(devid[2],byref(stsA))

    if sts1.CurSpeed==0 and sts2.CurSpeed==0 and stsA.CurSpeed==0:
        return 1
    else:
        return 0

def Move(devid,dsdx,tgt,refresh,hold):
        #Moves both stages to tgt[0:1] position in mm
        #Rotates laser ot tgt[2] degrees

    est1=engine_settings_t()
    est2=engine_settings_t()
    estA=engine_settings_t()

    lib.get_engine_settings(devid[0],byref(est1))
    lib.get_engine_settings(devid[1],byref(est2))
    lib.get_engine_settings(devid[2],byref(estA))

    #Fetch microstep mode
    umode=[2**(est1.MicrostepMode-1),2**(est1.MicrostepMode-1),
    2**(estA.MicrostepMode-1)]

    #Whole steps of target
    Step=[-int(tgt[0]*dsdx[0]+0.5),-int(tgt[1]*dsdx[1]+0.5,
    int(tgt[2]*dsdx[2]+0.5)]

    #Microsteps equivalent to residuals
    uStep=[int((-tgt[0]*dsdx[0]-Step[0])*umode[0]),
    int((-tgt[1]*dsdx[1]-Step[1])*umode[1]),
    int((tgt[2]*dsdx[2]-Step[2])*umode[2])]

    #Moves stages to determined step and microstep equivalent to tgt(mm)
    lib.command_move(devid[0],Step[0],uStep[0])
    lib.command_move(devid[1],Step[1],uStep[1])
    lib.command_move(devid[2],Step[2],uStep[2])


    if hold==1:
    #Holds process until stage arrives at tgt,
```

```
    #rechecks every refresh no. seconds
        t.sleep(0.5)
        while Arrived(devid,dsdx)==0:
            t.sleep(refresh)

def ChangeAspect(devid,dsdx,newang,refresh,hold,Dist):
        #Moves and rotates laser to hit same point but with a new angle
    #Gets initial position
    Pos=GetPos(devid,dsdx)

    #Conversion to radians
    newangR=(newang)*np.pi/180

    dR=newangR-Pos[2]*np.pi/180

    dL=-np.tan(dR)*Dist

    #Limits determined by the travel range of the laser
    lim=[np.arctan(Pos[0]/Dist),np.arctan((Pos[0]-50)/(Dist))]

    if newangR>lim[0]:
        newangR=lim[0]
    elif newangR<lim[1]:
        newangR=lim[1]

    #Compute new position and angle
    newPos=[Pos[0]+dL,Pos[1],newangR*180/np.pi]


    Move(devid,dsdx,newPos,refresh,hold)
```

Listing 4: Transmission Sweep command

```
def RunSweep(devid,dsdx,xL,SwRng,SwSpd,fs,verbose,outputdir,Offset):

    SetSpeed(devid,dsdx,SwSpd)
    Pos=GetPos(devid,dsdx)
    if abs(Pos[1]-SwRng[1])<abs(Pos[1]-SwRng[0]):
        s=1            #Set starting point as the closest end of range
    else:
        s=0

    #Set speed to 1mm/s for starting position move
    if verbose==1:
        print("————————————————————————————————")
        print("Moving␣laser␣to␣{}mm".format(xL))
        print("Moving␣detector␣to␣{}mm".format(SwRng[s]))
        print("————————————————————————————————")

    Move(devid,dsdx,[xL,SwRng[s],0],1/fs,1) #Move to starting position, hold till finished

    tSweep=(SwRng[1]-SwRng[0])/SwSpd[1] #Sweep time
    nSam=int(tSweep*fs+0.5)             #Number of samples to be taken

    if verbose==1:
        Pos=GetPos(devid,dsdx)
        print("————————————————————————————————")
```

```
        print("Laser␣position:␣{}mm".format(Pos[0]))
        print("Detector␣position:␣{}mm".format(Pos[1]))
        print("--------------------------------------------------")
        print("Move␣complete,␣beginning␣sweep")
        print("Expected␣sweep␣time:{}s".format(tSweep))
        print("--------------------------------------------------")

    SetSpeed(devid,dsdx,SwSpd)              #Specified sweep speed

    data=np.zeros(nSam,dtype=np.float64)       #Preallocate data array
    x=np.linspace(SwRng[s]+Offset,SwRng[1-s]+Offset,nSam)     #Define x values
    Peak=np.zeros(2,np.float64)                #Peak parameter list

    with nidaqmx.Task() as task:
        task.ai_channels.add_ai_voltage_chan("Dev1/ai0",max_val=10,min_val=0)
        #Initiate input channel
        task.timing.cfg_samp_clk_timing(fs,source='',active_edge=Edge.RISING
        ,sample_mode=AcquisitionType.FINITE,samps_per_chan=nSam)
        #Specify sampling frequency


        stream=AnalogSingleChannelReader(task.in_stream)
        #Initialize data stream object

        Move(devid,dsdx,[xL,SwRng[1-s],0],1/fs,0)
        #Start sweep move, no hold
        stream.read_many_sample(data,
        number_of_samples_per_channel=nSam,timeout=tSweep+1)
        #Data aquisition through stream object
    if verbose==1:
        print("Beginning␣write␣operation")
        tsw=t.time()

    np.savetxt(outputdir+"{}mm.csv".format(round(xL+Offset,
    3)),np.c_[x,data],delimiter=",")
    #Write raw data to csv file

    N=max([int(0.001*fs/SwSpd[1]),1])
    #Define moving mean window as equivalent to 1um,
    #set to 1 if spatial sampling is less than 1 pr. um

    mmData=np.convolve(data,np.ones((N,))/N,mode="Same")
    #Moving mean using convolution, generates same size as data array
    Peak=[max(mmData),x[np.argmax(mmData)]]
    #Returns peak value of moving mean result and corresponding position in mm
    if verbose==1:
        print("Write␣operation␣complete,time␣taken:␣{}s".format(t.time()-tsw))
        print("--------------------------------------------------")
        print("Data␣returned␣as:␣"+"{}mm.csv".format(round(xL+Offset,3)))
        print("Collected␣samples:␣{}".format(int(nSam)))
        print("Mean␣of␣samples:␣{}␣mV".format(round(np.mean(data)*1000)))
        print("Standard␣deviation␣of␣samples:␣{}␣mV".format(round(np.std(data*1000))))
        print("--------------------------------------------------")
        print("Peak␣found␣at:␣{}mm".format(round(Peak[1],3)))
        print("Peak␣value:␣{}␣V".format(Peak[0]))
        print("--------------------------------------------------")
    return Peak
```

Listing 5: Matched filter enabled peak detection

```
def MatchFilter(D,Fcycles,fs,fm):
    Nf=int(fs/fm); #Number of samples per modulation cycle

    h=np.hstack((np.ones(int(Nf/2)),np.zeros(int(Nf/2))))
    #Create core filter cycle for a square wave

    if Fcycles*Nf>(0.2*len(D)):
        Fcycles=int(0.2*len(D)/Nf)
        #Limits number of cycles in filter if it becomes large compared to dataset
    hf=np.tile(h,Fcycles)   #Repeats filter cycles to create full filter

    N=max([int(fs/(2*fm)),1])
    #Smooths over flats of modulation wave

    mmD=np.convolve(D,np.ones((N,))/N,mode=”Same”)
    #Moving mean to approximate DC voltage


    F=np.convolve(hf,D-min(mmD),mode=’same’)
    #Filters using convolution
    return F

def FindPeak(devid,dsdx,xL,Rng,Ang,fs,fm,Fcycles):

    Spd=[1,10,0.5]

    SetSpeed(devid,dsdx,Spd)
    Pos=GetPos(devid,dsdx)

    #Set starting point as the closest end of range
    if abs(Pos[1]-Rng[1])<abs(Pos[1]-Rng[0]):
        s=1
    else:
        s=0

    Move(devid,dsdx,[xL,Rng[s],Ang],0.01,1)
    #Move to starting position, hold till finished

    tSweep=(Rng[1]-Rng[0])/Spd[1] #Sweep time
    nSam=int(tSweep*fs+0.5) #Number of samples to be taken

    SetSpeed(devid,dsdx,Spd) #Specified sweep speed

    data=np.zeros(nSam,dtype=np.float64) #Preallocate data array
    x=np.linspace(Rng[s],Rng[1-s],nSam) #Define x values
    Peak=np.zeros(2,np.float64)  #Peak parameter array

    with nidaqmx.Task() as task:
        task.ai_channels.add_ai_voltage_chan(”Dev1/ai0”,max_val=10,min_val=0)
        #Initiate input channel
        task.timing.cfg_samp_clk_timing(fs,source=’’,active_edge=Edge.RISING,
        sample_mode=AcquisitionType.FINITE,samps_per_chan=nSam)
        #Specify sampling frequency


        stream=AnalogSingleChannelReader(task.in_stream)
```

```
    #Initialize data stream object

    Move(devid,dsdx,[xL,Rng[1-s],Ang],0.01,0)
    #Start sweep move, no hold
    stream.read_many_sample(data,
     number_of_samples_per_channel=nSam,timeout=tSweep+1)
     #Data aquisition through stream object

Fd=MatchFilter(data,Fcycles,fs,fm)

N=max([int(fs/(2*fm)),1])
#Define moving mean window as equivalent to one half modulation cycle
mmData=np.convolve(data,np.ones((N,))/N,mode="valid")
#Set of "flat" values corresponding to modulation cycles


Peak=[data[np.argmax(Fd)]-min(mmData),x[np.argmax(Fd)]-(1-2*s)*Spd[1]/2]
#Initial peak with approximate compensation from overshoot due to DAQ delay

cdata=np.convolve(data,np.hstack((np.zeros((N-1,)),1)),mode='valid')

sdNoise=(np.sqrt(np.var(cdata-mmData)));
print("Initial␣peak␣found␣at:␣{}␣mm".format(Peak[1]))
print("Initial␣peak␣value:␣{}␣V".format(Peak[0]))
print("Stndard␣deviation␣of␣samples:␣{}␣V".format(sdNoise))
if max[Fd]>(1.5*np.mean(Fd)):
#Considers there to be a peak if filter response has a peak
#50% higher than the mean
    PeakN=[0,Peak[1]];
    #Initiates peak list
    while abs(PeakN[-1]-PeakN[-2])>0.5 and Spd[1]>0.1:
    #Continues narrowing untill standstill or peak converges
        Spd[1]=Spd[1]/2     #Reduces speed to combat overshoot
        dev=2*abs(PeakN[-1]-PeakN[-2])
        #Narrows range to twice deviation from last peak

        Rng=[max([PeakN[-1]-dev,-10]),min([PeakN[-1]+dev,100])]

        #Moves to position for new scan
        SetSpeed(devid,dsdx,Spd)
        Pos=GetPos(devid,dsdx)

            #Set starting point as the closest end of range
        if abs(Pos[1]-Rng[1])<abs(Pos[1]-Rng[0]):
            s=1
        else:
            s=0

        Move(devid,dsdx,[xL,Rng[s],Ang],0.01,1)
        #Move to starting position, hold till finished

        tSweep=(Rng[1]-Rng[0])/Spd[1] #Sweep time
        nSam=int(tSweep*fs+0.5) #Number of samples to be taken

        SetSpeed(devid,dsdx,Spd) #Specified sweep speed

        data=np.zeros(nSam,dtype=np.float64)     #Preallocate data array
```

```
            x=np.linspace(Rng[s],Rng[1-s],nSam)      #Define x values

            with nidaqmx.Task() as task: #Scanning task
                task.ai_channels.add_ai_voltage_chan("Dev1/ai0",
                max_val=10,min_val=0)
                #Initiate input channel
                task.timing.cfg_samp_clk_timing(fs,source='',active_edge=Edge.RISING,
                sample_mode=AcquisitionType.FINITE,samps_per_chan=nSam)
                #Specify sampling frequency


                stream=AnalogSingleChannelReader(task.in_stream)
                #Initialize data stream object

                Move(devid,dsdx,[xL,Rng[1-s],Ang],0.01,0)
                #Start sweep move, no hold
                stream.read_many_sample(data,
                number_of_samples_per_channel=nSam,timeout=tSweep+1)
                #Data aquisition through stream object

            Fd=MatchFilter(data,Fcycles,fs,fm) #Filtering of data

            PeakN.append(x[np.argmax(Fd)])
            #Returns peak value of moving mean result
            #and corresponding position in mm

        SetSpeed(devid,dsdx,[2,4,0.5]) #Increase speed
        Move(devid,dsdx,[xL,PeakN[-1],Ang],0.01,1) #And move to position of peak

        data=np.zeros(fs,dtype=np.float64)
        with nidaqmx.Task() as task:    #Acquire 1s of samples
            task.ai_channels.add_ai_voltage_chan("Dev1/ai0",max_val=10,min_val=0)
             #Initiate input channel
            task.timing.cfg_samp_clk_timing(fs,source='',active_edge=Edge.RISING
            ,sample_mode=AcquisitionType.FINITE,samps_per_chan=fs)
            #Specify sampling frequency


            stream=AnalogSingleChannelReader(task.in_stream)
            #Initialize data stream object

            stream.read_many_sample(data,
             number_of_samples_per_channel=fs,timeout=2)
             #Data aquisition through stream object

        mmData=np.convolve(data,np.ones((N,))/N,mode="valid")
        #Moving mean over half modulation cycle

        Peak=[max(mmData)-min(mmData),PeakN[-1]]
        #Assign current position and voltage difference from modulation

    else:
        Peak=[0,0]

    return Peak
```